Structural, Physical, and Electronic Properties Studies of Topological Materials

Thesis submitted for the degree of

Doctor of Philosophy (Sc.)

in

Physics

by

Susmita Changdar

Department of Physics
University of Calcutta
2023

Dedicated to my beloved parents

Abstract

Topological materials have been the most captivating research fields in condensed matter physics, yielding connections between different scientific disciplines and promising breakthroughs in topological quantum computations. This thesis embarks on synthesizing and studying the properties of single crystals those are anticipated to host nontrivial band topology. Using angle-resolved photoemission spectroscopy (ARPES), we explored the band structures of various topological materials. For instance, FeSi is a topological semimetal with exotic spin-1 and spin-3/2 fermions. Overall the ARPES data of FeSi matches with density functional theory (DFT) calculations. However, the respective higher-fold degenerate band crossing points (BCPs) appear 0.54 eV above the Fermi level, which could not be observed by ARPES. Subsequently, we performed ARPES measurements on $K_{0.65}RhO_2$ that is predicted to be a quantum topological Hall insulator. Although no topologically protected band dispersions were observed, we found momentum-dependent strong electron-phonon coupling possibly leading to a high-energy kink at around 195 meV. By studying the magnetic and transport properties of antiferromagnetic (AFM) topological insulator (TI) $Mn_{1-x}Sn_xBi_2Te_4$, we observed reduction in the saturation magnetic field with increasing Sn. At an appropriate Sn concentration (68%) we observe the quantum anomalous Hall (QAH) state at much lower critical fields than in the parent $MnBi_2Te_4$. Furthermore, ARPES investigations of 10% magnetic impurities (Co, Mn, Eu) doped into the topological insulator Bi_2Se_3 revealed unaltered topological surface states (TSSs), demonstrating the robustness of topological states against the magnetic impurities. This indicates that introducing more magnetic impurities is necessary to open the gap. We further studied the electronic band structure of noncollinear AFM Weyl semimetal (WSM) Mn_3Ge. Presence of several bands near the Fermi level obstructs us from resolving the bands associated with the Weyl nodes. Nevertheless, we achieved commendable agreement between DFT calculations and ARPES data. By comparing ARPES data with orbital-resolved DFT calculations, we could estimate the orbital contributions of different bands.

রূপরেখা

কঠিন অবস্থা পদার্থবিজ্ঞানের এক চিত্তাকর্ষক গবেষণা শাখা হলো টপোলজিকাল উপাদান, যা বিভিন্ন বৈজ্ঞানিক শাখার মধ্যে সংযোগ প্রদান করে এবং টপোলজিক্যাল কোয়ান্টাম গণনার ক্ষেত্রে নতুন সাফল্য এনে দেবার সম্ভাবনা রাখে। এই থিসিসটি অগতানুগতিক (নন্ট্রিভিয়াল) ব্যান্ড টোপোলজি ধারণ করা উচিত এইরূপ অযুগ্ম ক্রিস্টালের সংশ্লেষণ এবং তাদের বৈশিষ্ট্যগুলির পুঙ্খানুপুঙ্খ অধ্যয়ন এর উপর কেন্দ্রীভূত। অ্যাঙ্গেল রিসল্ভড ফোটোএমিশন স্পেকট্রোস্কোপি (ARPES) ব্যবহার করে, আমরা বিভিন্ন টপোলজিকাল উপাদানের ব্যান্ড নিরীক্ষণ করেছি। উদাহরণস্বরূপ, FeSi হল একটি টোপোলজিক্যাল সেমিমেটাল যার মধ্যে স্পিন-১ এবং স্পিন-৩/২ ফার্মিয়ন এর উপস্থিতি প্রত্যাশিত। সামগ্রিকভাবে FeSi-এর থেকে প্রাপ্ত ARPES পর্যবেক্ষণ, ডেন্সিটি-ফাঙ্কশনাল তত্ত্বের (DFT) সাথে সমতুল্য। কিন্তু হাই-ফোল্ড ডিজেনারেট ব্যান্ড ক্রসিং পয়েন্টগুলি (BCPs) ফার্মি স্তরের ০.৫৪ ইলেক্ট্রনভোল্ট উপরে থাকায় ARPES এর দ্বারা এদের পর্যবেক্ষণ সম্ভব হয়নি। পরবর্তী কাজটিতে আমরা $K_{0.65}RhO_2$ এর উপর ARPES পরিমাপ করেছি। $K_{0.65}RhO_2$ কে একটি কোয়ান্টাম টপোলজিক্যাল হল (QTH) অন্তরক বলে অনুমান করা হয়। যদিও ARPES দ্বারা টপোলজিক্যালভাবে সুরক্ষিত ব্যান্ড পরিলক্ষিত হয়নি, আমরা ব্যান্ড গুলি থেকে ভরবেগ-নির্ভর শক্তিশালী ইলেকট্রন-ফোনন কাপলিং এর উপস্থিতি লক্ষ্য করেছি যা ১৯৫ মিলিইলেক্ট্রনভোল্ট বন্ধন শক্তিতে ব্যান্ড ডিসপেরশনে স্পষ্ট পরিবর্তন ঘঠায়। অ্যান্টিফেরো-ম্যাগনেটিক (AFM) টপোলজিকাল ইনসুলেটর (TI) $Mn_{1-x}Sn_xBi_2Te_4$ এর চৌম্বকীয় এবং পরিবহন বৈশিষ্ট্যগুলি অধ্যয়ন করে, আমরা Sn বৃদ্ধির সাথে সম্পৃক্ত চৌম্বকক্ষেত্রের হ্রাস লক্ষ্য করেছি। একটি উপযুক্ত Sn ঘনত্বে (৬৮%) আমরা বিশুদ্ধ $MnBi_2Te_4$ থেকে অনেক কম চৌম্বক ক্ষেত্রে কোয়ান্টাম অ্যানোমালাস হল (QAH) অবস্থা পর্যবেক্ষণ করি। টপোলজি-ক্যাল অন্তরক Bi_2Se_3তে ডোপ করা ১০% চৌম্বকীয় অশুদ্ধি (Co, Mn, Eu) ARPES তদন্তে অপরিবর্তিত টপোলজিক্যাল সারফেস স্টেট (TSSs) প্রদর্শন করে, যা চৌম্বকীয় অশুদ্ধির বিরুদ্ধে টপোলজিক্যাল অবস্থার দৃঢ়তার প্রমান দেয়। TSS এ ব্যান্ড গ্যাপ খোলার জন্য আরও চৌম্বকীয় অশুদ্ধির সংযোজন জরুরি। এরপর আমরা ননকোলিনিয়ার AFM Weyl সেমিমেটাল (WSM) Mn_3Ge এর ইলেকট্রনিক ব্যান্ড কাঠামো অধ্যয়ন করেছি। ফার্মি স্তরের কাছাকাছি বহুসংখ্যক ব্যান্ডের উপস্থিতি Weyl নোডগুলির সাথে যুক্ত ব্যান্ডগুলিকে পৃথক করতে বাধা দেয়। তবুও, আমরা DFT গণনা এবং ARPES ডেটার মধ্যে গুণগত সাদৃশ্য পর্যবেক্ষণ করেছি। উপরন্তু, অরবিটাল-রিসল্ভড DFT গণনার সাথে ARPES ডেটা তুলনা করে আমরা ব্যান্ডগুলিতে বিভিন্ন অরবিটালের অবদান অনুমান করতে পারি।

Acknowledgements

My time pursuing my Ph.D. at the S. N. Bose National Centre for Basic Sciences, Kolkata, has been a remarkable privilege. The outstanding research facilities and the exceptional people I've worked with have enriched my journey. Since the beginning of my education, I have crossed paths with many people who've taught me the importance of learning and sparked my love for research. At this moment, I wish to convey my heartfelt gratitude to all these individuals sincerely.

I wish to extend my heartfelt acknowledgments to Dr. Thirupathaiah Setti, my dedicated supervisor. His guidance has not only honed my research skills but also enriched my journey with invaluable insights and novel ideas throughout my Ph.D. tenure.

I convey my appreciation to the respected members of the examination committee for generously dedicating their time and effort to evaluate my thesis.

I am deeply thankful to the S. N. Bose National Centre for Basic Sciences for enriching my research environment. The research facilities, serene surroundings, and comfortable accommodations have nurtured my academic pursuits. I am thankful to Technical Research Centre (TRC) for their support, as this research has utilized the Instrument facilities at the TRC of S. N. Bose National Centre for Basic Sciences, established under the TRC project of the Department of Science and Technology (DST), Govt. of India. I am grateful to the University Grants Commission (UGC), India, for the Ph.D. fellowship that supported my research journey.

My appreciation goes out to the entire Quantum-Materials group. Their cooperation has made these five years of my Ph.D. unforgettable. I extend my heartfelt gratitude to Indrani Kar, Achintya Low, Sayan Routh, Shubham Purwar, Susanta Ghosh, and Soumya Ghorai, whose friendship and collaborations have been the cornerstone of my research experience. I am deeply thankful to my junior, Soumya Ghorai, for giving his valuable time and effort in proofreading my thesis, and identifying the typos that had eluded my notice. I am indebted to the postdoctoral scholars of our group, Dr. Reena Goyal, Dr. Pankaj Maheshwari, Dr. Tushar Kanti Bhowmik, and Dr. Ayana Mukhopadhyay, whose invaluable insights have guided me through various research challenges.

My sincere thanks to my Ph.D. coursework teachers, Dr. Atindra Nath Pal, Dr. Manoran-

jan Kumar, Late Prof. Sugata Mukherjee, Prof. Kalyan Mandal, Prof. Ranjan Choudhuri, and Dr. Thirupathaiah Setti for their exceptional teaching.

I express my sincere gratitude for the invaluable technical support provided during ARPES measurements by Dr. Y. Kushnirenko and Prof. Bernd Büchner from IFW Dresden, Germany, as well as Dr. Nicholas C. Plumb and Prof. Ming Shi from PSI, Switzerland. Additionally, I extend my heartfelt thanks to Kritika Vijay, Dr. Soma Banik, and Dr. Tapas Ganguly for their indispensable contributions throughout the ARPES measurements in RRCAT, India. I extend my gratitude to Dr. Saicharan Aswartham and Grigory Shipunov from IFW Dresden, Germany, as well as Dr. Rabia Sultana and Dr. V. P. S. Awana from NPL, India. Their generosity in providing single crystals for my research was a pivotal contribution, especially when our lab did not have a crystal growth facility. I appreciate Anumita Bose, Nesta Beno Joseph, and Dr. Awadhesh Narayan from IISC Bangalore. Their collaborative theoretical work and DFT calculations have significantly enhanced our understanding of the collected ARPES data, contributing to a deeper insight into our research. I sincerely thank the technical staff, Mr. Rishikesh Nandi, Mr. Shakti Nath Das, Mrs. Urmi Chakrabarty, Mr. Joy Bandopadhyay, Mr. Sourabh Sinha, and Mr. Debarghya Ghosh for their unwavering technical support during the measurements performed in S.N.B.N.C.B.S., Kolkata.

A heartfelt acknowledgment to my M.Sc supervisor Dr. Samudra Roy and teachers Dr. Debraj Choudhury, Prof. Sayan Kar, Dr. Thirthashankar Ray, and Prof. Sugata Pratik Khastgir.

My journey has been brightened by the presence of my dear friends: Tanmoy Chakraborty, Debayan Mondal, Premashish Kumar, Biswajit Panda, Prasun Boyal, Anish Das, and Riju Pal, who have woven unforgettable memories alongside me. I thank my juniors, Shubham Purwar, Susanta Ghosh, and Achintya Low, for bringing joy to campus life and creating a sense of homeliness within our lab. I extend my gratitude to my seniors Shantanu Mukherjee, Surya Narayan Panda, Rituparna Mandal, Anirban Mukherjee, Dhiraj Tapadar, Rafiqul Alam, and Shubhadip Moulik for their unwavering support.

I thank my uncle, Prof. Shubhas Samanta, for instilling the joy of science in me since my childhood.

I am thankful to my father, Rabindranath Changdar (associate professor, Kharagpur College). His wisdom and encouragement have been a driving force behind my journey.

To my mother, Rohini Changdar, I offer heartfelt thanks for her constant belief in my potential, providing me with the courage to pursue my dreams. They have shaped my path and given me the strength to reach for my dreams. I feel truly lucky to have been born as their daughter.

Finally, I want to give a special thanks to my husband, Arindam Samanta. He has been there for me through the ups and downs, supporting me without fail and believing in me no matter what.

Susmita Changdar
Quantum Materials Lab,
Condensed Matter and Materials Physics Department,
S. N. Bose National Centre for Basic Sciences, Kolkata
September 22, 2023

Publications relevant to the thesis

1. **Susmita Changdar**, S. Aswartham, Anumita Bose, Y. Kushnirenko, G. Shipunov, N. C. Plumb, M. Shi, Awadhesh Narayan, B. Büchner, and S. Thirupathaiah, Electronic structure studies of FeSi: A chiral topological system, Phys. Rev. B **101**, 235105 (2020).

2. **Susmita Changdar**, Rabia Sultana, Soma Banik, V. P. S. Awana, and Setti Thirupathaiah, Angle resolved photoemission spectroscopy study on electronic band structure of topological insulator Bi_2Se_3 in the presence of magnetic impurities, AIP Conference Proceedings **2265**, 030355 (2020).

3. **Susmita Changdar**, Grigory Shipunov, Nesta B. Joseph, Nicholas C. Plumb, Ming Shi, Bernd Büchner, Awadhesh Narayan, Saicharan Aswartham, and Setti Thirupathaiah, Anomalous band renormalization due to a high-energy kink in $K_{0.65}RhO_2$ with colossal thermoelectric power factor, Phys. Rev. Materials **5**, 055402 (2021).

4. **Susmita Changdar**, Susanta Ghosh, Kritika Vijay, Indrani Kar, Sayan Routh, P. K. Maheswari, Soumya Ghorai, Soma Banik, and S. Thirupathaiah, Nonmagnetic Sn doping effect on the electronic and magnetic properties of antiferromagnetic topological insulator $MnBi_2Te_4$, Physica B: Condensed Matter **657**, 414799 (2023).

5. **Susmita Changdar***, Susanta Ghosh*, Anumita Bose, Indrani Kar, Achintya Low, Patrick Le Fevre, François Bertran, Awadhesh Narayan, and Setti Thirupathaiah, Electronic Band Structure Studies of Magnetic Weyl Semimetal, Mn_3Ge, (*under review*).

Other works

1. Shubham Purwar, **Susmita Changdar**, Susanta Ghosh, S. Thirupathaiah, Magnetocrystalline Anisotropy and Magnetocaloric Effect Studies on the Room-temperature 2D Ferromagnetic Cr_4Te_5, arXiv:2209.08477 (2022)

2. Achintya Low, Susanta Ghosh, **Susmita Changdar**, Sayan Routh, Shubham Purwar, and Setti Thirupathaiah, Tuning of topological properties in the strongly correlated antiferromagnet Mn_3Sn via Fe doping, Physical Review B 106, 144429 (2022).

Contents

List of Figures

Chapter 1

Introduction

The discovery of topological phases of the matter, such as the quantum Hall effect (QHE) [14] has developed one of the most intriguing research fields in condensed matter physics, as the scientific context of these systems not only connects various fields of the fundamental sciences but provides fascinating technological applications in spintronics and topological quantum computations [15, 16]. Importantly, the theory of topological materials is deeply rooted in high-energy physics as these materials can be classified based on the characteristic Weyl fermions [17], Dirac fermions [18], and Majorana fermions [19, 20], which are the fundamental particles predicted in high-energy physics a long time ago. The presence of such Dirac fermions was initially observed in the nontrivial two-dimensional topological insulators (TIs) like 2D HgTe quantum wells, Bi_2Se_3, Bi_2Te_3, Sb_2Te_3, etc, hosting quantum spin Hall (QSH) state. In these systems, the conducting Dirac fermions present on the sample surface are protected by the time-reversal symmetry (TRS), while the bulk states remain insulating in nature.

Followed by TIs, several other topological materials such as topological superconductors [21], Dirac semimetals (DSMs) [22, 23], Weyl semimetals (WSMs) [24] have been discovered. Unlike in TIs, in DSMs and WSMs the topological states are bulk in nature. In the case of DSM, the band crossing points (BCPs) are protected by the time-reversal and inversion symmetries to possess four-fold degeneracy. Upon lifting one of these two symmetries, one can derive the WSM from DSM. In this case, the BCP behaves like a Weyl point, is protected by one of the two symmetries to possess two-fold degeneracy. Apart from TI, DSMs, and WSMs, there exist other classes of quantum states, like Majorana fermions, that are localized at the edge of the topological superconductors [25]. Recently,

a new class of quantum materials also emerged with manifold degenerate fermions at the BCP [26].

Microscopic understanding of these exotic topological quantum materials is of utmost importance for unraveling their potential futuristic applications in quantum computations and spintronics. The objective of this thesis revolves around the synthesis of high-quality single crystals of various topological materials with in-depth investigation of their structural, physical, electronic properties, as well as electronic band structure studies.

The first chapter of this thesis provides an overview of various topological materials discovered to date. We begin with the QHE, the first identified topological state, and then explore other topological states discovered over time. We examine experimental evidence of their topological phases in different condensed matter systems for each class of these materials. We also offer a concise theoretical explanation to give experimental researchers a basic understanding without going into complex theoretical derivations. The first section confers about the QHE and briefly introduces important mathematical concepts like the Chern number and Berry curvature. These concepts will be essential for grasping more advanced discussion on topological phases in later sections. Moving from there, we cover the topics such as the quantum spin-Hall (QSH) insulators (also known as 2D-TIs), 3D-TIs, QAH insulators, WSMs and DSMs. We conclude the chapter by exploring topological semimetals with higher-fold degeneracy.

In the second chapter, we discuss the experimental techniques utilized for the synthesizing of various single crystals and exploring the properties. We start by discussing the flux-growth technique employed for the single crystal growth. Moving forward, we focus on crystal characterization methods, including energy dispersive X-ray analysis (EDS), X-ray diffraction (XRD), and low-energy electron diffraction (LEED). Magnetic properties of the single crystals were studied by using the vibrating sample magnetometer (VSM). Electrical and magneto-transport studies were carried out suing the physical property measurement system (PPMS of Quantum Design, DynaCool, 9T). Valance band and core-level spectra is studied using the X-ray photoemission spectroscopy (XPS). Low-energy band structure is studied using the angle-resolved photoemission spectroscopy (ARPES). Additionally, we have briefly introduced the critical components of the setup and their respective functions.

From Chapter 3 to Chapter 7, we present our experimental results obtained on various topological materials conducted during my Ph.D. tenure. Chapter 3 discusses the band

structure of FeSi, a topological semimetal that hosts higher-fold degenerate fermions. Using ARPES measurements, we extensively studied the band structure of FeSi. In Chapter 4, we analyze the band structure of theoretically predicted QAH insulator $K_{0.65}RhO_2$ using ARPES. Our studies suggest $K_{0.65}RhO_2$ to be a strongly correlated system but not a QAH. In Chapter 5, we explore the effects of Sn doping on the electronic, magnetic, and transport properties of the intrinsic AFM-TI $MnBi_2Te_4$. Chapter 6 investigates the influence of magnetic impurities on the electronic structure of 3D TI Bi_2Se_3 using ARPES, while Chapter 7 concentrates on the electronic structure of the magnetic WSM Mn_3Ge. Finally, Chapter 8 concludes the thesis by summarizing the main observations drawn from our experimental observations.

1.1 Quantum Hall effect

Topological materials have been the most fascinating research fields in condensed matter physics, which started with the discovery of QHE [14]. According to Landau's theory, different phases of matter can be classified by their spontaneously broken symmetries. For example, the crystalline solids and the magnetic materials can be classified by the spontaneously broken translational and the rotational symmetries, respectively. However, QHE [27, 28] could not be classified in such a way as these states are protected by certain symmetries, which compelled a new classification of states known as topological phases of matter.

The phenomena of QHE was first discovered by K.V. Klitzing in 1980 [14], for which he won the Nobel prize in 1985. A typical Hall set-up is presented in Fig. 1.1(a). When a magnetic field (B) is applied along the z axis and the current (I) is flowing along x-direction, a Hall voltage (V_H) is generated along the y-axis. The Lorentz force $q\mathbf{v}\times\mathbf{B}$ bends the charge carrier's flow and accumulates the opposite charge carriers to the opposite side of the sample, generating a potential difference between the opposite sides. This electric potential along the $y-$axis is termed Hall voltage V_H. In an ordinary Hall state, the Hall resistance $R_{xy} = V_H/I$ varies linearly as a function of magnetic field B. However, in quantum Hall state, R_{xy} vs. B graph exhibits plateaus for a particular magnetic field range after which R_{xy} jumps to the next plateau (Fig. 1.1(b)). Moreover, When R_{xy} jumps from one plateau to the next plateau, the longitudinal Hall resistance R_{xx} becomes zero and only becomes finite at the step of each plateau in R_{xy} (Fig. 1.1(b)). The value of

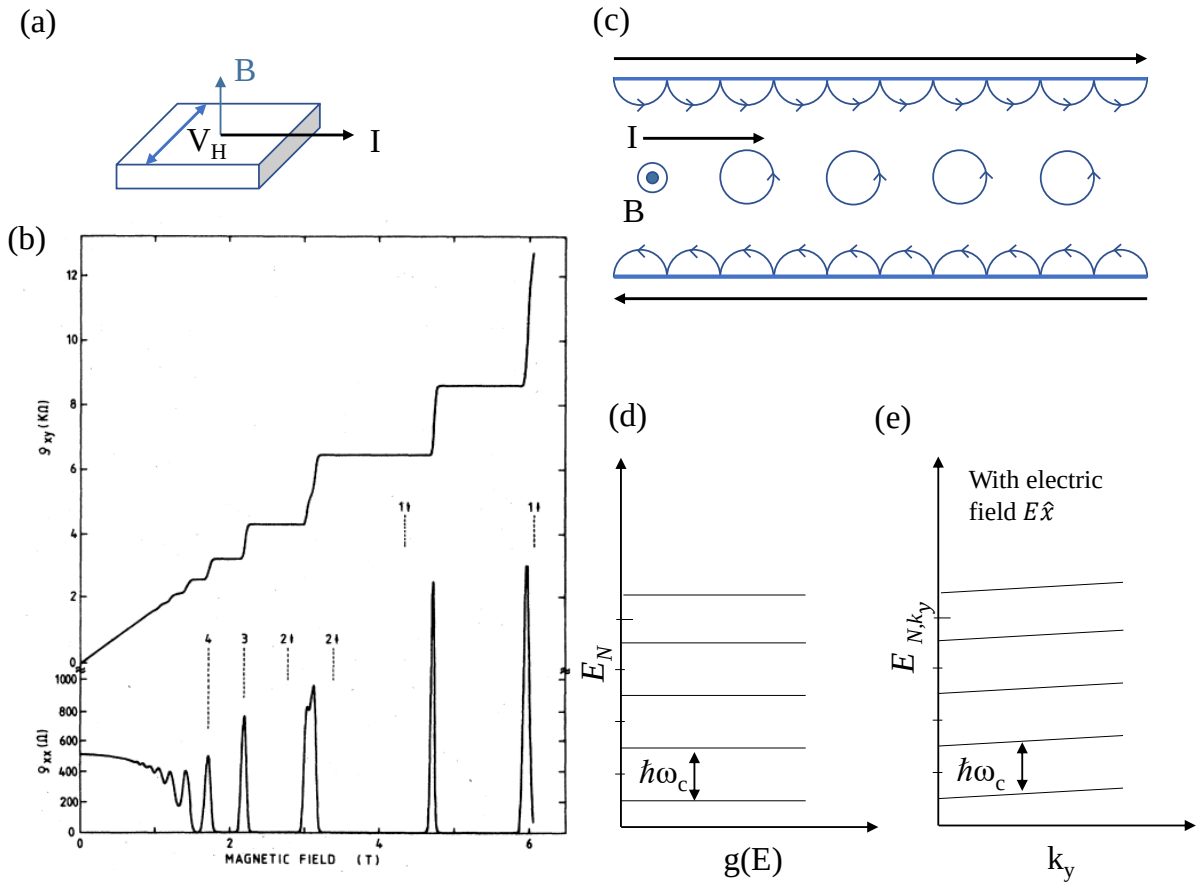

Figure 1.1: (a) Schematic of a Hall-effect set-up. (b) QHE as observed by K. V. Klitzing. The diagram is taken from Ref. [1]. (c) A simplified model demonstrating a quantum Hall state with insulating bulk (full circles) and conducting edge states (half circles at the edge). (d) Landau levels under magnetic fields. (e) Landau levels under external magnetic and electric fields.

R_{xy} in each of these plateaus can be expressed as $R_{xy} = h/Ne^2$ (N is an integer number). This quantization of R_{xy} was initially explained quantum mechanically by Landau levels [29].

1.1.1 Landau levels

The origin of Landau levels is related to the problem of the free electrons moving under a magnetic field **B**. The Lagrangian of an electron with charge -e, mass m, and velocity $\dot{\mathbf{x}}$ can be written as

$$L = \frac{1}{2}m\mathbf{x}^2 - e\mathbf{x}.\mathbf{A} \tag{1.1}$$

Here $\mathbf{A}$ is electromagnetic vector potential ($\mathbf{B} = \nabla \times \mathbf{A}$). Under gauge transformation of $\mathbf{A}$, there will be an additional term $\nabla\alpha$, considering α is a scalar field. However, this scalar field does not change the equation of motion, and the Lagrangian remains gauge invariant.

Next, we calculate the Hamiltonian from the Lagrangian:

$$H = \mathbf{x}.\mathbf{p} - L = \mathbf{x}.\frac{\partial L}{\partial \mathbf{x}} - L = \frac{1}{2m}\left(\mathbf{p} + e\mathbf{A}\right)^2 \tag{1.2}$$

Here, $\mathbf{p}$ is the canonical momentum. Considering $\mathbf{B} = B\widehat{\mathbf{z}}$, one can write $\mathbf{A} = Bx\widehat{\mathbf{y}}$ as a choice of Landau gauge. This way, the Hamiltonian in Eqn.1.2 becomes,

$$H = \frac{p_x^2}{2m} + \frac{1}{2m}\left(p_y + eBx\right)^2 \tag{1.3}$$

As our choice of Landau gauge makes the y-direction translational invariant and p_y and H are commutative, the $\mathbf{p_y}$ operator can be written as $\hbar k_y$:

$$H = \frac{p_x^2}{2m} + \frac{(\hbar k_y + eBx)^2}{2m} \tag{1.4}$$

The above Hamiltonian is quite similar to the Hamiltonian of a harmonic oscillator moving along the x-axis. Expressing Eqn.1.4 in a similar fashion, one can get:

$$H = \frac{p_x^2}{2m} + \frac{m\omega_c^2}{2}\left(x + k_y l_B^2\right)^2 \tag{1.5}$$

Here, $\omega_c = eB/m$ stands for cyclotron frequency of the circular orbits of electrons (Fig.1.1(c)) in the magnetic field $B\widehat{\mathbf{z}}$ and $l_B = \sqrt{\frac{\hbar}{eB}}$ represents the magnetic length. The Hamiltonian in Eqn. 1.5 is similar to a harmonic oscillator except for a shift of $k_y l_B^2$ along $x-$axis. The energy eigenvalue of the Hamiltonian will be

$$E_N = \hbar\omega_c \left(N + \frac{1}{2}\right) \tag{1.6}$$

A representation of such energy levels as a function of the density of states (DOS) is presented in Fig. 1.1(d). To sum up, the presence of magnetic field $B\hat{\mathbf{z}}$ on a free electron gas confines the electron DOS to equispaced energy levels known as Landau levels. Moreover, the number of available states in each Landau level is found to be BA/Φ_0. Here, A is the area of the sample, and $\Phi_0 = 2\pi\hbar/e$ is known as the flux quantum. For electrons, one needs to take the spin degeneracy ($S = 2$) into account, which will double the number of electrons in a Landau level to $2BA/\Phi_0$. When N number of Landau levels are filled with electrons, we observe a resistivity plateau at $R_{xy} = h/Ne^2$ in QHE. It is to be noted that Landau levels are comparable to an insulator as the filled and empty levels have $\hbar\omega_c$ energy gap. Despite that, we observe finite Hall resistance in QHE. To resolve this discrepancy, we need to take the electric field $E\hat{\mathbf{x}}$ applied during Hall measurements into account. Considering the electric potential $V = -Ex$, Eqn. 1.3 will now become

$$H = \frac{p_x^2}{2m} + \frac{1}{2m}\left(p_y + eBx\right)^2 + eEx \tag{1.7}$$

and the corresponding energy eigenstates become

$$E_{N,k_y} = \hbar\omega_c \left(N + \frac{1}{2}\right) - eE\left(k_y l_B^2 + \frac{eE}{m\omega_c^2}\right) + \frac{mE^2}{2B^2} \tag{1.8}$$

The eigenstates are now proportional to k_y. A visual representation of the Landau levels in presence of applied electric field is shown in Fig. 1.1(e). The group velocity of electrons become $v_y = \frac{1}{\hbar}\frac{dE_{N,k_y}}{dk_y} = -E/B$, meaning the electrons drift along $y-$direction. As a result, we observe quantized Hall resistance instead of insulating behavior.

1.1.2 Origin of edge states

Although the Landau levels explain the origin of quantized Hall resistance, there is another remarkable phenomenon called edge modes that occur in a quantum Hall state. The quantum Hall state develops a channel across the edge of a sample through which current flows without backscattering [30, 31]. A simplified description of the edge states is sketched

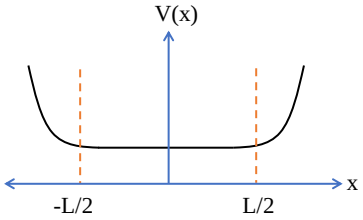

Figure 1.2: An illustration of the potential inside the system of width L. V_x is constant within the bulk of the sample $-L/2 \leq x \leq L/2$ and slowly starts to increase near the edge of the sample.

in Fig. 1.1 (d). When magnetic field B is applied perpendicular to the sample, the electrons move in cyclotron orbits inside the sample, which cause the bulk of the sample to become insulating. However, along the edge of the samples, the cyclotron orbits are not complete as the electrons collide with the boundary. The skipping orbits create a gapless channel through which the electrons are allowed to move in a specified direction. The opposite edges of the sample have electrons flowing in opposite directions. Such regulated motion of electrons across the edge of the samples are known as chiral edge channels.

To understand the origin of edge channels quantum mechanically, we consider a potential $V(x)$ inside the sample (Fig. 1.2). Performing Taylor expansion on $V(x)$ one can write $V(x) = V(X_0) + \frac{dV}{dx}(x - X_0) + ...$ Ignoring the quadratic term, We can assume $V(x) \propto x$. Considering $V(x)$ in the Hamiltonian we get,

$$H = \frac{p_x^2}{2m} + \frac{1}{2m}\left(p_y + eBx\right)^2 + V(x) \tag{1.9}$$

The above Hamiltonian is identical to that of Eqn. 1.7, where electric field $E(\hat{x})$ is applied on the system. As a result, we will get a similar drift velocity of electrons, $v_y = -\frac{1}{eB}\frac{dV}{dx}$ along the $y-$axis. For $x < 0$, $v_y > 0$ and $v_y < 0$ for $x > 0$. This explains the opposite current flow in the opposite edges of the sample in a chiral manner. Further derivation of the current flow I_y will give us $I_y = -e/2\pi \int v_y dk_y = e/2\pi \int \frac{1}{eB}\frac{dV}{dk_y} = \frac{e}{h}\Delta V$. Here ΔV stands for the potential difference between the two edges of the sample, which can be written as $\Delta V = eV_H$ in terms of Hall voltage. In this manner, Hall resistance $R_{xy} = V_H/I_y = h/e^2$. While discussing the Hall current, one needs to incorporate the contribution of the electric field discussed in Eqn. 1.7 with the edge potential. In this scenario, the potential will appear as Fig. 1.3.

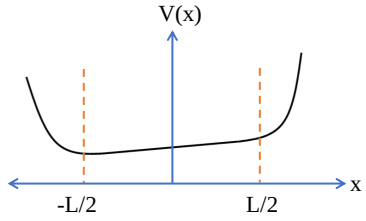

Figure 1.3: Potential as a function of sample width with consideration of electric field

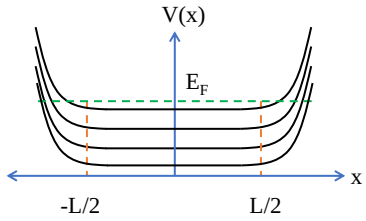

Figure 1.4: Potential under magnetic and electric fields.

However, the addition of an electric field does not change the I_y as long as the variation of $V(x)$ with x is small, and the Hall resistance remains quantized. Fig. 1.4 demonstrates the inclusion of the potential $V(x)$ to the Landau levels. As it can be seen, There are now N number of chiral edge channels for N number of filled Landau levels.

1.1.3 TKNN invariant

As mentioned earlier, one of the main attractive features of the chiral edge channels in QHE is that they flow dissipationless currents. These channels are robust and can survive disruptions like impurities. This overall quantization of the Hall current and the robust chiral edge states has a topological aspect to it. Moreover, quantized Hall resistance is also observed without any magnetic field in some materials (QAH insulators), which can not be solely explained by the Landau levels. This is where the theory developed by D.J. Thouless, M. Kohmoto, M.P. Nightingale, and M. Den Nijs (TKNN) in 1982 [27] comes into play. According to the TKNN theory, the Hall conductivity σ_{xy} can be expressed in terms of the total Berry curvature $\Omega(\mathbf{k})$ of the Bloch wave function ($|u_m(\mathbf{k})\rangle$) over the whole Brillouin zone (BZ) of a two-dimensional crystal showing QHE.

$$\sigma_{xy} = \frac{Ne^2}{h} = \frac{e^2}{h}\frac{1}{2\pi}\oint \Omega(\mathbf{k})d^2\mathbf{k} \tag{1.10}$$

Here the term $\frac{1}{2\pi}\oint \Omega(\mathbf{k})d^2\mathbf{k}$ is a topological invariant also known as TKNN invariant. To get a better understanding of the above term, we briefly introduce Berry curvature $\Omega(\mathbf{k})$ in the next section.

1.1.4 Berry curvature

According to Bloch's theorem, the eigenfunction of an electron inside a periodic crystal lattice is $|\psi_n(\mathbf{k})\rangle = e^{i\mathbf{k}.\mathbf{r}}|u_n(\mathbf{k})\rangle$ [32]. For $\mathbf{K}$ being the reciprocal lattice vector, then $|u_n(\mathbf{k})\rangle = |u_n(\mathbf{k}+\mathbf{K})\rangle$ and the corresponding energy eigenvalues $E_n(\mathbf{k}) = E_n(\mathbf{k}+\mathbf{K})$. Berry phase is a geometric phase that arises when the Hamiltonian $H(\mathbf{R})$ of a system undergoes an adiabatic cycle. In this process, the parameter $\mathbf{R}(t)$ evolves in a path that it returns to its initial value, $\mathbf{R}(t=T) = \mathbf{R}(t=0)$, after a duration of time T. Along the path, the eigenstate $|\psi_n(\mathbf{T})\rangle$ acquires an additional phase of γ_c over $|\psi_n(\mathbf{0})\rangle$. This additional phase is known as Berry phase [33] and expressed as:

$$\gamma_c = i\int_{R(0)}^{R(T)} d\mathbf{R}\,\langle u_n(\mathbf{R})|\,\nabla_{\mathbf{R}}\,|u_n(\mathbf{R})\rangle = i\oint d\mathbf{R}\,\langle u_n(\mathbf{R})|\,\nabla_{\mathbf{R}}\,|u_n(\mathbf{R})\rangle \tag{1.11}$$

When we consider the Berry phase over the whole BZ of a crystal,

$$\gamma_c = i\oint d\mathbf{k}.\,\langle u_n(\mathbf{k})|\,\nabla_{\mathbf{k}}\,|u_n(\mathbf{k})\rangle = \oint d\mathbf{k}.\mathbf{A}(\mathbf{k}) \tag{1.12}$$

$A(\mathbf{k}) = i\,\langle u_n(\mathbf{k})|\,\nabla_{\mathbf{k}}\,|u_n(\mathbf{k})\rangle$ is known as Berry connection. Under gauge transformation $\mathbf{A}(\mathbf{k})$ transforms into $\mathbf{A}(\mathbf{k}) + \nabla_{\mathbf{k}}\beta(\mathbf{k})$. However, the Berry phase remains invariant as the above equation transforms into,

$$\gamma_c = \int_S d^2\mathbf{k}.\nabla_{\mathbf{k}} \times \mathbf{A}(\mathbf{k}) \tag{1.13}$$

by Stokes' theorem. And $\nabla_{\mathbf{k}} \times \nabla_{\mathbf{k}}\beta(\mathbf{k}) = 0$. The term $\nabla_{\mathbf{k}} \times \mathbf{A}(\mathbf{k}) = \Omega(\mathbf{k})$ is known as Berry curvature. One interesting feature of the Berry curvature is that the closed loop integral of $\Omega(\mathbf{k})$ over the BZ is an integral multiple of 2π.

$$\int_{BZ} \Omega(\mathbf{k})d^2\mathbf{k} = 2\pi C \tag{1.14}$$

Here C is a topological invariant known as Chern number [27]. Comparing with Eqn. 1.10, the Chern number equals to the integer number N in quantized Hall conductivity σ_{xy}.

The reason C is called a topological invariant is rooted in a branch of mathematics known as topology. Topologically, the geometry of any two objects is identical as long as they can be transformed into each other under continuous deformation. For example, a donut and a cup have one hole in their geometry and are considered topologically identical, whereas a plate has no hole and falls under different topological classes. In this case, the number of holes in the geometrical object is a topological invariant known as genus number g. Both donut and cup have genus number $g = 1$ and belong to the same topological class, while a plate falls in a different topological class with $g = 0$. According to the Gauss bonnet theorem [34] in differential geometry, the total Gaussian curvature K of an enclosed surface S is

$$\int_S K dA = 2\pi\chi \tag{1.15}$$

χ is a topological invariant. χ represents Euler characteristic of the surface S, which is related to g [35]. When examined closely, the above equation resembles Eqn.1.14.

In a similar fashion to the Euler characteristic, the Chern number (C) topologically classifies different phases of matter in condensed matter physics. Here, the systems whose Hamiltonian can be transformed into one another by following an adiabatic path fall under the same topological class. This way, all topological insulators with a finite gap between conduction and valence bands are topologically equivalent. In contrast, the gap between the conduction and valence band vanishes at the edge of the quantum Hall insulator. As a result, the Hamiltonian of a quantum Hall insulator can no longer be transformed into the Hamiltonian of an ordinary Hall insulator, making the QH phase topologically distinct from the trivial insulator.

1.2 Quantum spin Hall Insulator (QSH)

As QHE is a quantized version of the Hall effect, the QSH effect is a topological phase of matter that can be considered a quantized version of the spin Hall effect. Spin Hall

effect is a phenomenon that appears in a two-dimensional system with strong spin-orbit coupling (SOC) [36]. SOC causes the spin-up and spin-down electrons to gather at the opposite faces of the samples. As a result, there will be a non-zero spin current between the two opposite sides of the sample. In short, the spin Hall effect is the spin version of the Hall effect, where Hall current is replaced by spin Hall current. However, unlike the Hall effect, no external magnetic field is required in the spin Hall effect. Similarly, the QSH effect does not require any external field. Unlike QHE, the TRS is preserved in QSH state [2, 37, 38]. Here, the SOC causes the electrons with up and down spins to flow in opposite directions across the edge channels of the 2D samples. As a result, the net edge current is zero, but the spin current remains non-zero due to spin accumulations on the opposite edges of the sample. A comparison of QHE and QSH effect can be found in Fig. 1.5.

QSH state was first realized by B. A. Bernvig, T. L. Hughes, and S. C. Zhang [2] in a semiconductor quantum well designed with an HgTe layer sandwiched between two CdTe layers. Due to the strong spin-orbit interaction in HgTe, the bands of HgTe becomes quite different from CdTe(see Fig. 1.6(A)). While for CdTe, the $p-$orbital bands (Γ_8) stay below the Fermi level and the $s-$orbital band (Γ_6) above the Fermi level, the bands invert for HgTe with Γ_8 going above and Γ_6 coming below the Fermi level. However, this band inversion can only appear above a particular thickness of the HgTe Layer d_c. Below d_c, the HgTe bands are oppressed by CdTe, and band inversion does not occur. Fig. 1.6(B) shows band dispersion of the subbands calculated with consideration of Γ_6, Γ_8 bands and $m_J = \pm 1/2, \pm 3/2$ at different HgTe layer thickness d. For $d < d_c$, the band gap is open. With an increase in HgTe Layer thickness, the energy gap between the top and bottom subbands decreases and becomes zero at $d = d_c$. The band inversion takes place above d_c. The purple color region in Fig. 1.6(B) is from band mixing of the top (blue) and bottom (red) bands. The zero energy gap at $d = d_c$ stops the Hamiltonian

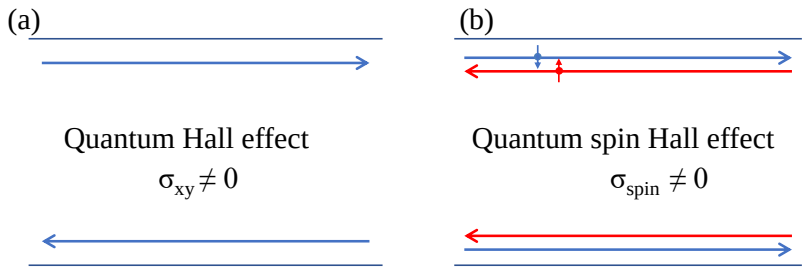

Figure 1.5: Comparison between QHE and QSH effect.

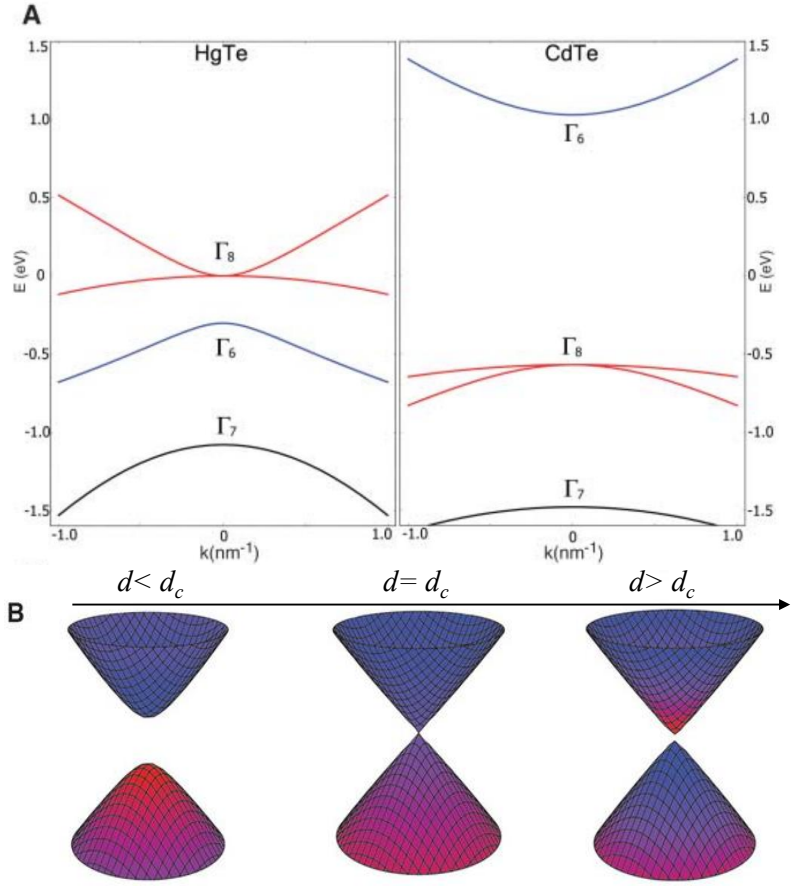

Figure 1.6: (A) The band structure of HgTe and CdTe with SOC. (B) Changes in band dispersion with HgTe layer thickness. (The diagrams are collected from ref. [2].)

above and below d_c from transforming into one another under continuous deformation. As a result, the state after band inversion becomes topologically distinct from $d < d_c$. This topologically distinct phase of matter is known as the QSH state or 2-D topological insulating state. Across the interface of HgTe and CdTe, the spin-up and spin-down electrons flow in opposite directions. The net current through the edge channel is zero, but a quantized spin Hall conductance of $\sigma_{spin} = 2e^2/h$ is observed.

1.2.1 Z_2 invariant

Since the net Hall current across the edge channels is zero in the QSH state, the Chern number (C) becomes $C = 0$. Hence, the QSH phase can not be defined just by the TKNN invariant. This is where Z_2 topological invariant comes into play. Unlike QHE, TRS is

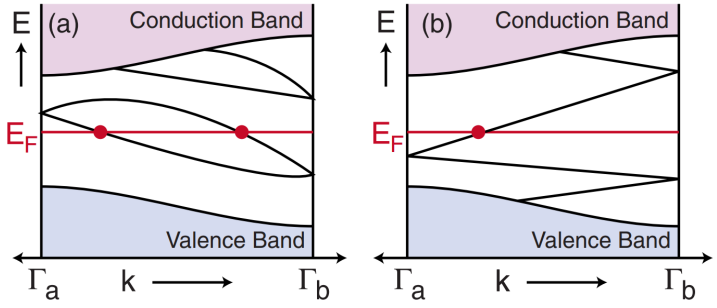

Figure 1.7: Band dispersion between the BZ range $\Gamma_a = 0$ to $\Gamma_b = \pi/a$ for (a) topologically trivial insulator with the edge states crossing the Fermi level for even number of times and (b) topologically non-trivial insulator with the topologically protected edge states crossing the Fermi level for an odd number of times. The image is collected from [3]

preserved in the QSH state and has a significant effect in defining this new topological invariant. TRS symmetry can be expressed in terms of an antiunitary operator $\Theta = e^{i\pi S_y/\hbar}K$. Here S_y represents the y-component of the spins of spin-1/2 particles, and K stands for the complex conjugation. For a system where TRS symmetry is preserved, the Bloch Hamiltonian $H(\mathbf{k})$ follows:

$$\Theta H(\mathbf{k})\Theta^{-1} = H(-\mathbf{k}) \tag{1.16}$$

All of these TRS invariant systems fall under two topological classes, $\nu = 0$ or 1. ν is the Z_2 topological invariant [37]. The TRS operator $\Theta^2 = -1$ for spin-1/2 electrons, which is why the TRS invariant Hamiltonians follow Kramer's theorem and have doubly degenerate eigenstates. The TRS-protected $\mathbf{k}$ points are doubly degenerate in nature, and the degeneracy disappears away from these particular points of the BZ due to SOC. Considering an edge state crosses the Fermi level at $\mathbf{k_x}$, a Kramer partner will be at $-\mathbf{k_x}$. The number of such Kramer's pair crossing the Fermi level defines the change of the topological invariant $\Delta\nu$. $\Delta\nu = 0$ for even number of crossings and $\Delta\nu = 1$ for odd number of crossings. The system is considered topologically trivial for $\Delta\nu = 0$ and topologically non-trivial for $\Delta\nu = 1$. The comparison of band dispersion with $\Delta\nu = 0$ and 1 is presented in Fig. 1.7.

Furthermore, the Z_2 topological invariant ν can be mathematically defined by an unitary matrix W whose coefficients are

$$W_{nm} = \langle u_m(\mathbf{k})| \Theta |u_m(\mathbf{k})\rangle \tag{1.17}$$

Here $|u_m\rangle$ is the Bloch wave function. Considering Γ_j is TRS symmetry protected $\mathbf{k}$ point, we define [3, 39]

$$\delta_j = \frac{Pf[W(\Gamma_j)]}{\sqrt{Det[W(\Gamma_j)]}} = \pm 1 \tag{1.18}$$

Then Z_2 invariant ν can be expressed in terms of δ_j as

$$(-1)^{\nu} = \Pi_{j=1}^{4} \delta_j \tag{1.19}$$

1.3 Three-dimensional topological insulator

Soon after the discovery of the QSH or 2D topological insulating state, scientists found its three-dimensional counterpart, where topologically protected edge states were replaced by 2D TSSs. In contrast to the QSH state, the classification of 3D TIs [3, 40, 41] involves four Z_2 topological invariants: ν_0, ν_1, ν_2, and ν_3. These invariants can be derived from the TRS protected $\mathbf{k}$ points in the BZ using the Eqn. 1.19 for QSH state, except now there will be eight time-reversal invariant $\mathbf{k}$ points instead of four. Among the four Z_2 invariants, ν_0 defines strong TI state ($\nu_0 = 1$) and weak TI state ($\nu_0 = 0$). (ν_1, ν_2, ν_3) represents the miller indices of the plane along which the topologically protected $\mathbf{k}$ points

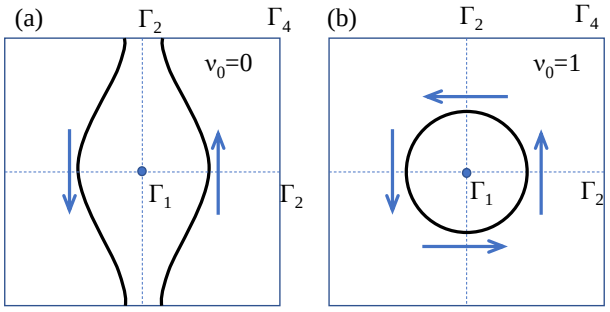

Figure 1.8: A demonstration of the surface bands on the Fermi surface of (a) weak TI and (b) strong TI. Γ_1, Γ_2, Γ_3, Γ_4 are the time-reversal invariant $\mathbf{k}$ points on the surface BZ.

appear. For strong TI, the surface bands are TRS protected. The surface states in strong TI enclose odd number time reversal invariant points. The illustration in Fig. 1.8(b) shows a simpler model with surface bands enclosing one Kramer's point (here Γ_1) in a 3D TI. For $\nu_0 = 0$, nontrivial topological properties manifest primarily in specific directions as these systems are stacks of two-dimensional QSH insulators. The chiral edge states of individual QSH insulator layers collectively give rise to non-trivial surface states along the stacking direction. Unlike the TRS protected robust bands in strong TIs, the surface bands are significantly less robust and vulnerable to defects and weak inter-layer coupling. Fig. 1.8(a) gives an example of the surface bands in weak TIs.The arrows in Fig. 1.8 mark the spin directions in the surface states across the BZ. To preserve the TRS in strong TI, the surface band spins along the positive and negative axis of the BZ become opposite to each other. This way, the Hamiltonian $H(\mathbf{k})$ follows Eqn. 1.16. In Fig. 1.8(b), the spin rotates by 2π over the enclosed surface state. However, TRS only requires rotation of π. The additional rotation of π is the non-zero Berry phase for the strong TI.

$Bi_{1-x}Sb_x$ is the first discovered 3D TI with TSS [4]. While the topological nature of 3D TI surface states is difficult to observe from Hall measurements, one can easily probe these surface states through ARPES measurements. Fig. 1.9(a) demonstrates the band structure of $Bi_{1-x}Sb_x$ along (111) plane for $0 < x < 0.03$. $Bi_{1-x}Sb_x$ has rhombohedral ($R\bar{3}m$) crystal structure. When projected along (111) plane. The L point of the BZ falls on the $\bar{M}$ point (Fig. 1.9(d)). At the L point of pure Bi, the conduction band is formed by symmetric orbitals L_s, while the valence bands consist of antisymmetric orbitals L_a (Fig. 1.9(a)). The band structure of pure Sb closely resembles that of Bi, except for L_s becoming the valence band and L_a becoming the conduction bands (Fig. 1.9(c)). The band dispersion near the L point follows the Dirac equation and exhibits almost linear behavior. As seen from Fig. 1.9(a), a small band gap exists between L_a and L_s. This band gap disappears at around $x \sim 0.4$, and the band dispersion can be expressed by a massless Dirac equation. This is where the system starts to enter into the topologically non-trivial state. Above $x = 0.04$, the band inversion between L_s and L_a takes place, and the band gap opens up again. For $x > 0.07$, the system becomes insulating with the lowering of the valence band at the T point (Fig. 1.9(b)). Within $0.07 < x < 0.22$, the system becomes a TI [42], that is insulating in bulk with the conducting surface bands [the black lines in Figs. 1.9(a)-(c)] connecting the valence and conduction bands. It is to be noted that for $x < 0.03$, the surface bands cross the Fermi level for an even number of times, while the count became odd for $0.07 < x < 0.22$. In the ARPES data obtained for

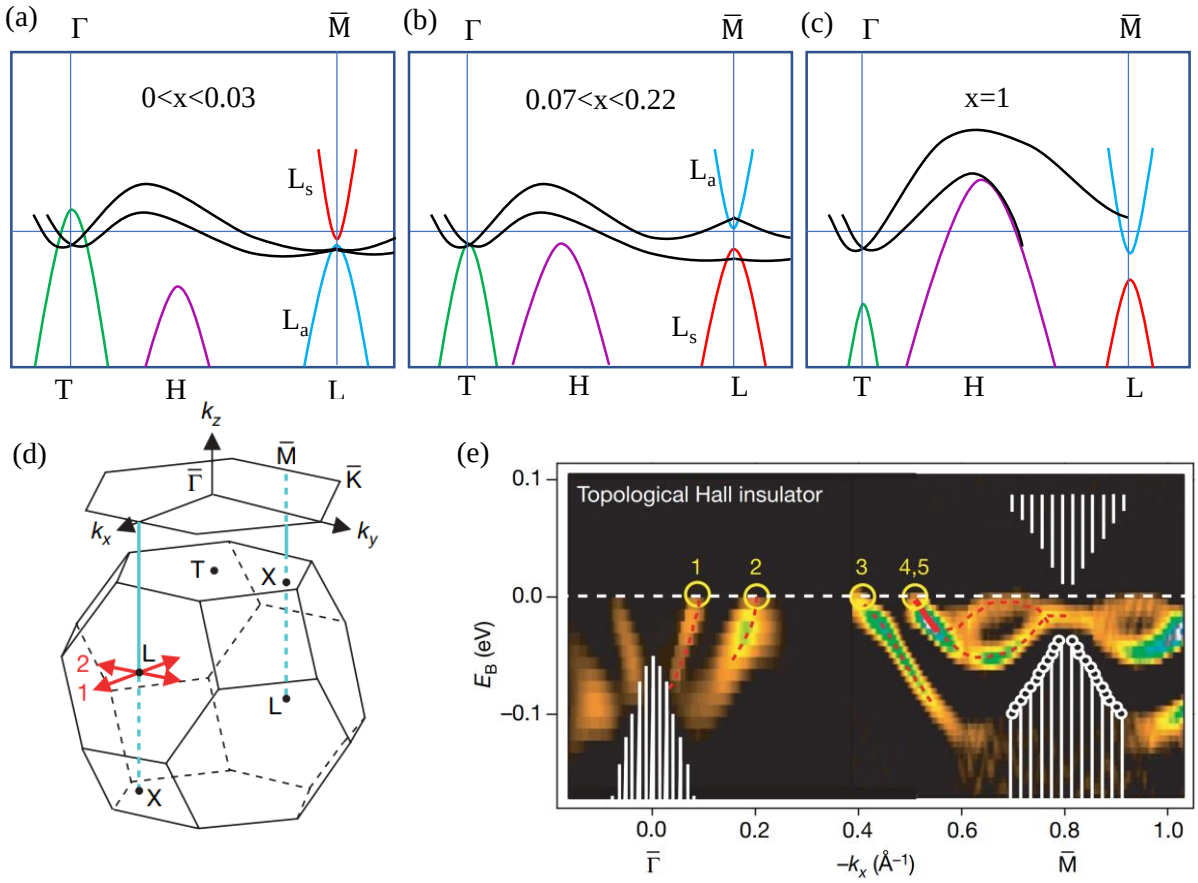

Figure 1.9: (a)-(c) Schematic diagram demonstrating the bulk and surface band structure of $Bi_{1-x}Sb_x$ with increasing x. (d) BZ of $Bi_{1-x}Sb_x$ and its 2D projection along (111) planec [4]. (e) First observation of gapless TSSs along (111) plane for x=0.1 from ARPES measurements [4].

$Bi_{0.9}Sb_{0.1}$ [4], the surface bands are observed to cross the Fermi level five times within the Γ-$\bar{M}$ region. As previously discussed, surface bands crossing the Fermi level for an odd number of times are considered topologically protected. Therefore, the observed surface bands in $Bi_{0.9}Sb_{0.1}$ are indeed topologically protected. Above $x = 0.22$, the valence band at H goes above the conduction band minima, and $Bi_{1-x}Sb_x$ becomes semimetallic again (Fig. 1.9(c)). Further, an increase in Sb causes the surface states to gradually faint near the $\bar{M}$ point (Fig. 1.9(c)).

The TSSs of $Bi_{1-x}Sb_x$ were rather complicated. The search for TIs with simpler surface states and larger band gaps continued until the discovery of Bi_2Se_3 family of materials [41, 43, 44]. Bi_2Se_3 is a 3D TI with a large 0.3 eV band gap. Such a large band gap makes it possible to observe topological properties even at room temperature. Following the

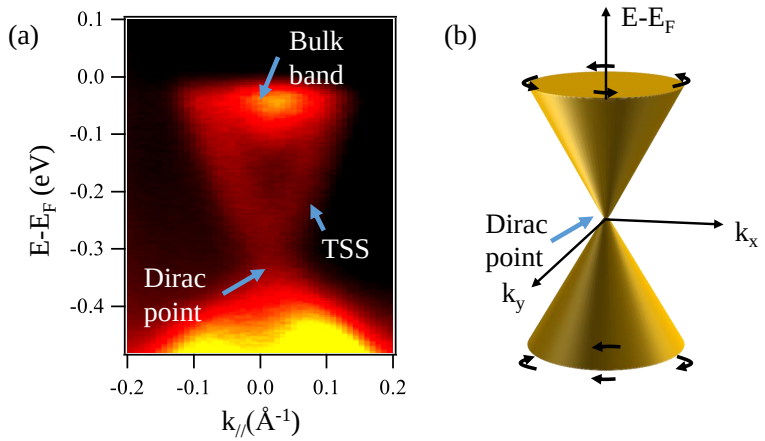

Figure 1.10: (a) Band structure of 3D TI Bi_2Se_3 observed from ARPES. (b) The TSSs marked in (a) form a Dirac cone in k_x-k_y plane. The arrows represent the spin directions throughout the BZ.

discovery of a topological insulating state in Bi_2Se_3, similar topological properties were identified in its isostructural Bi_2Te_3 [43] and Sb_2Te_3 [41] systems. In these materials, the band dispersion of the TRS protected surface bands is quite simple in nature (Fig. 1.10(a)). They exhibit linear dispersion following the Dirac equation and cross the Fermi level at a single point to form a Fermi circle around the Dirac point. This behavior is similar to the depiction in Fig. 1.8(b). Additionally, in $Bi_{1-x}Sb_x$ the composition varies with the substitution of Sb for Bi, leading to the potential transition from topologically non-trivial to trivial phases depending on the substitution amount. Whereas Bi_2Se_3 represents a chemically pure compound. This inherent purity simplifies the process of growing single crystals, reducing the likelihood of impurities and disorder in the crystal lattice. Although topologically protected bands are robust against disorder, the higher purity of Bi_2Se_3 family of materials helps to observe the TSS with better resolution through the ARPES measurements.

1.4 Quantum anomalous Hall insulator

The anomalous Hall effect (AHE) is a phenomenon observed in magnetic materials with broken TRS. The magnetization of the material gives rise to a Hall current without any external field. Similar to the quantized version of the Hall effect, one could wonder about the quantization of anomalous Hall conductivity σ_{xy} without any external field. In

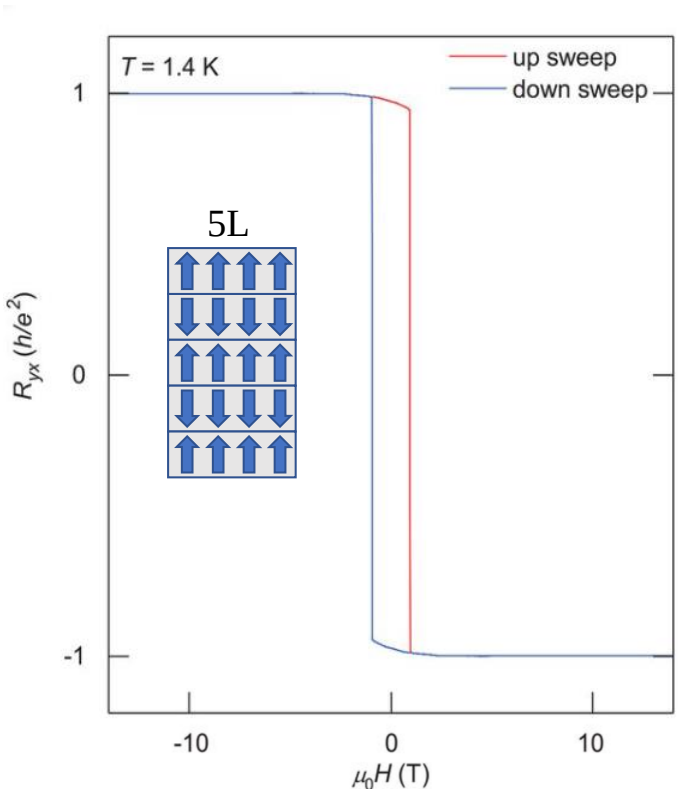

Figure 1.11: QAH effect observed in five-Layer $MnBi_2Te_4$ film (Collected from [5]).

support of this notion, F.D.M. Haldane designed a 2D honeycomb lattice model in 1988 that shows quantized σ_{xy} at zero external fields [45]. However, prior to the discovery of the QSH or 2D topological insulating state, experimental observation of the QAH state remained elusive. As discussed before, the QSH state does not break the TRS symmetry. Here, the opposite spin electrons move in the opposite direction through the edge channels of the samples, generating a quantized spin current along the way. The main idea was to introduce magnetism to these QSH systems for realizing QAH state [46]. On that note, Mn ions were doped in HgTe/CdTe quantum Wells, but the system remained a paramagnet with intact TRS [47]. The first observation of the QAH state was made by doping magnetic element Cr into a thin film of three dimensional TI $(Bi, Sb)_2Te_3$ [48] in 2013, which was followed by the observation of the QAH effect in V-doped $(Bi, Sb)_2Te_3$ thin film in 2015 [49]. Magnetic doping achieved the QAH effect at mK range temperature and ultimately compromised the sample quality, which posed challenges for both experimental investigations and practical applications of the QAH state. Considerable efforts were devoted to discovering three-dimensional TIs with

intrinsic magnetism to help realize QAH states at higher temperatures. $MnBi_2Te_4$ is one such TI with intrinsic AFM ordering, where the QAH effect is observed for odd no. of layers [5]. Recently, the QAH effect has also been found in non-magnetic Moiré superlattices like twisted bilayer graphene [50–52] and transition-metal dichalcogenide heterostructures [53], where orbital magnetic states give rise to the QAH state.

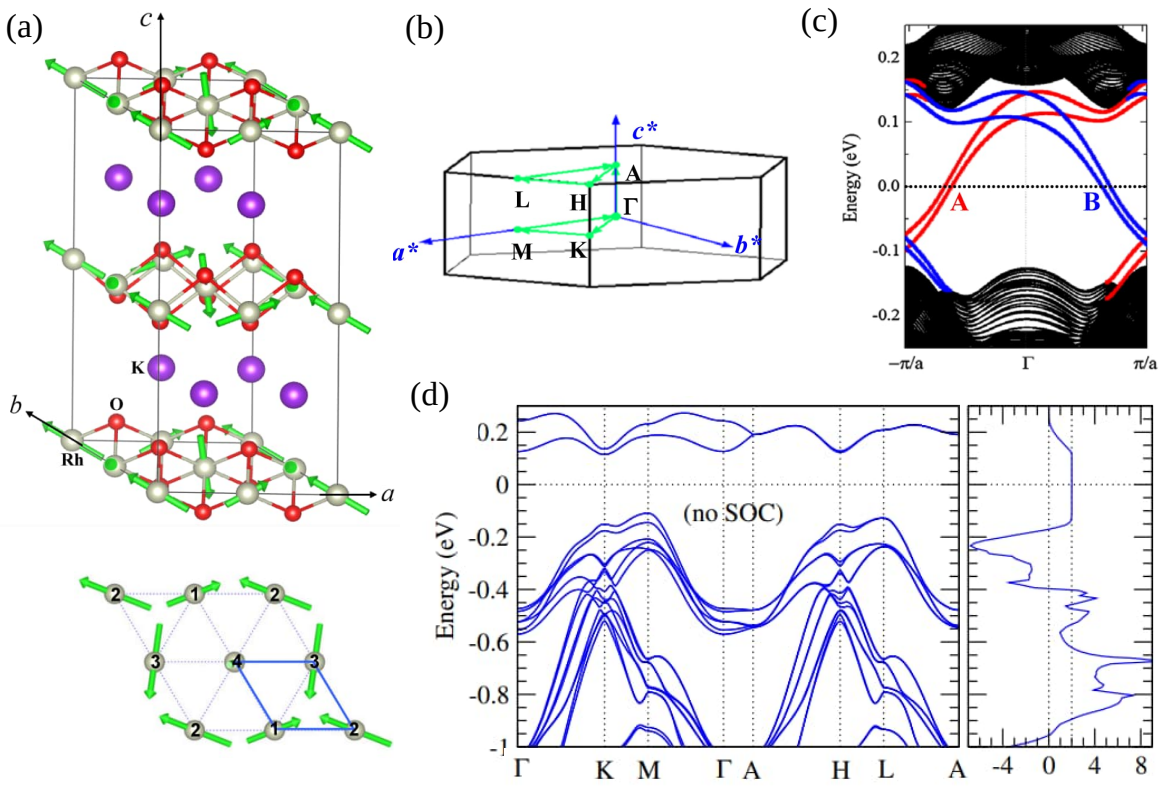

Figure 1.12: (a) Crystal structure of $K_{0.5}RhO_2$. The green arrows represent the magnetic moments of the Rh atoms. The projection of magnetic ordering along $ab-$plane is presented in the lower panel. (b) The Hexagonal BZ of $K_{0.5}RhO_2$. (c) The band structure of $K_{0.5}RhO_2$ nano-ribbon along $a-$axis. The bands marked as A and B are the chiral edge states from opposite sides of the ribbon. The bulk bands are presented in black. (d) The bulk band structure of $K_{0.5}RhO_2$ without SOC. The calculated anomalous Hall conductivity shows quantization of ($\sigma_{AH} = 2e^2/h$) over the insulating region. All images are collected from [6]

Moreover, in 2015, researchers predicted the existence of a QAH insulating state in $K_{0.5}RhO_2$ when it adopts a non-coplanar chiral AFM configuration [6]. The crystal struc-

ture of $K_{0.5}RhO_2$ is hexagonal as shown in Fig. 1.12(b) (space group $P6_3/mmc$), and the magnetization arises from the Rh atoms. The considered non-coplanar AFM arrangement of Rh magnetic moments is depicted in Fig. 1.12(a). Utilizing first-principles calculations below the Néel temperature, quantized anomalous Hall conductance of $\sigma_{AH} = 2e^2/h$ was found. In Fig. 1.12(d), the bulk band structure exhibits insulating behavior with a constant band gap of 0.22 eV over the BZ. The quantized Hall conductance is attributed to the presence of edge states in Fig. 1.12(c). It is worth mentioning that the quantized Hall conductivity remains unchanged both with and without SOC. This observation has led researchers to the conclusion that the observed quantized σ_{AH} is a result of the existence of an exotic topological phase known as quantum topological Hall state in the $K_{0.5}RhO_2$ system.

Magnetic TI films such as Cr doped $(Bi, Sb)_2Te_3$ and $MnBi_2Te_4$ films host massless Dirac cones at the top and bottom surfaces that are protected by TRS. In the presence of magnetism, the TRS is broken, and the surface state spins, coupled with the moments of the magnetic ions. This coupling results in an additional mass term to the surface state Hamiltonian that opens up a gap at the Dirac point. The massive Dirac cones lead to a Hall conductivity of $\pm e^2/2h$ in each surface of the TI films. This phenomenon is known as surface half-QHE [45, 54]. When magnetic moments are oriented along the same direction in both the top and bottom surfaces of the TI film, the Hall conductivity components add up to a quantized Hall conductivity of e^2/h at zero fields. It is to be noted that only the surface magnetic order of the TI films plays a role in generating the QAH effect. For example, $MnBi_2Te_4$ is an intrinsic AFM. For odd no of layers, the magnetic moments of top and bottom surfaces are along the same direction [55, 56]. The moments inside the bulk do not affect the QAH effect, and clear quantized Hall conductance of e^2/h is observed in five-layer $MnBi_2Te_4$ films (Fig. 1.11). It is worth mentioning that the QAH effect manifests at significantly higher magnetic fields in pure $MnBi_2Te_4$ thin films.

1.5 Topological semimetals

As discussed before, TIs exhibit gapless surface states with Dirac-like dispersion with an insulating bulk band structure. Over the years, non-trivial band topology was also observed in semimetals [57–60]. Topological semimetals host linear dispersive bands at several high symmetry points of the BZ. These BCPs are protected by symmetries like

TRS and/or inversion symmetry (IS). Depending on the type of symmetry protection at the BCPs, topological semimetals are mainly classified into Dirac [23, 61–63] and Weyl [24, 58, 64]semimetals.

In relativistic quantum mechanics, the wave equation of a spin-1/2 particle can be written as

$$(i\hbar\gamma^{\mu}\partial_{\mu} - mc)\psi = 0 \tag{1.20}$$

Here $\mu = 0, 1, 2, 3...$ represents time and the dimension of the space, c is the velocity of light, and m is the mass of the particles. This equation is known as the Dirac equation derived by Paul Dirac in 1928 [65]. The fermions following the wave equation are called Dirac fermions. Considering these fermions without mass (m=0), Weyl derived two equations from the Dirac equation in 1929 [66].

$$i\partial_t\psi_{\pm} = \pm v\mathbf{p}.\sigma\psi_{\pm} \tag{1.21}$$

Here $\psi_{\pm}$ is two-component wave vector and the Hamiltonian

$$H_{\pm} = \pm v\mathbf{p}.\sigma \tag{1.22}$$

v is the velocity of the Weyl fermion, σ represents the pauli matrices and $\mathbf{p}$ stands for the crystal momentum. A WSM contains at least two BCPs, known as the Weyl points. These fermions exhibit opposite chiralities in accordance with the Hamiltonians H_+ and H_- in Eqn. 1.22. Each of these Hamiltonians has two eigenvalues $E = \pm vp$. The Weyl point appears at $p = 0$, where the eigenvalue becomes doubly degenerate. If the opposite chiral Weyl points have no separation in momentum, the system is transformed into a DSM. In this scenario, the BCP becomes a fourfold degenerate Dirac point.

Next, we focus on the Berry curvature of Weyl and Dirac semimetals to understand their topological nature. In a WSM, the pair of Weyl points with opposite chirality acts as the source (+) and sink (−) of the Berry curvature in momentum space. Between the Weyl points, the Berry phase γ_c becomes non-zero. This results into a non-zero Chern no. of $C = 1$ in a 2D momentum plane. Conversely, the Chern no. remains zero in momentum planes that do not lie between the Weyl nodes (Fig.1.13(a)). As for the Dirac point, it can be viewed as having two Weyl points coinciding with each other, resulting in a Chern number of $C = 0$. It is to be noted that both Dirac and Weyl nodes are very robust in

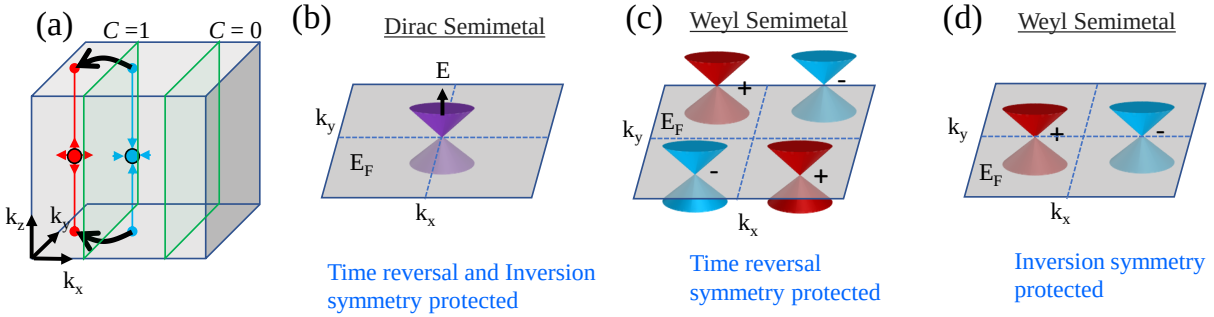

Figure 1.13: (a) Schematic representation of three-Dimensional momentum space in a Weyl semimetal (WSM). The red and blue circles in the bulk denote the Weyl points, acting as source and sink of Berry curvature, respectively. The projection of the Weyl points on the surface are connected by topological Fermi arcs (the black arrows on the top and bottom surface). The non-zero Berry phase between the Weyl nodes gives rise to Chern no. $C = 1$ for any momentum plane between the Weyl nodes and $C = 0$ for any other momentum plane. (b) The linear band dispersion in a DSM near the Dirac point protected by TRS and IS. (c) Band dispersion in a WSM protected by TRS. (d) Band dispersion in a WSM protected by IS.

nature due to their symmetry protection. In a DSM, the fourfold degenerate Dirac point is protected by both TRS and IS. However, WSM phase can only be obtained by breaking one of these two symmetries. When IS is broken, the TRS symmetry protects the Weyl points. Preserving TRS requires Weyl nodes in k and $-k$ momentum to be of the same chirality. To balance these same chirality Weyl nodes, a pair of opposite chirality appears. This way, four Weyl nodes exist in a TRS protected WSM (Fig. 1.13(c)). On the other hand, if TRS is broken in a WSM, the two opposite chirality Weyl nodes appear at the same energy value due to the IS protection (Fig.1.13(d)).

The non-trivial band topology originates topological surface states known as Fermi arcs in a WSM. The Fermi arcs are quite distinct from the TSS in a TI. In the case of TIs, the surface states form a close loop around the Dirac point (Fig. 1.10). In contrast, the Fermi arcs are not closed loops but open lines connecting the opposite chirality of Weyl points. ARPES is a very efficient technique for probing the surface Fermi arcs and identifying WSM phase. The topological Fermi arcs were first realized in WSM TaAs by ARPES measurements [58]. Subsequently, Fermi arcs were also detected in other compounds from the transition metal monopnictide family, such as NbP [67, 68] and NbAs [69]. Later, WSM phase was also observed in transition metal dichalcogenide [70, 71] $MoTe_2$ [72]. $MoTe_2$ belongs to a different WSM phase than TaAs. TaAs family of materials are

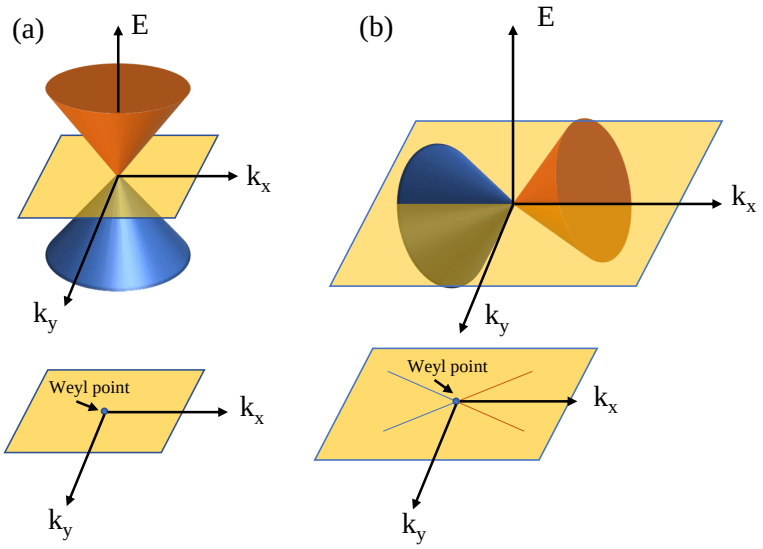

Figure 1.14: Schematic diagrams of (a) type-I WSM and (b) type-II WSM with the constant energy contours taken across the Weyl nodes.

type-I WSMs, which means that on a constant energy contour that passes through the Weyl node will have only one point will appear (Fig. 1.14(a)). Fig. 1.14(b) demonstrates the type-II Weyl node, which is observed in $MoTe_2$ and some other transition metal dichalcogenide compounds [73, 74]. Due to the tilting of the hole and electron-like bands near the Weyl point, the constant energy contour exhibits the Weyl point as a band touching point between the two bands.

The WSM phases observed in both the TaAs family and $MoTe_2$ family are achieved by breaking IS. As mentioned earlier, WSM phases can also be obtained by breaking the TRS. However, the observation of Fermi arcs in TRS-broken WSMs using ARPES is challenging. Nevertheless, TRS-broken WSMs are of significant interest due to their ability to exhibit a large AHE resulting from non-zero Berry curvature. This property is advantageous for designing memory devices, making these materials technologically relevant. An example of such TRS-broken WSM is Mn_3X (X = Sn, Ge, Ga) family of materials [7, 8, 75**?** –80]. These materials belong to the $P6_3/mmc$ space group and feature stacks of a Kagome lattice made of Mn atoms. In this structure, the Mn atoms create a non-collinear AFM ordering, breaking the TRS of the system and leading to the emergence of multiple Weyl points across the BZ. Fig. 1.15(a) depicts the distribution of TRS-broken Weyl points across the Fermi surface of Mn_3Sn. As shown in Fig. 1.15(b), the bands associated with the Weyl nodes near the $K-$ point become visible from ARPES data. These Weyl nodes in Mn_3Ge are responsible for inducing a Giant AHE [81]. Consequently, we conducted

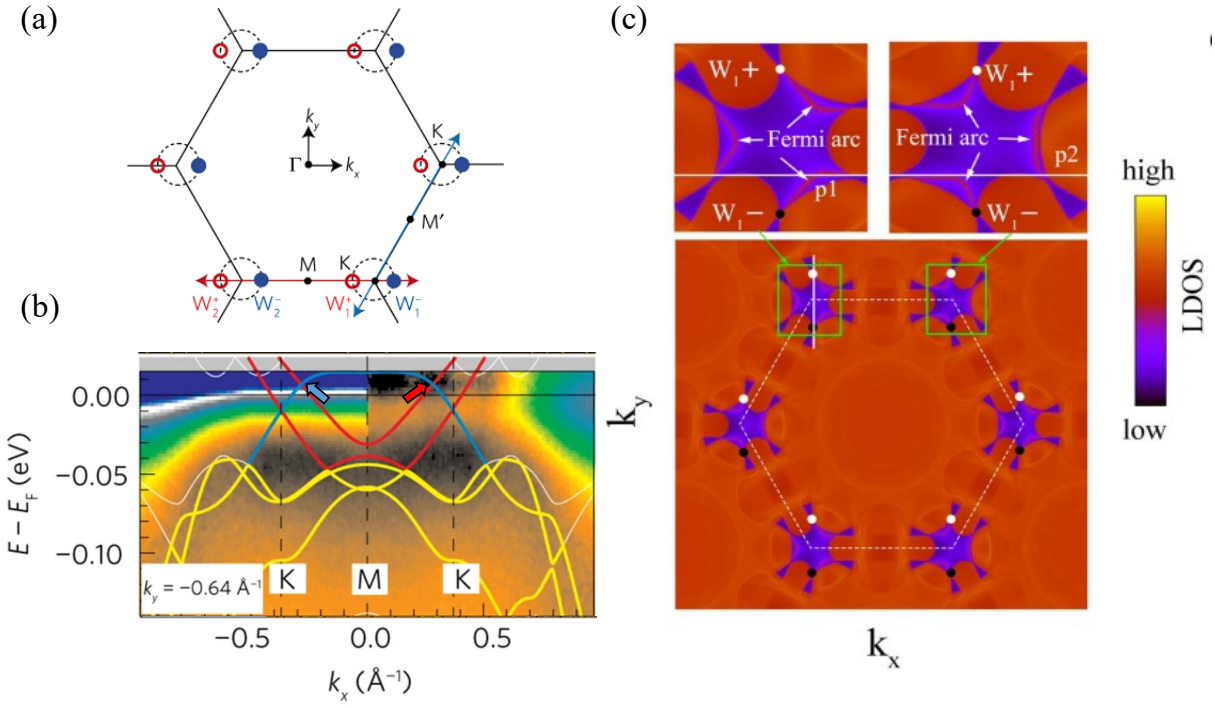

Figure 1.15: (a) Schematic diagram of the BZ of Mn_3Sn showing the positions of Weyl nodes near the Fermi level. (b) ARPES data of Mn_3Sn taken along $M - K$ direction, showing the bands generating the Weyl nodes. The red and blue arrows mark the Weyl nodes near the K points. (The diagram in (a) and (b) are collected from [7]) (c) Surface state calculation of Mn_3Ge demonstrating the Fermi arcs (taken from [8]).

ARPES measurements on Mn_3Ge to experimentally observe its electronic structure.

1.5.1 Topological semimetals with higher fold degeneracy

Dirac, Weyl, and Majorana fermions are the fundamental particles in high-energy physics. We have already explored the topological properties of condensed matter systems hosting Dirac and Weyl fermions. Similarly, Majorana fermions have also been observed in specific superconducting heterostructures [20, 22]. Apart from these three fundamental fermions, higher-fold degenerate fermions were also observed in condensed matter systems over the past few years [9–11, 26, 82]. In high-energy physics, fundamental particles are governed by the Poincaré symmetry [83], which includes space-time translation symmetry, spatial rotation symmetry, and Lorentz boosts. These symmetries preserve the consistency of physical laws across all observers within any inertial frame of reference. Conversely, the behavior of the particles in condensed matter systems is dictated by the specific crystal

symmetries among the 230 space groups [84]. The space group symmetries impose fewer constraints on the fermions compared to that of of Poincaré symmetry, providing the opportunity to explore novel quantum states that have no analogs in high-energy physics.

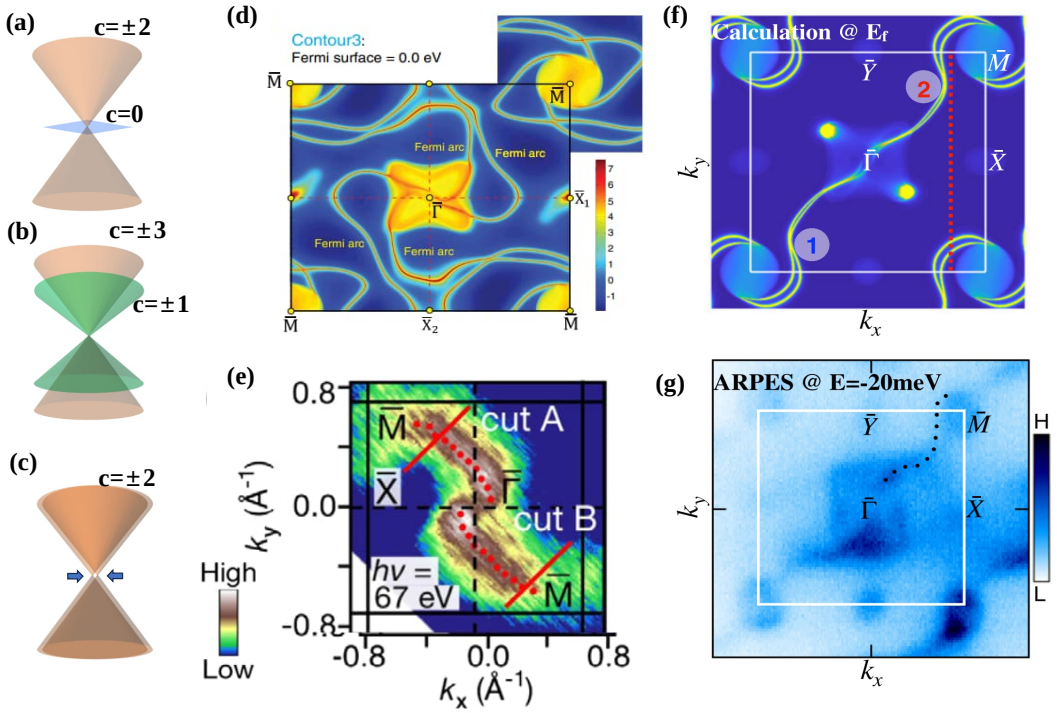

Figure 1.16: Schematic diagram showing the electronic structure at (a) spin-1 excitation, (b) spin-3/2 excitation, and (c) double Weyl fermions (The arrows in (c) indicate the overlap of the two BCPs). Fermi surface along (001) plane of CoSi obtained from (d) surface state calculations (collected from [9]) and (e) ARPES (collected from [10]). (f) Surface state calculation of RhSi along (001) plane (g) Fermi surface of RhSi observed via ARPES. (f)-(g) are collected from [11])

As a result, it is possible to obtain spin-1 excitations and Rarita-Schwinger-Weyl (RSW) excitations with spin-3/2 in a three-dimensional crystal lattice. Both spin-1 and spin-3/2 fermions can be described using the same Hamiltonian as shown by Eqn. 1.22, which characterizes spin-1/2 fermions, but with the replacement of Pauli matrices σ by spin matrices S for spin-1 and spin-3/2 fermions. For spin-1 fermions, these spin matrices are of 3×3 order, leading to three-fold degenerate BCPs with a Chern number $C = \pm 2$ (Fig. 1.16(a)) [26]. On the other hand, for RSW fermions, the spin matrices are 4×4 and generate a fourfold degenerate BCP with a Chern number $C = \pm 4$. At this BCP, two bands with Chern numbers $C = \pm 3$ and $C = \pm 1$ touch each other (Fig. 1.16(b)) [26, 85]. Furthermore, in the presence of TRS, four-fold degenerate fermions with a Chern number

$C = \pm 2$, known as double-Weyl fermions [9, 86], are also observed (Fig. 1.16(c)).

Compounds like $PdSb_2$, CoSi, and their isostructural materials were predicted to host such higher-fold degenerate fermions from the DFT calculations [9, 26, 87], which were later confirmed by ARPES measurements [10, 11]. The observation of Fermi arcs in CoSi and its isostructural compound RhSi is presented in Fig. 1.16(d)-(g). Both CoSi and RhSi crystallize in noncentrosymmetric cubic crystal structures ($P2_13$ space group) and exhibit spin-1 excitations at the center ($\bar{\Gamma}$) and double Weyl excitations at the corner ($\bar{M}$) of the BZ. Surface state calculations for CoSi (Fig. 1.16(d)) and RhSi (Fig.1.16(f)) along the (001) plane reveal connecting Fermi arcs between the bulk Fermi surfaces related to these higher-fold degenerate excitations. ARPES measurements further experimentally confirm the presence of these long Fermi arcs in both RhSi and CoSi. Additionally, the existence of such chiral fermions were also predicted in other transition metal monosilicides. In this thesis, we explore the electronic structure of the isostructural material FeSi to investigate its topological nature.

Chapter 2

Experimental details

2.1 Single crystal growth

Single crystals are the highly oriented crystalline materials with all atoms sitting on a continuous lattice that expands throughout the crystal in three diemensions. This characteristic of a single crystal allows us to examine the physical, electronic, and magnetic properties along different lattice planes of the crystal. The measurements reported in this thesis were carried out on single crystals of the following compounds: FeSi, $K_{0.65}RhO_2$, Bi_2Se_3, $Mn_{1-x}Sn_xBi_2Te_4$ and Mn_3Ge.

Single crystals of FeSi and $K_{0.65}RhO_2$ were grown by Dr. S. Aswartham and G. Shipunov in IFW Dresden, Germany [88, 89] via floating zone method [90, 91] and flux growth method [92, 93] respectively. Dr. Rabia Sultana prepared the single crystals of magnetically doped Bi_2Se_3 [94] in CSIR-NPL, Delhi, India. Mn_3Ge single crystals were grown by Susanta Ghosh in S. N. Bose National Centre for Basic Sciences using flux-growth technique. Therefore, the discussion on the above mentioned materials remains outside the scope of the thesis from a crystal growth point of view. As for $Mn_{1-x}Sn_xBi_2Te_4$, we used the flux growth technique to prepare the singles crystals with x=0,0.2,0.55,0.68,0.86 and 1 [95]. So in the next section, we briefly introduce the Flux growth method.

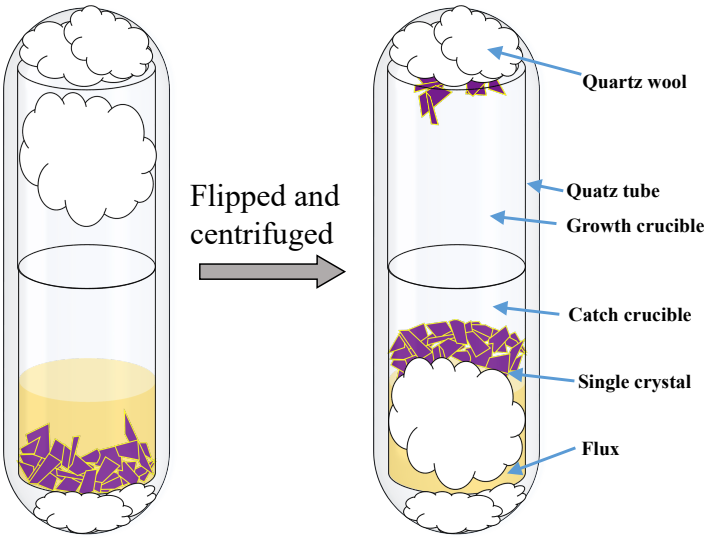

Figure 2.1: Illustration of Flux-growth technique

2.1.1 Flux growth method

Flux-growth technique is a commonly technique to grow high-quality single crystals of desired compositions. In this method, first the elements of desired composition are added crucible along with appropriate flux of necessary quantity. Here, the flux helps to reduce the melting point of the elements as the they completely can dissolve in the flux. The most commonly used crucibles in the laboratory are alumina (Al_2O_3), boron nitride (BN), graphite, and metal crucibles like tantalum (Ta), Platinum (Pt), Tungsten (W), etc. [96, 97]. Then depending on the type of crystals Oxide/Non-oxide, one needs to put the crucible inside a quartz ampule and vacuum seal it. The vacuum sealed quartz ampule is then kept inside the furnace in a specific temperature-profile that first dissolves the components in the flux. Then the nucleation is started during slow-cooling, after which the ampule is annealed at a particular temperature (also known as sample growth temperature) where the crystal forms. The ampule is then reversed and centrifuged to eliminate the excess flux from the single crystals. On that note, one can see from Fig. 2.1 there is a reversed crucible with quartz-wool inside that has been added on top of the chemical filled growth crucible. When the ampule is reversed and centrifuged, the melted chemicals in the growth crucible fall on the glass wool of the second crucible (marked as catch crucible in the left figure in Fig. 2.1). The glass wool works as a net that catches the crystals and lets the liquid flux pass through, and we collect shiny crystals of the desired material after breaking the quartz tube.

2.2 Composition characterization

2.2.1 Energy dispersive X-ray analysis (EDS)

Energy dispersive X-ray spectroscopy, also known as EDS or EDAX, is generally used to identify the elemental composition of the prepared materials. Here, elemental analysis of the sample is performed by stimulating the emission of characteristic X-rays by focusing an electron beam on the sample. The obtained characteristic X-rays reveal the elements present in the sample along with their weight percentage.

Characteristic X-ray generation

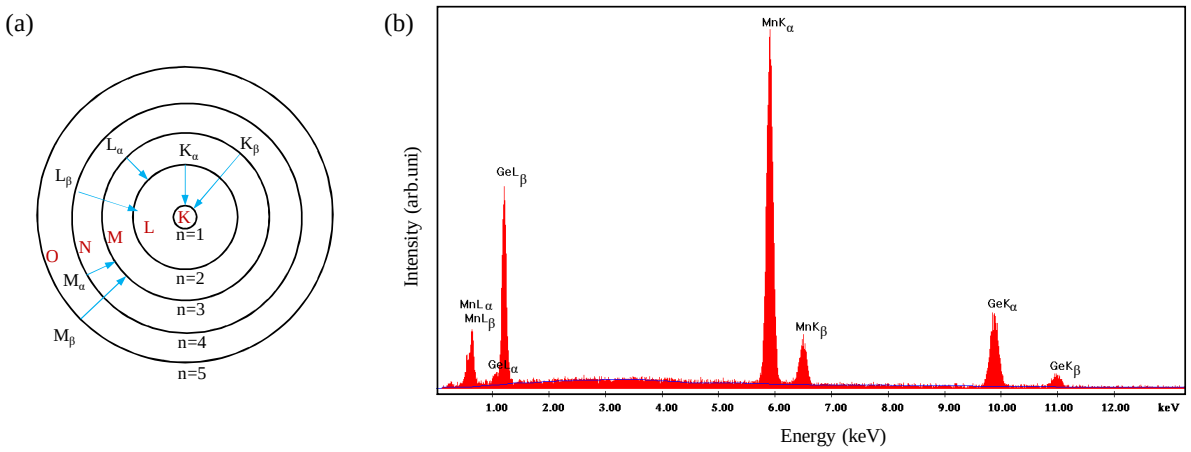

Figure 2.2: Schematic diagram of electron transitions to lower atomic levels and generation of K, L, and M lines. A typical EDS spectrum showing the characteristic X-ray lines from different elements present in the sample.

When a sample is bombarded with a high kinetic energy electron beam, the bound electrons from the inner shells of the atoms are knocked off. Now that there is a vacancy in the inner shell, the electrons in the outer shell jump down to the lower energy inner shells. In this process, the electron generates an X-ray with energy equal to the difference between the two energy levels. The energy levels are defined by principal quantum number n. n=1, 2, 3, and 4 are denoted by K, L, M, and N, respectively. Fig. 2.2(a) exhibits schematic diagram demonstrating the generation of different characteristic X-rays. When the electron falls down from L to K shell, the characteristic X-ray is named K_α. For M to

K shell jump, the generated X-ray is denoted as K_β. Similarly, L_α, L_β X-rays are generated due to electron transition from M and N shells to L respectively. Since each element in the periodic table has a different atomic structure, one can determine the elements present in a sample by detecting the characteristic X-rays coming out of the sample.

Fig. 2.2(b) shows a typical EDS image showing the characteristic X-ray peaks K_α, K_β, and L_α, L_β of different elements present in the sample (In this case Mn and Ge). Here, the intensity of a particular X-ray peak is dependent on the probability of a particular electron transition. The probability of L to K shell electron transition is higher than M to K shell transition. As a result, K_α peaks have a higher intensity than K_β peaks for both Mn and Ge. For quantitative analysis, first, the background (the black line in Fig. 2.2(b) EDS spectra) intensity is subtracted from the obtained spectrum. The relative intensity of the peaks from different elements gives the weight percentage. The atomic percentage is further calculated by considering the atomic weight of each element.

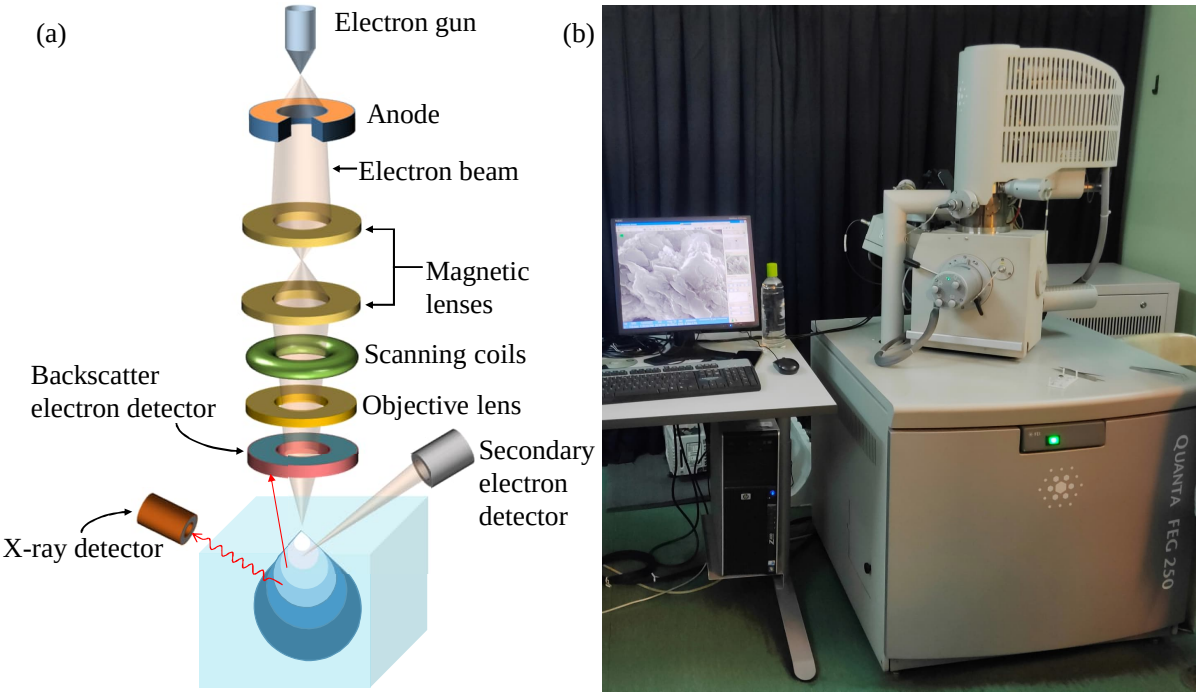

Figure 2.3: (a) Schematic diagram of different parts of a scanning electron microscope (SEM). (b) EDS attached to FE-SEM used for our sample characterization at SNBNCBS.

Experimental Set up

The image of the entire setup used for performing EDS measurements is given in Fig. 2.3(b). This is a Field emission scanning electron microscope (FESEM), a type of SEM that uses a Field emission gun instead of thermionic excitation to generate an electron beam. Here the field emission gun uses a potential gradient for generating an electron beam with a much smaller spot size. As a result, this FESEM setup has better than 1.5 nm resolution and can be used for observing the surface morphology on the nanometer scale. The schematic diagram of an SEM is presented in Fig. 2.3(a). EDS is one component of this setup. For collecting the EDS spectrum, an electron beam of 20-25 kV is focussed on the sample in 1 mbar vacuum. Then a Silicon drift detector is used for detecting the characteristic X-rays coming out from different elements of the sample. Then from the counts of each X-ray line, the percentage of each element present in the sample is acquired.

2.3 Structural characterization

2.3.1 X-ray diffraction (XRD)

X-ray diffraction technique is used to identify the crystal structure and symmetry of the as-prepared materials. In general, the atoms in crystals arrange themselves in a periodic pattern constructing the crystal lattice. In this technique, an X-ray beam of a particular wavelength λ is focussed on the lattice planes of a crystal at an angle θ (Fig. 2.4(a)). The electrons of the atoms then scatter the beam elastically at the same angle. Since the X-ray beam is diffracted by different lattice planes, depending on their path difference, there can be either constructive or destructive interference. If d is the distance between two consecutive lattice planes, the path difference between the X-rays diffracted from the two consecutive lattice planes will be $2dSin(\theta)$. Constructive interference will only appear when this path difference equals $n\lambda$ (n is an integer number), which brings us to the Bragg's law $2dSin(\theta)=n\lambda$ [98]. Collecting the diffracted X-ray as a function of θ, one can find intensity peaks at certain θ values signifying constructive interference. By calculating the lattice plane distance (d) using the Bragg's relation, we can estimate the lattice constant and symmetry of the crystal.

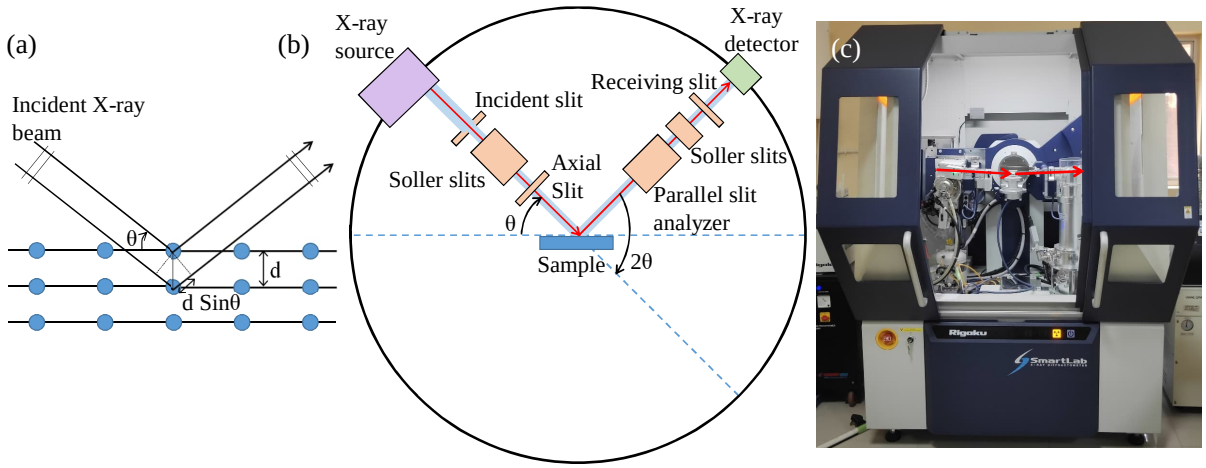

Figure 2.4: (a) X-ray diffraction from the lattice planes. (b) Schematic diagram of an X-ray diffractometer. (c) Rigaku SmartLab X-ray diffractometer used for our measurements at SNBNCBS.

A schematic diagram of a typical XRD setup is shown in Fig. 2.4(b). To generate X-rays, first, an electron beam is generated inside a highly evacuated X-ray tube via thermionic emission from a heated W-cathode, which is then targeted on the Cu anode to produce characteristic X-rays. The generated characteristic X-ray is then passed through different slits to obtain a focussed X-ray beam that incidents on the sample surface. The diffracted X-ray beam is again passed through slits like Parallel slit analyzer, Soller slit, and receiving slit to focus the beam and increase the peak intensity of the collected XRD data [99]. We carried out XRD measurements in Rigaku SmartLab X-ray diffractometer (9 kW) using Cu-Kα radiation (λ=1.54Å) (Fig.2.4(c)). Here the electrons emitted from W-cathode are accelerated with a voltage difference of 20-45 KV between the cathode and anode, and the electron current is kept within 10-200 mA. As a result, an electron beam of a maximum of 9 KW is generated, which hits the Cu anode to generate Cu Kα X-rays. To detect the diffracted beam, hybrid photon counting (HPC) detector is used [100]. It is worthy to mention that the above mentioned diffractometer uses $\theta - \theta$ goniometer. Here the sample stage remains fixed while the X-ray tube and detector rotate to collect the XRD pattern. The angular position of the X-ray tube and detector are recorded as -θ and θ. There are other XRD setups such as Rigaku MiniFlex II with $\theta - 2\theta$ goniometer, where instead of the X-ray tube, the sample stage rotates at an angle θ and the detector by 2θ.

2.3.2 Low-energy electron diffraction (LEED)

LEED technique is used for visualizing the crystal symmetry of the single crystal surface. Here a focussed low-energy electron beam (the red arrow in Fig. 2.5(a)) falls on the freshly cleaved surface of the single crystal. The crystal lattice then diffracts the electron beam in different directions, and based on the crystal structure of the specimen, we observe a diffraction pattern on our hemispherical fluorescent screen.

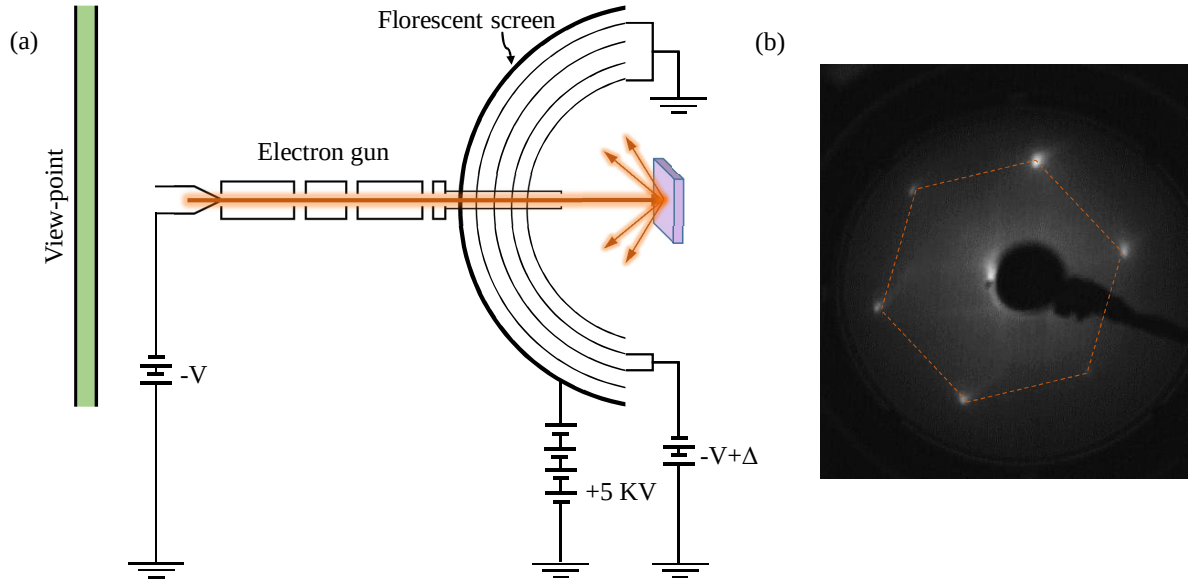

Figure 2.5: (a) Schematic diagram of a LEED setup. (b) LEED data of a single crystal with hexagonal symmetry.

The schematic diagram of a LEED setup is illustrated in Fig. 2.5(a). The electron beam is generated from the cathode filament by thermionic emission. To generate the required low-energy electron beam, the emitted electrons are accelerated by keeping the cathode at a negative potential -V (usually within 30-200 eV) w.r.t. the sample surface. The accelerated electron beam is then collimated with electron lenses and bombarded on the sample surface. Since this technique is highly surface sensitive, the single crystal needs to be cleaved *in-situ* before measurement. The scattered electrons then fall on the hemispherical grids that block all the secondary electrons with lower energy from reaching the fluorescent screen. Here a negative voltage is used to stop the low-energy electrons. Therefore, only elastically scattered electrons that create the diffraction pattern reach the screen. The screen is kept at a higher positive voltage ($\sim$+5 KV) to accelerate

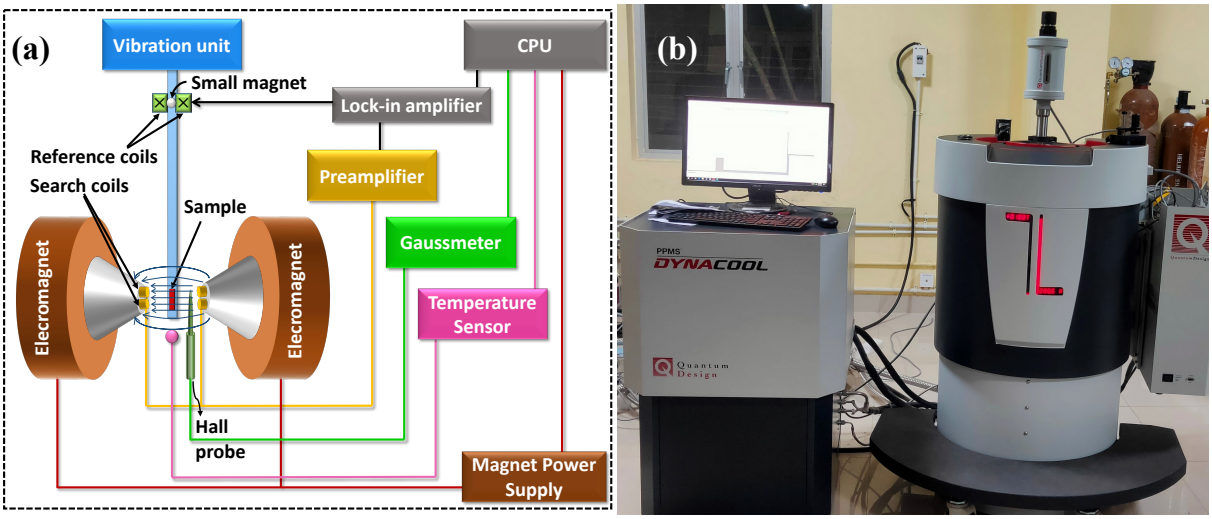

Figure 2.6: (a) Schematic diagram of a VSM setup. (b) VSM option with the Quantum Design PPMS.

the electrons enough to excite the fluorescence. So we observe bright spots creating a diffraction pattern as shown in Fig. 2.5(b).

2.4 Vibrating sample magnetometer (VSM) measurements

VSM is a widely used scientific apparatus that employs Faraday's law of induction [101] to measure the magnetic properties of materials. According to Faraday's law, electromotive force (emf) is generated in a conducting coil when kept under a varying magnetic field. If the applied magnetic flux passing through the coil is Φ_B, then emf (ϵ) generated in the coil will be $\epsilon = -\frac{d\Phi_B}{dt}$. $\frac{d\Phi_B}{dt}$ is the rate at which the magnetic flux changes with time. The direction of current flow from the induced emf ϵ is determined by Lenz's law. Hence, the induced current direction is such that it generates a magnetic field opposite to the varying applied magnetic field passing through the coil.

Different components of a VSM setup are demonstrated in Fig. 2.6. The magnetic sample is mounted on a non-magnetic stick which is connected to the vibration unit of the setup. The stick is then positioned to keep the sample between two electromagnet poles where the field is uniform. The external magnetic field somewhat aligns the magnetization along the field. Then, as the sample is moved up and down at high speed, the magnetic field

created by the magnetic dipole moment of the sample changes with time. This alternating magnetic field from the sample induces an electric field in the pickup coils of the setup by the Faraday's law of induction. The voltage generated in the pickup coil $V_{coil} = \frac{d\Phi_B}{dt}$. In terms of the vertical position of the sample (z), $\frac{d\Phi_B}{dt}$ can also be written as $\frac{d\Phi_B}{dz}\frac{dz}{dt}$. So, for a sample oscillating sinusoidally at a frequency f and amplitude A, the induced voltage will be $V_{coil} = 2\pi f C m A Sin(2\pi f t)$. Here C is the coupling constant, and m is the sample's magnetic moment we intend to measure. Thus, from the coil voltage, we can extract the sample magnetization at an applied magnetic field.

All magnetization measurements were carried out using the VSM option in the Quantum Design PPMS with magnetic fields varied up to 9 T within the temperature range of 2 and 300 K 2 K to 300 K. During the measurements, the sample is oscillated with a frequency $f = 40$ Hz and amplitude A=1-3 mm with VSM linear motor, which generates a voltage in the pickup coils. This setup is capable of detecting very low magnetic moments up to the order of 10^{-6} emu. Furthermore, using the VSM oven option in this PPMS, one can perform VSM measurements at high temperatures (400-1000 K).

2.5 Electrical resistivity measurements

To understand the electrical transport properties of the as-grown single crystals, we performed resistivity measurements. By observing the temperature-dependent resistivity data, we can identify the nature of the samples, such as metallic, insulating, superconducting, or semiconducting. In this thesis, all of the discussed topological materials are found to be good conductors with resistance in the order of $m\Omega$. Hence we performed resistivity measurements in the four-probe technique. In this method, four probes are made on the sample, among which two are used for current flow and the other two for measuring voltage drop across the sample. This way, the contact resistance gets canceled, making this technique very efficient for low resistivity measurements. A typical four-probe resistivity set-up is demonstrated in Fig. 2.7(a). The lock-in amplifier works as an AC voltage source that causes current flow through the sample and the standard resistance (R_L). Since the sample resistance is very low, R_L is added to the circuit to reduce the voltage drop across the sample and prevent its burning from joule heating. If the voltage drop measured across the sample is considered V_S, and the voltage drop across R_L is V_L, then sample resistance (R_S) can be written as $R_S = \frac{R_L}{V_L} \times V_S$ when R_S and R_L are con-

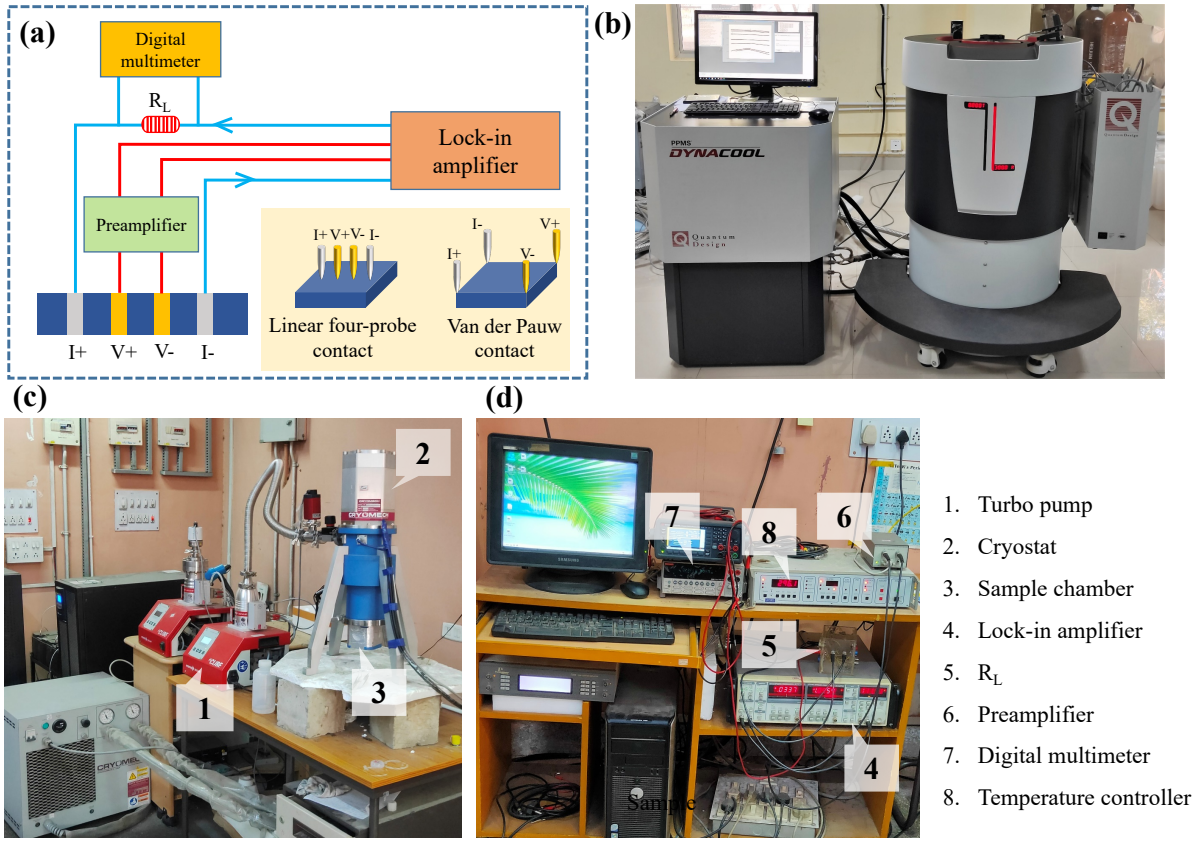

Figure 2.7: (a) Schematic diagram of a four-probe resistivity measurement setup. Inset shows linear and Van der Pauw connections for four-probe measurements. (b) Photographic image of PPMS available at SNBNCBS, used to measure resistivity of our single crystals in the presence of different temperatures and fields. (c)-(d) In-house resistivity set-up for temperature-dependent resistivity. The name of the components numbered in the white bubbles is presented on the right.

nected in series. Hence, we can extract the sample resistance by measuring V_S, V_L, and R_L. During the measurements, there are two different types of four-probe contacts made on a sample surface: (a) linear four-probe connection and (b) Van der Pauw connection. The schematics of these two methods are shown in the inset of Fig. 2.7(a). In the linear four-probe technique, four equispaced probes are connected on the sample with two outer probes for current flow and two inner probes for voltage measurements (Left image in the inset), while all probes are placed across the edge of the sample in Van der Pauw method (right image in the inset)[102]. As a result, we obtain the average resistivity of the whole sample in the Van der Pauw method instead of resistivity along the connection direction, which is the case for the linear four-probe technique. These two methods are alternatively used for different shapes of the sample. While the linear four-probe technique is more

efficient for needle-shaped samples, the Van de Pauw method can be used for measuring the resistivity of square-shaped samples.

Temperature-dependent resistivity measurements within 4 to 300 K were carried out in our in-house resistivity setup (Fig.2.7(c)-(d)). Quantum Design PPMS (Fig.2.7(b)) with ETO option was used for performing both temperature and field-dependent resistivity measurements with the magnetic field varied up to 9 T, and the temperature changed within the range of 2 and 300 K. Cu wires were used for preparing the four-probe connection. Vacuum-compatible Epo-Tek H2OE silver epoxy was used for connecting the Cu wires to the samples. A high-resolution microscope (Leica S9i) is used to attach the four-probe contacts on the sub-millimeter-sized samples for these studies. Then to perform resistivity measurements in the in-house setup, the sample was mounted on the sample stage of the cryostat, and an AC voltage within 1-5 V and frequency 111.11 Hz was applied on the sample, and a standard resistance R_L (usually within 1-2 KΩ) using Stanford Research Systems 830 (SR830) digital signal processing (DSP) lock-in amplifier. Keithly 2000 digital multimeter (DMM) was used to determine the voltage drop V_L across R_L. To measure V_S, the two voltage leads $V+$ and $V-$ are first connected to SR554 transformer preamplifier that amplifies the voltage by 100, then connected again to the lock-in amplifier. CRYOMECH closed cycle refrigerator(CCR) based cryostat was used for cooling down the sample to the lowest achievable temperature 4 K. Oxford Instrument^{TM} ITC-503 temperature controller was used to control the rate of temperature change during measurements, and the sample temperature was detected using an Rh-Fe thermometer connected to the sample stage. Next, to control the whole measurement from the desktop, different components of the setup were connected to the desktop with General Purpose Interface Bus (GPIB), and then a LabVIEW program was used for the data acquisition.
.

2.6 Photoemission spectroscopy

When a photon beam of energy $h\nu$ incidents on a solid, the electrons from different atomic orbitals of the solid absorb the photon energy and emit out of the solid (Fig. 2.8(a)). If the kinetic energy of the emitted electron is E_{kin}, then $E_{kin} = h\nu - E_B - \Phi$, where E_B is the binding energy of the electron inside the solid and Φ is minimum energy for taking an electron out of the sample to the vacuum, also known as work function. The

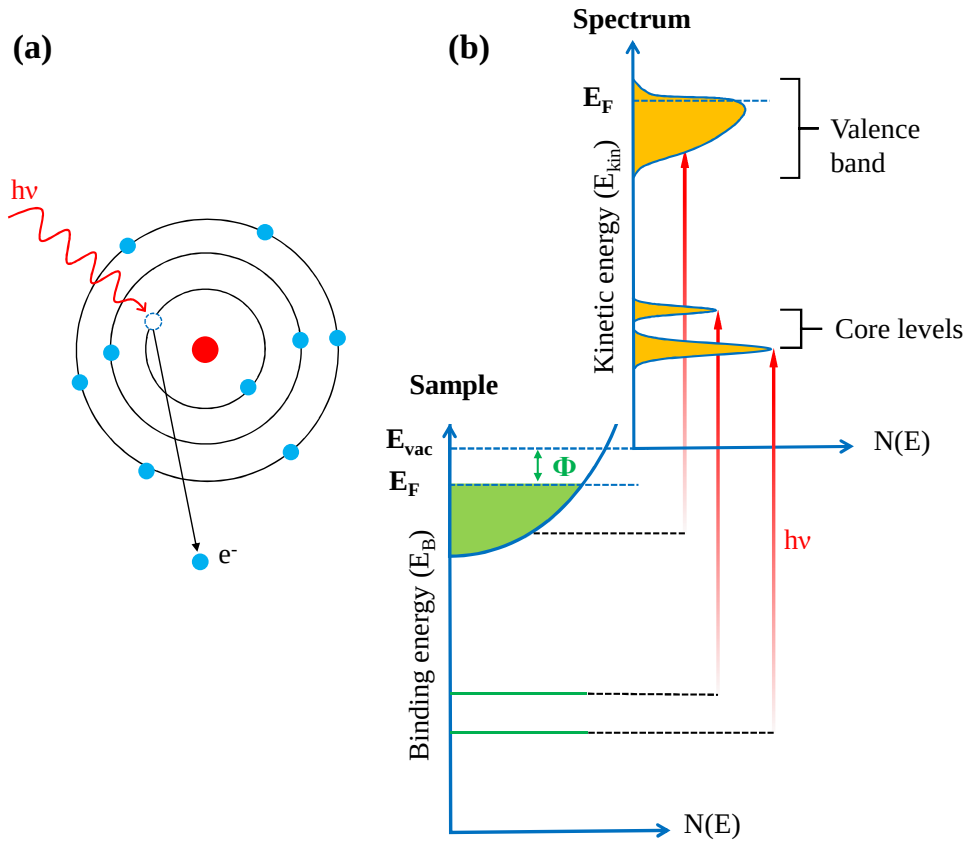

Figure 2.8: (a) Emission of a photoelectron from an atom. (b) The bottom left diagram is the Binding energy (E_B) as a function of the DOS inside a sample. After the incidence of a photon beam with energy hν, the kinetic energy (E_{kin}) distribution of the detected photoelectrons is presented in the top right diagram.

history of photoemission goes back to the late 19th century: in the year 1887, Heinrich Hertz had noticed the electron emission from a solid when light impinges on it. Later this process was successfully explained by Albert Einstein in the year 1905 and is known as the photoelectric effect. Photoemission spectroscopy (PES) is a measurement technique that utilizes the photoelectric effect to determine the binding energy of electrons (E_B) inside the sample. Fig. 2.8(b) shows the binding energy distribution of electrons inside the sample and the representation of the obtained kinetic energy distribution of the photoelectrons ejected from the sample surface when collide with a photon beam of energy $h\nu$. Among different PES techniques, we used XPS and ARPES to study both the bulk and surface electronic structure of our samples. Depending on the incident photon energy, one can extract either bulk or the surface electronic structure. The dependence of the inelastic mean free path (also known as escape depth) of the photoelectrons (λ) to its kinetic energy

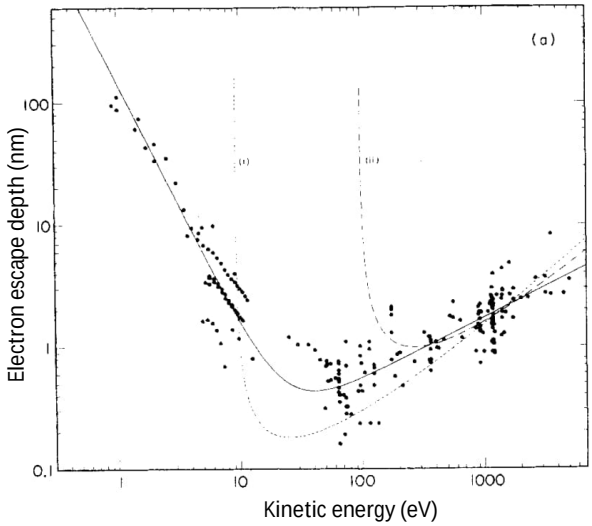

Figure 2.9: Inelastic mean free path (electron escape depth) of photoelectron plotted as a function of its kinetic energy. The figure is taken from ref.[12]

is presented by the *universal curve* [12] in Fig. 2.9. The curve can be fitted by

$$\lambda = \frac{A}{E^2} + B\sqrt{E} \tag{2.1}$$

with $E < 10eV$ region having more contribution from $\frac{A}{E^2}$ and $E > 60eV$ region from $B\sqrt{E}$. The escape depth is at its lowest within 10-100 eV kinetic energy of electrons, which means when a sample surface is hit with 10-100 eV photon beam, the photoelectrons mostly come out from the sample surface, providing the surface electronic structure. On the other hand, photoelectrons excited by photons outside this energy range have higher escape depth, carrying information about the bulk bands.

Theory of PES

Theoretically, PES can be described using Fermi's Golden rule [103]. In the photoelectric process, if the initial state wave function is $\Psi_i(N)$ and the final state wave function is $\Psi_f(N)$ for an N-electron system, the probability of transition (w_{fi}) from $\Psi_i(N)$ to $\Psi_f(N)$ will be

$$W_{fi} \propto \frac{2\pi}{\hbar} |\langle \Psi_f | H_{int} | \Psi_i \rangle|^2 \delta(E_f(N) - E_i(N) - h\nu) \tag{2.2}$$

$E_i(N)$ and $E_f(N)$ represent the energy of the system in its initial and final state, and H_{int} is the perturbation operator for the interacting electron. For an unperturbed system, $H = \frac{p^2}{2m_e} - eV(\mathbf{r})$. When the momentum $\boldsymbol{p}$ transforms to $\boldsymbol{p} - \frac{e}{c}\boldsymbol{A}$, the Hamiltonian will be

$$H = \frac{1}{2m_e}\left(\mathbf{p} - \frac{e\mathbf{A}}{c}\right)^2 + eV(\mathbf{r}) = \left[\frac{p^2}{2m_e} + eV(\mathbf{r})\right] + \left[\frac{e}{2m_e c}(\mathbf{A}.\mathbf{p} + \mathbf{p}.\mathbf{A}) + \frac{e^2A^2}{2m_e c^2}\right] \quad (2.3)$$

The second part of H corresponds to H_{int}. Since the momentum operator $\mathbf{p} = -i\hbar\nabla$, the commutation of $\mathbf{p}$ and $\mathbf{A}$ will be $[\mathbf{p}.\mathbf{A}] = -i\hbar\nabla.\mathbf{A}$. Under the approximation that the wavelength of the incident photon is much larger compared to the electron escape depth (dipole approximation), $-i\hbar\nabla.\mathbf{A} = 0$. Then the perturbation Hamiltonian becomes

$$H_{int} = \frac{e}{m_e c}(\mathbf{A}.\mathbf{p}). \quad (2.4)$$

The term $\frac{e^2A^2}{2m_e c^2}$ in Eqn. 2.3 is disregarded here as it is only relevant for a very high-intensity photon beam, which is not the case for a typical laboratory source. Based on Eqn. 2.4 the transition probability will be,

$$W_{fi} \propto |\langle\Psi_f|(\mathbf{A}.\mathbf{p})|\Psi_i\rangle|^2 \delta(E_f(N) - E_i(N) - h\nu) \quad (2.5)$$

So far, there are two models used to describe the transition probability W_{fi}: (a) three-step model and (b) one-step model [104]. Visual representations of these two models are provided in Fig. 2.10. According to the three-step model (Fig. 2.10(a)), the transition from the initial to the final state occurs in three steps:

1. Photoexcitation of a bound electron inside the solid
2. Advancement of the excited electron towards the solid surface.
3. Emission of the electron from the surface to the vacuum.

On the contrary, the one-step model considers the whole procedure from photoexcitation to emission to be in a single step (Fig. 2.10(b)) and makes quite a complex mathematical representation. As a result, the three-step model is usually preferred over the one-step model for describing most of the experimental observations. Following the three-step

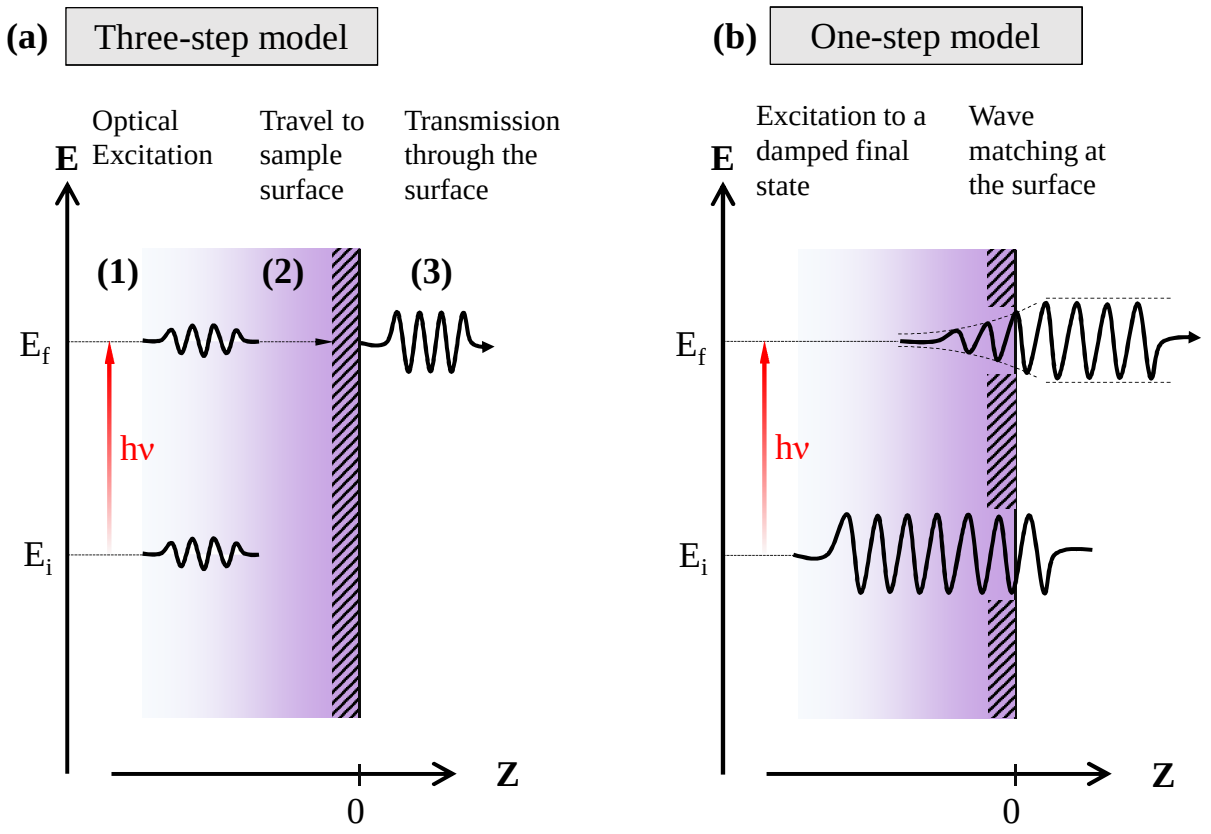

Figure 2.10: Representations of (a) three-step model and (b) one-step model.

model, it appears that separating the wave function of the photoelectron from the rest of the solid make things simpler. Hence, the initial state $\Psi_i(N)$ can be written in terms of one electron wave function $\phi_i(\mathbf{k})$ (here $\mathbf{k}$ is the momentum vector) and wave function of the remaining $(N-1)$ electrons $\Psi_i(N-1)$ as,

$$\Psi_i(N) = C\phi_i(\mathbf{k})\Psi_i(N-1). \tag{2.6}$$

The final state wave function $\Psi_f(N)$ of the photoelectric effect can also be written as

$$\Psi_f(N) = C\phi_f(\mathbf{k})\Psi_f(N-1) \tag{2.7}$$

under the *sudden approximation*, which separates the photoelectron wave function $\phi_f(\mathbf{k})$ from the wave function of the remaining system $\Psi_f(N-1)$ of (N-1) electrons, while neglecting all other interactions such as electron-electron and electron-phonon interactions between the photoelectron and the system.

Therefore, $\langle \Psi_f | H_{int} | \Psi_i \rangle$ term in Eqn. 2.2 can be written as,

$$\langle \Psi_f | H_{int} | \Psi_i \rangle = \langle \phi_f(\mathbf{k}) | H_{int} | \phi_i(\mathbf{k}) \rangle \langle \Psi_f(N-1) | | \Psi_i(N-1) \rangle \tag{2.8}$$

$\langle \phi_f(\mathbf{k}) | H_{int} | \phi_i(\mathbf{k}) \rangle$ is the matrix element M_{fi} for one electron dipole in presence of light. This way, the intensity of photoelectrons momentum $\mathbf{k}$ will be proportional to W_{fi} and can be written as,

$$I(h\nu, \mathbf{k}, E) \propto \sum_{f,i} |M_{fi}|^2 T(E, \mathbf{k}) D(E_{kin}, \lambda) \delta(E_f - E_i - h\nu) \tag{2.9}$$

$T(E, \mathbf{k})$ is the escape probability of the electrons and $D(E, \lambda)$ transport depth of the electrons, which in terms of inelastic mean free path λ can be written as

$$D(E, \lambda) \approx \frac{\alpha\lambda}{1 + \alpha\lambda} \tag{2.10}$$

Here α is the optical absorption coefficient. The expression for photocurrent I in Eqn. 2.9 is valid for atoms and molecules. When considered for a solid $\delta(E_f - E_i - h\nu)$ will be replaced by spectral function $A(E, \mathbf{k})$ giving the photocurrent equation for solid,

$$I(\nu, \mathbf{k}, E) \propto \sum_{f,i} |M_{fi}|^2 T(E, \mathbf{k}) D(E_{kin}, \lambda) A(E, \mathbf{k}) \tag{2.11}$$

The spectral function $A(E, \mathbf{k})$ can be represented in terms of Green's function as:

$$A(E, \mathbf{k}) = -\frac{1}{\pi} Im[G(E, \mathbf{k})] \tag{2.12}$$

The Green's function for an interacting electron system with self-energy $\Sigma(E, \mathbf{k})$ is

$$G(E, \mathbf{k}) = \frac{1}{E - E_k^0 - \Sigma(E, \mathbf{k})} \tag{2.13}$$

Here, the self energy $\Sigma(E, \mathbf{k})$ is a complex quantity, $\Sigma(E, \mathbf{k}) = Re\Sigma(E, \mathbf{k}) + iIm\Sigma(E, \mathbf{k})$ and the corresponding spectral function in terms of $\Sigma(E, \mathbf{k})$ will be

$$A(E, \mathbf{k}) = -\frac{1}{\pi} \frac{Im\Sigma(E, \mathbf{k})}{\left[E - E_k^0 - Re\Sigma(E, \mathbf{k})\right]^2 + \left[Im\Sigma(E, \mathbf{k})\right]^2} \tag{2.14}$$

E_k^0 is the bare band energy. The spectral function above is a Lorentzian function with a

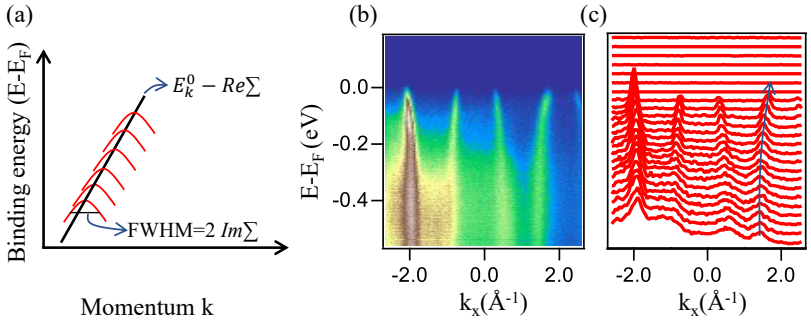

Figure 2.11: (a) A schematic diagram showing the extraction of self-energy information from ARPES data. (b) and (c) demonstrate an example of ARPES data and the MDCs extracted from the data.

half-width half maxima of $Im\Sigma(E, \mathbf{k})$ and peak position at $E_k^0 - Re\Sigma(E, \mathbf{k})$. Angle resolve photoemission spectroscopy (ARPES) measurements provide direct access to observe the spectral function $A(E, \mathbf{k})$ following Eqn. 2.11. Fig. 2.11(a) Schematically shows the extraction of real and imaginary parts of the self-energy from a given band dispersion. Fig. 2.11(b) demonstrates an E vs. k diagram obtained from ARPES measurements. Fig. 2.11(c) shows the MDCs extracted at different binding energies. From Fig. 2.11(c) one can easily visualize the Lorentzian pattern of the peaks, which are quite comparable to the schematics in Fig. 2.11(a).

The self-energy of an electron system has main contributions from electron-electron (Σ^{el-el}), electron-phonon (Σ^{el-ph}), and electron-impurity (Σ^{el-imp}) interactions :

$$\Sigma = \Sigma^{el-el} + \Sigma^{el-ph} + \Sigma^{el-imp} \tag{2.15}$$

Among these, Σ^{el-el} affects the electrons at higher binding energies, and Σ^{el-ph} dominates over the electrons near the Fermi level. Σ^{el-el} can be expressed as [105]:

$$\Sigma^{el-el} = \alpha E + i\beta[E^2 + (\pi k_B T)^2] \tag{2.16}$$

and Σ^{el-ph} can be expressed as [105, 106]:

$$\Sigma^{el-ph} = \int dE' \int_0^{\hbar\omega_D} \alpha^2 F(\hbar\omega) \left[\frac{1 - f(E', T) + n(\hbar\omega, T)}{E - E' - \hbar\omega} + \frac{f(E', T) + n(\hbar\omega, T)}{E - E' - \hbar\omega} \right] d(\hbar\omega) \tag{2.17}$$

The β in Eqn. 2.16 represents the strength of e-e coupling. In Eqn. 2.17, $\hbar\omega_D$ stands for Debye energy. The term $n(\hbar\omega, T)$ and $f(E', T)$ represent Bose-Einstein and Fermi-Dirac distributions, respectively. $\alpha^2 F(\hbar\omega)$ is the electron-phonon coupling term, which is also known as the Eliashberg spectral function. $F(\hbar\omega)$ in $\alpha^2 F(\hbar\omega)$ stands for the phonon DOS. From Eqn. 2.17, one can extract the $Im\Sigma^{el-ph}$ [105, 106]:

$$Im\Sigma^{el-ph} = \pi \int_0^{\hbar\omega_D} dE' \alpha^2 F(E') \left[1 + 2n(E') + f(E + E') - f(E - E')\right] \tag{2.18}$$

Here, we would like to introduce another important parameter called the electron-phonon coupling strength λ_{el-ph}. In terms of self energy, $\lambda_{el-ph} = \left.\frac{\partial \Sigma^{el-ph}}{\partial E}\right|_{E_F}$. λ_{el-ph} is also known as the mass enhancement factor and can be expressed in terms of the group velocity near Fermi level v_F. If we consider the bare band velocity of electrons without any correlations as v_b, then $\lambda_{el-ph} = \frac{v_b}{v_F} - 1$.

2.6.1 XPS measurements

XPS is a PES technique that uses photoelectric effect to collect information about the elements present in both surface and bulk of the sample and their corresponding oxidation states. The schematic diagram showing different components of an XPS setup is presented in Fig. 2.12. As suggested by the name, XPS uses X-ray sources such as Al Kα, Mg Kα, or synchrotron radiation source to hit the sample surface, which results in the emission of photoelectrons in different directions. These photoelectrons have an average inelastic mean free path of a few nms(1-10 nm). Hence, one needs to cleave the sample $in - situ$ before irradiating the X-ray beam on the sample surface. A small portion of the emitted electrons is then passed through the electrostatic lenses depending on the acceptance angle and focussed on the hemispherical analyzer, which separates the electrons based on their kinetic energy. As illustrated in Fig. 2.12, a hemispherical analyzer consists of two concentric hemispheres of different radii, where the outer hemisphere is kept at a negative voltage w.r.t the inner hemisphere. As soon as the focussed beam with different kinetic

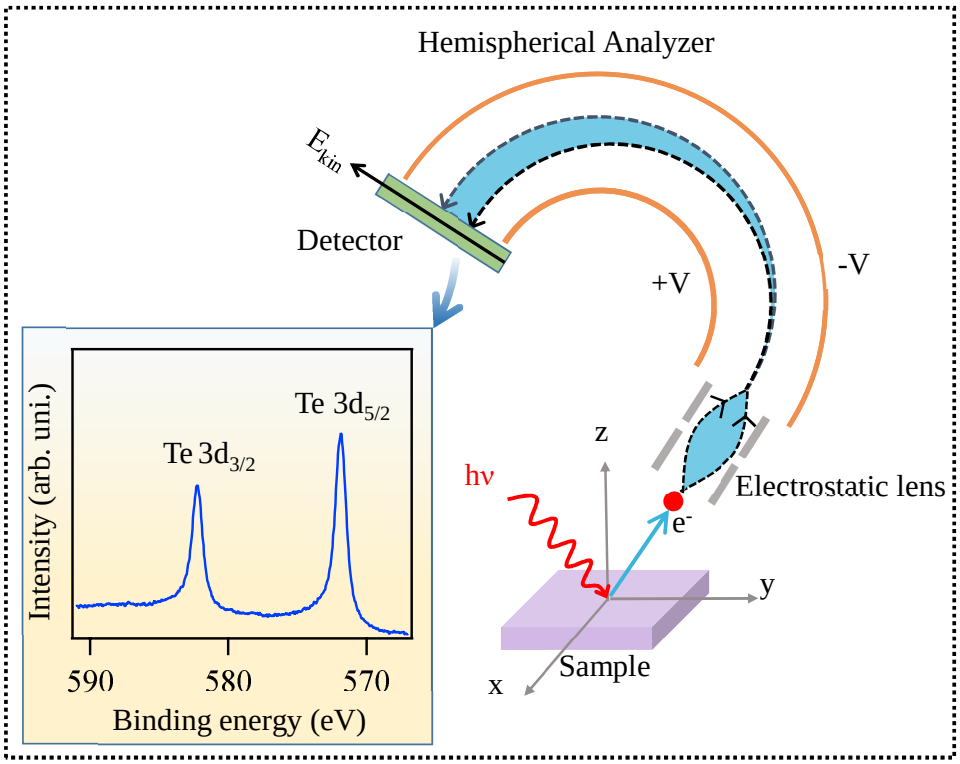

Figure 2.12: Schematic diagram of an XPS setup

energy electrons enters the analyzer, the voltage difference deflects the electrons into different trajectories depending on their kinetic energies. While the electrons with higher kinetic energy are deflected towards the outer hemisphere, the lower energy electrons follow trajectories closer to the inner hemisphere. The detector collects the photoelectrons of different kinetic energy to generate the XPS spectra as a function of energy. Moreover, by changing the voltage of the hemispheres (pass energy), one can tune the kinetic energy window of electrons that will reach the detector. An example of XPS data showing Te 3d peaks is presented in Fig. 2.12. We obtained the binding energy E_B from the photoelectric effect formula that says, $E_B = h\nu - E_{kin} - \Phi$. Since each element of the periodic table has very distinctive energy levels, we can determine the elements present in a sample and their oxidation states from the binding energy values of the intensity peaks. Additionally, we can determine the atomic percentage of each element from the area under their corresponding intensity peaks. We performed XPS measurements using a synchrotron source in BL-10 at RRCAT Indore. All samples were cleaved $in-situ$ in the vacuum better than 5×10^{-11} mbar. XPS measurements were carried out at a sample temperature of 20 K using SPECS Phoibos150 electron analyzer with a photon energy of

hν= 800 eV and an energy resolution of 0.4 eV.

2.6.2 ARPES measurements

Similar to XPS, ARPES is also a PES technique that works on the photoelectric effect. In the case of ARPES measurement, the angle of the incident photon beam is varied, and along with the information of kinetic energy and electron counts, the angle of the emitted electrons θ is also recorded by the hemispherical analyzer. So, one can obtain three-dimensional data with electron counts at different kinetic energy and θ (Fig. 2.14(c)). This additional information of θ corresponds to the momentum vector k. The schematic diagram in Figs. 2.14(a)-(b) describes the measurement geometry of ARPES. If we consider a photoelectron with momentum vector k is emitted at a polar angle θ and azimuthal angle ϕ (Fig. 2.14(a)), the three components of the momentum vector will be:

$$k_x = k \sin\theta \cos\phi \tag{2.19}$$

$$k_y = k \sin\theta \sin\phi \tag{2.20}$$

$$k_z = k \cos\theta \tag{2.21}$$

Figure 2.13: XPS/ARPES set-up at RRCAT, Indore (taken from ref. [13]).

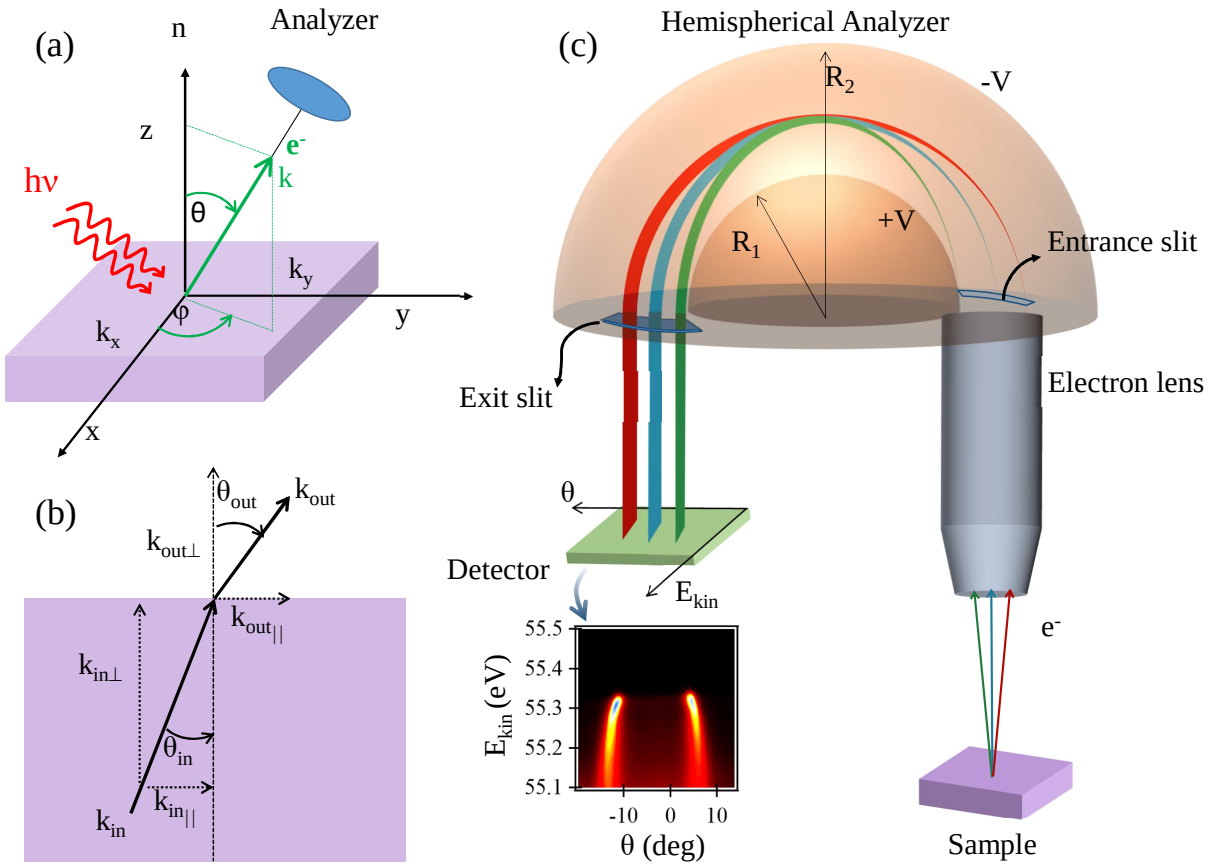

Figure 2.14: (a) Geometrical description of an ARPES measurement. (b) Transmission of in-plane ($k_{||}$) and out-of-plane ($k_{\perp}$) momentum vectors from the sample to vacuum. (c) Schematic diagram of a hemispherical analyzer showing how the electrons with different angles and kinetic energy follow separate paths inside the analyzer to create a kinetic energy and theta-dependent intensity (electron counts) map.

The k_x and k_y are the components parallel to the sample surface. Hence, the momentum component parallel to the sample surface is $k_{||} = \sqrt{k_x^2 + k_y^2} = k \sin\theta$, and k_z is the vector component perpendicular to the sample plane also expressed as $k_{\perp}$. The transmission geometry of the momentum vector from inside the sample to the vacuum is sketched in Fig.2.14(b). Here k_{in} and θ_{in} define the momentum vector and emission angle inside the sample, while k_{out} and θ_{out} represent the same in a vacuum.

Following the energy conservation law E_{kin} can be written as:

$$E_{kin} = \frac{\hbar^2 k_{in}^2}{2m} - V_0 = \frac{\hbar^2 k_{in||}^2}{2m} + \frac{\hbar^2 k_{in\perp}^2}{2m} - V_0 \tag{2.22}$$

Here, V_0 is the inner potential term which stands for the energy difference between the valence band minima and the vacuum (E_{vac} in Fig.2.8(b)). The value of V_0 differs for every element and can be obtained from the scans along k_z direction or theoretical calculations.

In terms of k_{out}, E_{kin} will be,

$$E_{kin} = \frac{\hbar^2 k_{out}^2}{2m} = \frac{\hbar^2 k_{out||}^2}{2m} + \frac{\hbar^2 k_{out\perp}^2}{2m} \tag{2.23}$$

According to the three-step model, when an electron passes through the sample surface to the vacuum, the momentum conservation law is preserved along the in-plane direction and broken along the out-of-plane direction. If $k_{in||} = k_{out||}$, then

$$\frac{\hbar^2 k_{out||}^2}{2m} = \frac{\hbar^2 k_{in||}^2}{2m} \tag{2.24}$$

and

$$\frac{\hbar^2 k_{out\perp}^2}{2m} = \frac{\hbar^2 k_{in\perp}^2}{2m} - V_0 \tag{2.25}$$

Since $k_{out||} = k_{out} \sin\theta_{out}$,

$$k_{in||} = k_{out||} = \sqrt{\frac{2mE_{kin}}{\hbar^2}} \sin\theta_{out} \tag{2.26}$$

However, from Eqns. 2.21 and 2.25, $k_{in\perp}$ component in terms of E_{kin} and θ_{out} will be,

$$k_{in\perp} = \sqrt{\frac{2mE_{kin}\cos^2\theta + V_0}{\hbar^2}} \tag{2.27}$$

This way, one can obtain the E_B vs. k diagram by recording the E_{kin} and θ_{out} of the emitted electrons.

The samples were cleaved *in-situ* to obtain fresh surface at 5×10^{-11} mbar chamber pressure to perform ARPES measurements on the prepared single crystals. He-I (21.2 eV), He-II (40.8 eV) light source, and synchrotron source (∼20-140 eV) were used as photon source. Since the electron escape depth for the aforementioned photon energy range is lower than 10Å, we mainly obtain information on the surface electronic structure. Throughout the measurement, the sample temperature was kept within 10-300 K. Data were collected with energy resolution between 10-25 meV depending on the photon energy and 0.2^o angular resolution.s We carried out ARPES experiments at different synchrotron

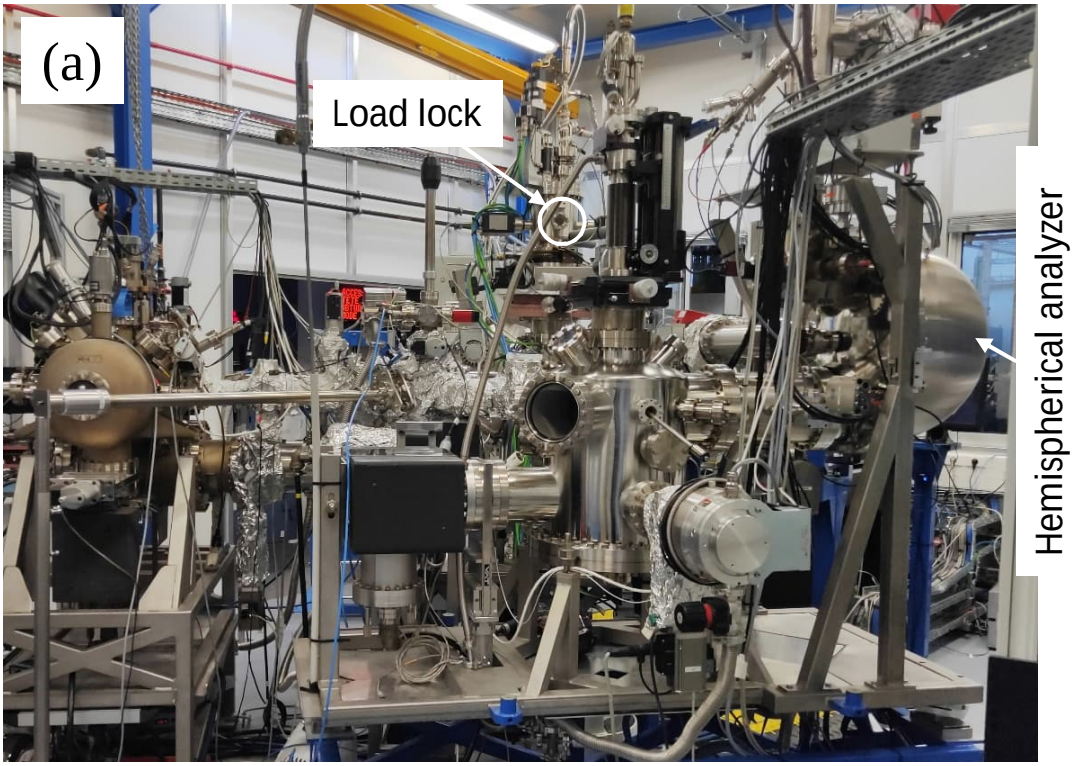

Figure 2.15: (a) ARPES set up at CASSIOPÉE beamline in SOLEIL synchrotron facility, France.

radiation facilities: BESSY II (Helmholtz Zentrum Berlin) synchrotron radiation center, Germany; Swiss Light Source (SLS) at the SIS beamline in PSI, Switzerland, CASSIOPÉE beamline at SOLEIL synchrotron, France, and ARPES BL-10 at Indus-2 in RRCAT, India. The photograph of CASSIOPÉE beamline at SOLEIL synchrotron with ARPES and spin-resolved PES end stations is shown in Fig.2.15.

Chapter 3

Electronic structure studies of FeSi: a chiral topological system

Most recent observation of topological Fermi arcs on the surface of manyfold degenerate B20 systems, CoSi and RhSi, have attracted enormous research interests. Although another isostructural system, FeSi, has been predicted to show bulk chiral fermions, it is yet to be clear theoretically and as well experimentally that whether FeSi possesses the topological surface Fermi arcs associated with the exotic chiral fermions in vicinity of the Fermi level. In this contribution, using ARPES and DFT, we present the low-energy electronic structure of FeSi. We further report the surface state calculations to provide insights into the surface band structure of FeSi near the Fermi level. Unlike in CoSi or RhSi, FeSi has no topological Fermi arcs near the Fermi level as confirmed both from ARPES and surface state calculations. Further, the ARPES data show SOC band splitting of 40 meV, which is in good agreement with bulk band structure calculations. We noticed an anomalous temperature dependent resistivity in FeSi which can be understood through the electron-phonon interactions as we find a Debye energy of 80 meV from the ARPES data.

Results Presented in this chapter are published in Phys. Rev. B 101, 235105 (2020)

3.1 Introduction

Since the discovery of linear dispersive Dirac fermions in graphene [107, 108], the condensed matter has become fertile grounds for the investigation of various exotic topological fermions. Especially, the experimental realization of three-dimensional TIs [3] further boosted the field to new heights, from basic sciences [24, 62, 63, 70, 71, 109–127] to more complex technological designs for the futuristic topological quantum computations (TQC) [15, 19, 128–130]. At present, the topological quantum materials are classified by the Weyl fermions [24, 70, 71, 116–125, 131], the Dirac fermions [62, 63, 112–115, 126], and the Majorana fermions [130, 132]. In general, at the BCP, the Weyl fermions have twofold degeneracy and the Dirac fermions have fourfold degeneracy. Recently, a new type of quantum materials have emerged with manyfold degenerate fermions at the BCP [9, 10, 26, 87, 133, 134]. These manyfold degenerate fermions are manifestations of the certain space-group symmetries in presence of the time-reversal invariance [26]. Among them, the chiral systems like the transition-metal mono-silicides MSi (M = Co, Mn, Fe, Rh) have been at the recent intense research focus as under certain conditions, some of these systems (CoSi and RhSi) are predicted to show spin-1/2 Weyl fermions with a topological charge of ± 1 [9, 10, 26, 87, 134–138], spin-1 excitations with a topological charge of ± 2 [86], and spin-3/2 Rarita-Schwinger-Weyl (RSW) fermions with topological charges of ±4 [85]. Moreover, the surface Fermi arcs connecting the manyfold degenerate BCPs are much longer in these systems compared to the other known Weyl and DSMs [58, 64, 121, 139].

Earlier the transition metal monosilicides were extensively studied for their low-energy electronic correlations [140–149]. Specifically, FeSi shows peculiar temperature dependent electronic and magnetic properties [150–155]. Further, FeSi behaves as a semiconductor with an indirect band gap of 50 meV within the temperature range of 100-200 K [147, 154], while is a bad metal [156] outside of this temperature range. Different mechanisms were proposed to explain this strange electronic and magnetic behaviour, (a) electron-phonon interactions [148, 157], (b) spin fluctuations [158, 159], and c) charge excitations [156]. Apart from these interesting physical properties, FeSi is further predicted to show the above-mentioned manyfold degenerate chiral fermions at the high symmetry points with a nonzero Berry phase [160]. Further, a recent transport study on FeSi shows anomalous temperature dependent resistivity which they attribute it to the plausible TSSs [155].

Motivated by the presence of surface Fermi arcs in RhSi and CoSi, we studied the low-

energy electronic structure of isostructural FeSi using angle-resolved photoemission spectroscopy and density functional theory to show that despite FeSi is being chiral topological system, associated surface Fermi arcs connecting the manyfold degenerate bulk BCPs are absent near the Fermi level. These observations are further confirmed by our surface state calculations. The ARPES data clearly show a SOC band splitting of 40 meV, consistent with the theoretical calculations which predict a SOC split of 39.5 meV. We further noticed anomalous temperature dependent resistivity in FeSi, that means, FeSi is a semiconductor respecting the activation energy formula only within the temperature range of 75-143 K and eventually becoming a bad metal as moving away from this temperature range. The spectral function analysis of ARPES data suggests an electron-phonon interaction at a Debye energy of 80 meV, while the spectral widths near the Fermi level change merely by the thermal excitations within the range of 15-80 K.

3.2 Experimental Details

Single crystals were grown using floating zone method [91, 161] by our collaborators Dr. Saicharan Aswartham, and Grigory Shipunov in IFW Dresden, Germany. As grown single crystals were characterized using X-ray diffractometer (XRD) and energy dispersive X-ray analysis (EDAX). These characterization techniques confirm the stoichiometric composition of FeSi and the space group of $P2_13$ (198) [147, 162]. More information on XRD and EDAX measurements of FeSi can be found from Fig. 3.1(a)-(b). Resistivity measurements were carried out on a closed cycle refrigerator (CCR) based cryostat of CRYOMECH. Four copper (Cu) leads were connected to the sample by vacuum compatible silver epoxy (Epo-Tek H27D) in Van der Pauw method. The sample temperature was varied between 5 and 310 K during the measurements.

ARPES measurements were carried out at 1^3-ARPES end station equipped with VG-Scienta R4000 electron analyzer in BESSY II (Helmholtz zentrum Berlin) synchrotron radiation center [163, 164] by Dr. Thirupathaiah Setti. The angular resolution was set at 0.2° for R4000. Photon energies for the measurements were varied between 30 and 110 eV. The energy resolution was set between 10 and 15 meV depending on the excitation energy. Data were recorded at a chamber vacuum of the order of 1×10^{-10} mbar and the sample temperature was kept at 1 K during the measurements. We employed various photon polarizations in order to extract the electronic structure comprehensively. Another set of

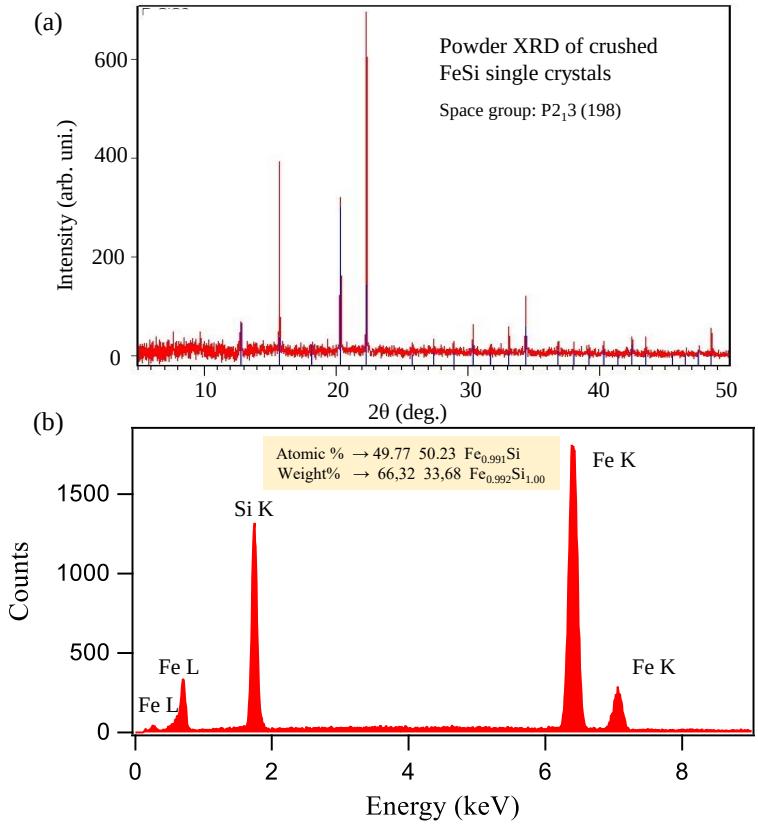

Figure 3.1: (a) Powder XRD measurements performed on the crushed FeSi single crystals. In the figure, XRD pattern from our samples is shown in red color, overlapped with the reference XRD pattern (blue color) of FeSi taken from the Inorganic Crystal Structure Database (ICSD). (b) Energy dispersive X-ray analysis (EDAX) data from the cleaved FeSi single crystals.

ARPES measurements were performed in Swiss Light Source (SLS) at the SIS beamline using a VG-Scienta R4000 electron analyzer. Photon energy was varied between 20 and 120 eV. Overall energy resolution was set between 15 and 25 meV depending on the photon energy. Samples were cleaved *in situ* at a sample temperature of 15 K and the chamber vacuum was better than 5×10^{-11} mbar during the measurements. At SIS beamline, the data were recorded by varying the sample temperature between 15 and 80 K.

3.3 Results and Discussions

Resistivity of FeSi as a function of temperature is shown in Figure 5.1. As can be seen from Figs. 5.1(c) and 5.1(d), the resistivity of FeSi decreases with increasing temperature

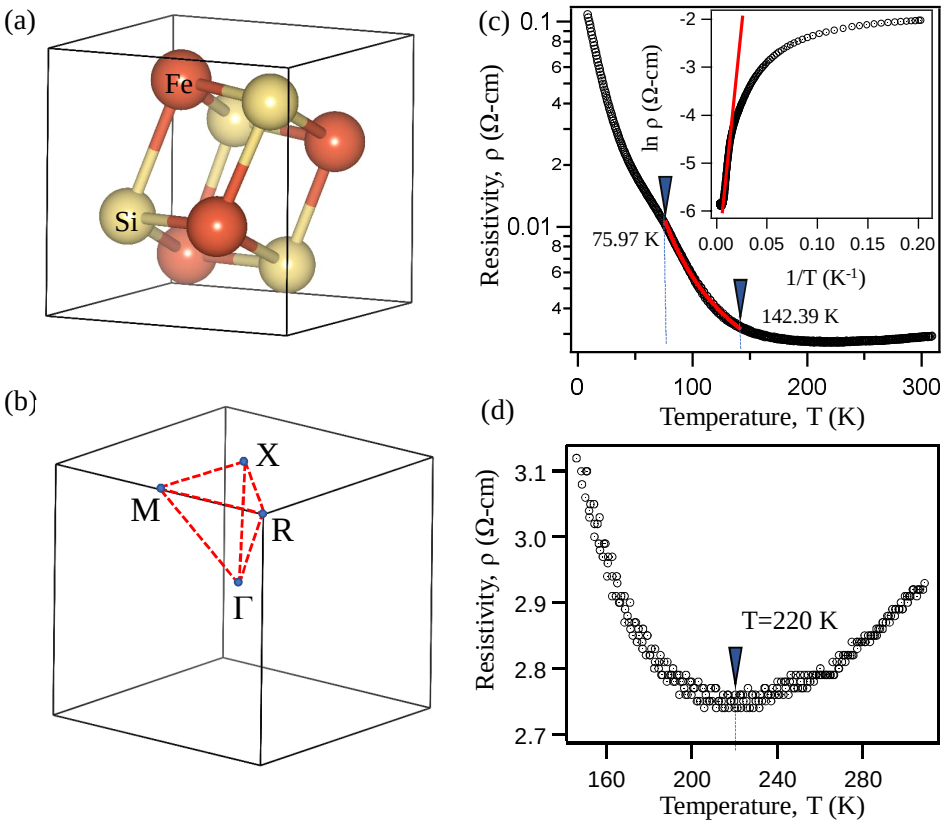

Figure 3.2: (a) and (b) are the cubic crystal structure and corresponding BZ of FeSi, respectively. (c) Temperature dependent resistivity. Red curve in (c) is the activation formula fitting. Inset in (c) is the ln(ρ) *vs.* 1/T. Red line in inset is the linear fitting. (d) Zoomed in resistivity data at high temperature, showing semiconductor to metal cross-over at T $\approx$ 220 K.

up to 220 K, like a semiconductor. However, from a close observation, we realise that FeSi is semiconductor only within the temperature range of 75-143 K as it can be properly fitted by the activation formula, $\rho(T) = \rho_0\ e^{(\frac{E_g}{2k_BT})}$, where E_g is the band gap. By fitting the resistivity data, as shown by the red line in the inset of Fig. 5.1(c), we estimate a semiconducting band gap of E_g=35 meV within this temperature range. The derived gap is in good agreement with previous report [140]. Further, we noticed a kink in the resistivity curve at around T = 75 K, below which $d\rho/dT$ decreases with decreasing temperature when compared to the projected semiconducting nature (see Fig. 3.3(a)). Similarly, we find that $d\rho/dT$ decreases with increasing temperature between 143 K and 220 K. As a result, from our systematic analysis (see Fig.3.3(a)), we identified that FeSi is a semiconductor with a maximum energy gap of 35 meV within the range of 75-143

K. Beyond this temperature range, the energy gap of the system rapidly decreases down to a negligible gap of 0.5 meV below 16 K (Fig.3.3(b)), indicating a bad metal [156]. The same is observed as the system goes above 143 K. And beyond 220 K, the resistivity increases with temperature in a metallic manner. This peculiar resistivity character below 75 K and above 143 K can be attributed to bad metalicity of FeSi [147, 155]. Thus, our resistivity measurements suggest that FeSi is a semiconductor following the activation formula within the temperature range of 75-143 K and gradually becomes a bad metal as we go away from this temperature range. These results are qualitatively in agreement with the existing reports, although the semiconducting temperature range is found to be different from different studies [148, 155, 162, 165–168].

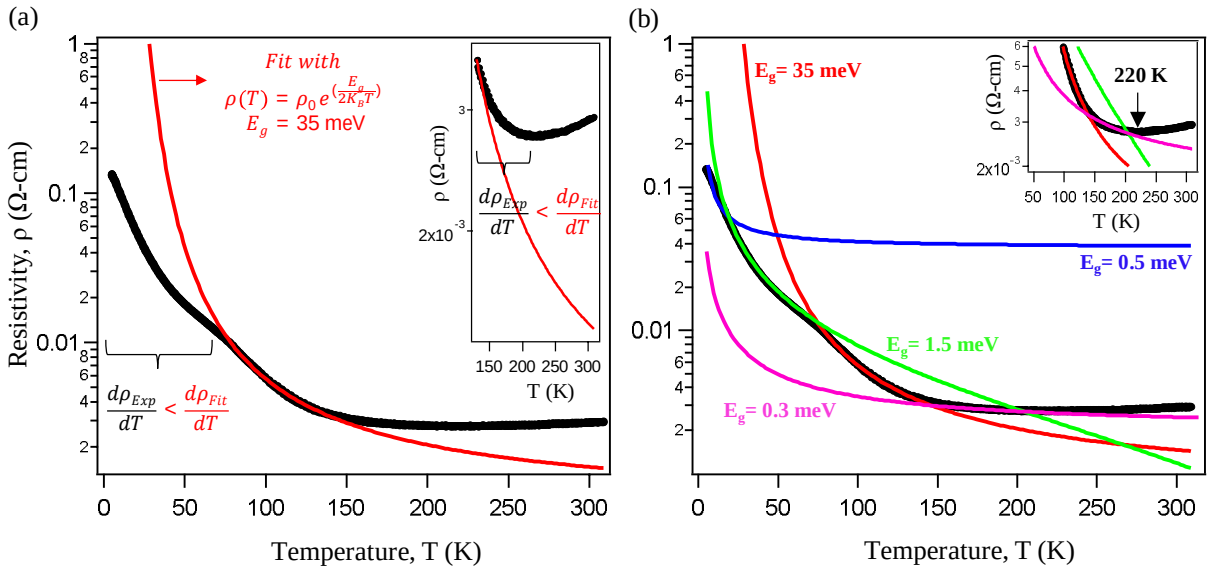

Figure 3.3: Resistivity data of FeSi single crystals. As can be seen from the panel (a), $d\rho/dT$ of the measured data decreases with decreasing temperature when compared to the projected semiconducting nature below 75 K. Similarly, between 143 K and 220 K, $d\rho/dT$ of the measured data decreases with increasing temperature. Inset in panel (a) shows the zoomed-in data between 130 K and 310 K. As can be seen from panel (b), to fit the experimental data within the range 5-220 K, one needs to consider at least four different energy gaps. That means, energy gaps of E_g = 0.5 meV, 1.5 meV, 35 meV, and 0.3 meV are required to fit the data in the ranges, 5-16 K, 16-75 K, 75-143 K, and 143-220 K, respectively, as demonstrated in panel (b). Beyond 220 K, the resistivity increases with temperature in a metallic manner as shown in the inset of panel (b). Therefore, the system FeSi is a semiconductor with a maximum energy gap of 35 meV within the range of 75-143 K. Beyond this temperature range, the energy gap of the system rapidly decreases down to a negligible gap of 0.5 meV below 16 K to become a bad metal. The same is happening as the system goes beyond 143 K.

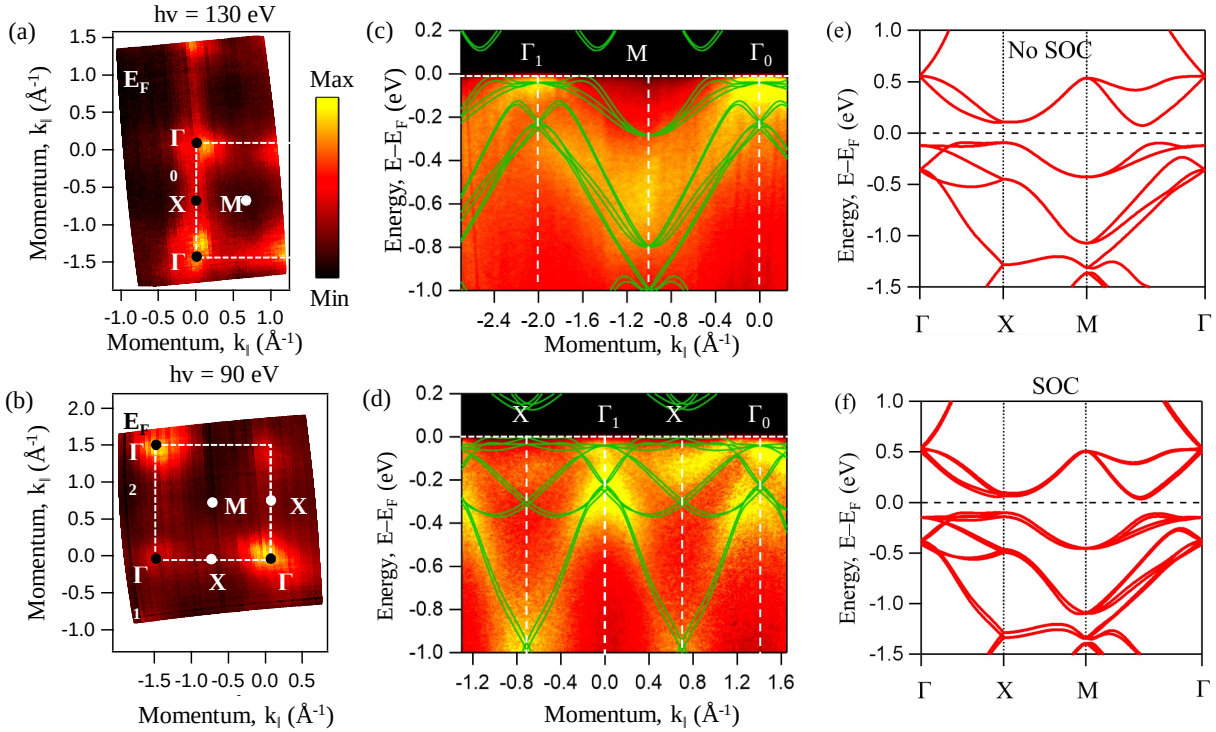

Figure 3.4: In-plane electronic band structure of FeSi. (a) and (b) are Fermi surface maps in $k_x - k_y$ plane measured using photon energy hν=130 eV and 90 eV, respectively. (c) Energy distribution map along the $\Gamma - M$ high symmetry line overlapped with DFT bulk band structure calculations including SOC. (d) Energy distribution map along the $\Gamma - X$ high symmetry line overlapped with DFT band structure calculations including SOC. (e) DFT calculated band structure without SOC. (f) DFT calculated band structure with SOC.

Next, ARPES data of FeSi is shown in Figure 5.2 recorded at a sample temperature of 1 K. Fermi surface maps in the $k_x - k_y$ plane are shown in Figs. 5.2 (a) and 5.2(b) measured using p-polarized light with photon energies of 130 eV and 90 eV, respectively. Consistent with the crystal structure, the in-plane Fermi surface (FS) maps show the square symmetry. From the FS maps, we identify a blob-like spectral intensity with fourfold symmetry at the Γ point. On the other hand, we did not observe any clear spectral intensity either at X or M point when measured using p-polarized light. To further elucidate the nature of band dispersions, we show energy distribution maps (EDMs) along the high symmetry lines $\Gamma - M$ and $\Gamma - X$ as shown in Figs. 5.2 (c) and 5.2(d), respectively, measured using p-polarized light. DFT bulk band structure including SOC along the respective high symmetry lines is overlapped on to the EDMs. As can be seen from Figs. 5.2(c) and 5.2(d), there is a good agreement between ARPES data and DFT

calculations. Note here that the Fermi level of DFT calculations is shifted approximately 100 meV towards the higher binding energy to match with the experimental Fermi level. Band structure from the DFT calculations without SOC and with SOC in the k path $\Gamma XM\Gamma$ are shown in Figs. 5.2(e) and 5.2(f), respectively. Further, using s-polarized light we could detect flat bands along the $\Gamma - X$ high symmetry line (see Fig. 3.5) which is in agreement with the DFT calculations. Thus, there is a finite spectral intensity at X point that is clearly visible with the s-polarized light. This suggests that the band structure of FeSi near the Fermi level is composed by the multiple orbital characters. More details on the polarization dependent matrix elements can be found at Ref. [169]. Importantly, in Fig. 5.2, we did not observe any spectral intensity related to the surface Fermi arcs. Overall, the ARPES data shown in Fig. 5.2 supports the bad metallic picture of FeSi at low temperatures as observed from our resistivity measurements. Worth to mention here that, in Fig. 5.2, for an easy representation, we did not take into account the k_z effects while assigning the high symmetry points on the Fermi surface maps and EDMs.

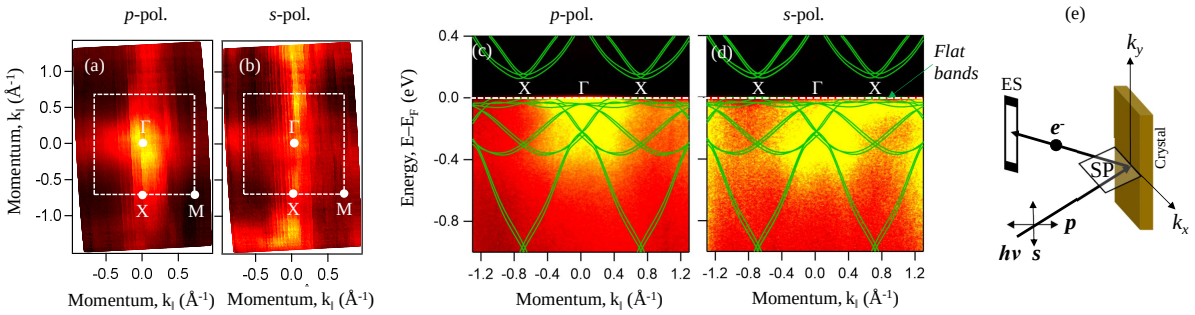

Figure 3.5: Polarization dependent Fermi surface maps measured with a photon energy of 100 eV. (a) p-polarization. (b) s-polarization. (c) and (d) are the EDMs taken along the $\Gamma - X$ orientation using p- and s- polarizations, respectively. (e) ARPES measurement geometry in which the s and p polarizations are defined with respect to the scattering plane (SP).

Photon energy dependent ARPES data are shown in Figure 5.3. Fig. 5.3 (a) shows $k_y - k_z$ Fermi surface map measured with the photon energies ranging from 75 eV to 108 eV with a step of 3 eV using p-polarized light. The high symmetry points Γ, X and R are denoted on the Fermi surface map following the equation, $k_z = \sqrt{\frac{2m}{\hbar^2}(V_0 + E_k \cos^2\theta)}$ with an inner potential of 16 eV. From the k_z Fermi surface map, we realize that the photon energy of 100±3 eV detects the bands from the Γ point and photon energy of 75±3 eV detects the bands from the X point. Similarly, the high symmetry point R is accessible with a photon energy of 86±3 eV when the sample surface is normal to the c axis. Energy

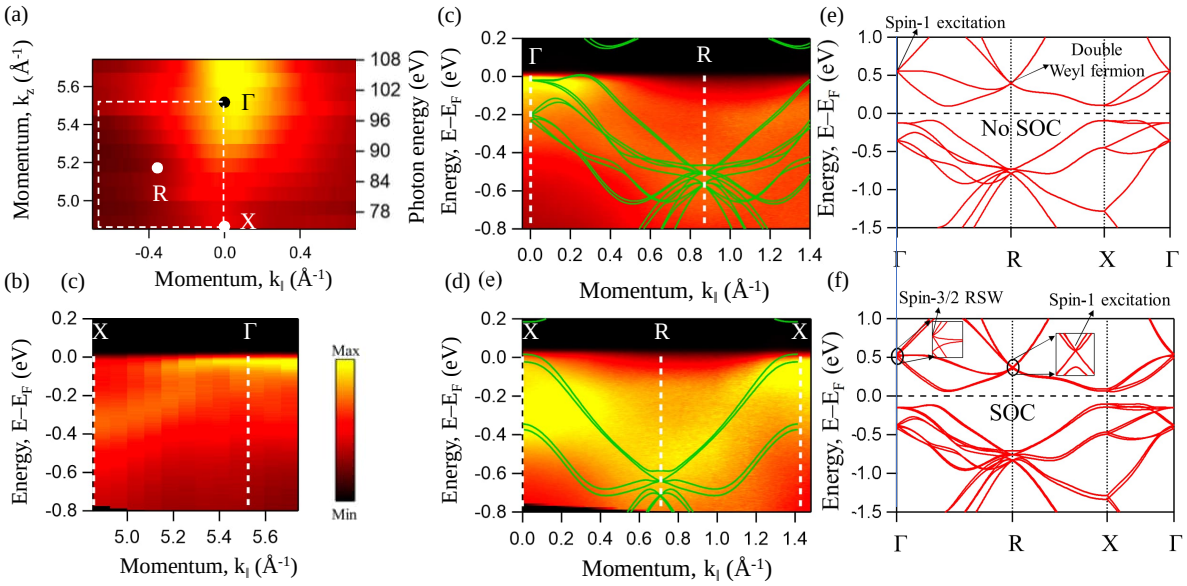

Figure 3.6: Out-of-plane electronic band structure of FeSi. (a) Fermi surface map in the $k_x - k_z$ plane. (b) Energy distribution map along Γ-X (001) high symmetry line. (c) Energy distribution map along the Γ-R high symmetry line overlapped with DFT band structure calculated including SOC. (d) Energy distribution map along the $X - R$ high symmetry line overlapped with DFT band struture calculated including SOC. (e) DFT band structure in the $\Gamma RX\Gamma$ without SOC and (f) with SOC.

distribution maps along $\Gamma - X$, $\Gamma - R$ and $X - R$ are shown in Figs. 5.3(b), (c), and (d), respectively. The band structure extracted along the in-plane $\Gamma - X$ ([100]) as shown in Fig. 5.3(b), is in good agreement with the band structure extracted along the out-of-plane $\Gamma - X$ ([001]) as shown in Fig. 5.2(d). The band structure derived from DFT calculations with SOC along $\Gamma - R$ and $X - R$ is overlapped on the experimental band structure as shown in Figs. 5.3(c) and (d), and there is a good agreement between DFT calculations and ARPES data. The calculated bulk band structure without SOC and with SOC in the k-path $\Gamma RX\Gamma$ are shown in Figs. 5.3(e) and (f), respectively. As predicted from the DFT calculations without SOC, in FeSi the triple-point spin-1 excitations with topological charge of ± 2 are at the Γ point and double Weyl fermions with topological charge of ± 2 are at the R point. On the other hand, DFT with SOC, the triple-point spin-1 excitations are predicted at the R point while the spin-3/2 Rarita-Schwinger-Weyl fermions are predicted at the Γ point [9].

Figure 5.4(a) depicts EDM along the $X - M$ orientation measured at a sample temperature of 15 K. From the second derivative of Fig. 5.4(a) as shown in Fig. 5.4(b) we identify two band dispersions, #1 and #2. Here, the band #1 is crossing the Fermi level with a

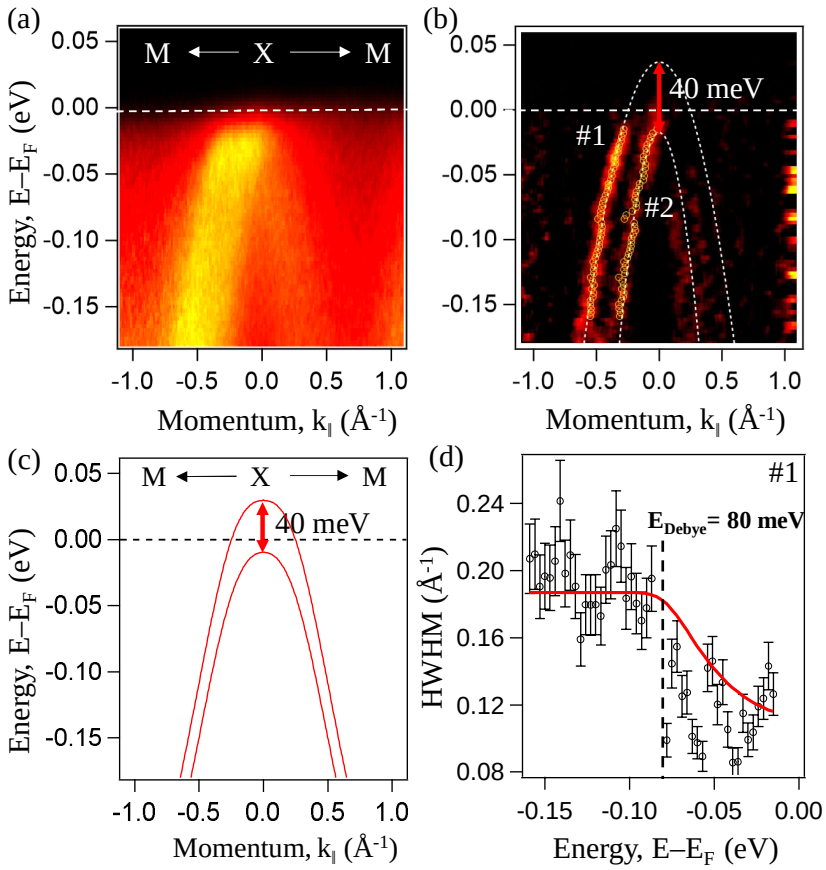

Figure 3.7: Temperature dependent ARPES data. (a) Energy distribution map along the $X-M$ high symmetry line measured using 90 eV photon energies at a sample temperature of 15 K. (b) Second derivative of (a). White dashed curves in (b) are the parabolic fits to the experimental bands. (c) Zoomed in DFT band structure along $X-M$ orientation. (d) Half width halm maximum (HWHM) as a function of binding energy extracted from the EDM shown in (a) by fitting the momentum dispersive curves (MDCs) with the Lorentzian function. In (d), the red curve is a fit of the self-energy function.

momentum vector of 0.22 Å^{-1} at the X point whereas the band #2 does not cross the Fermi level. Further, we estimate an energy difference between the top of #1 and #2 is about 40 meV, which is in good agreement with the DFT calculations with SOC which predicts it to be 39.5 meV as shown in Fig. 5.4(c). In fact, without SOC there exists only one band dispersion along $X-M$ orientation at this energy position [see Fig. 5.2(e)]. Thus, the experimental band structure can be properly reproduced using DFT calculations only with the SOC inclusion. To further elucidate temperature effects on the electronic band structure of FeSi, we measured EDMs along $X-M$ orientation with temperature ranging between 15 K and 80 K (see Fig. 3.8). From the temperature dependent EDMs as shown

in Fig. 3.8, it is evident that the band structure near the Fermi level hardly changes with the temperature at least within the range of 15-80 K. We further estimated half-width-half-maximum (HWHM) from MDCs which is directly related to the imaginary part of the self-energy ($\Im\Sigma(E)$) for the band #1 as shown in Fig. 5.4(d). By fitting HWHM using the self-energy function [170], we find electron-phonon coupling at a Debye energy of 80 meV. This estimate of Debye energy is in good agreement with an earlier ARPES report which suggested a Debye energy of 90 meV [144]. Thus, the anomalous resistivity observed in FeSi (see Fig. 5.1-3.3) may not be of the electronic structure origin. But, based on the spectral functional analysis, we suggest that the electron-phonon coupling is playing a crucial role for the observed anomalous resistivity also as suggested by the previous reports [148, 157, 171, 172].

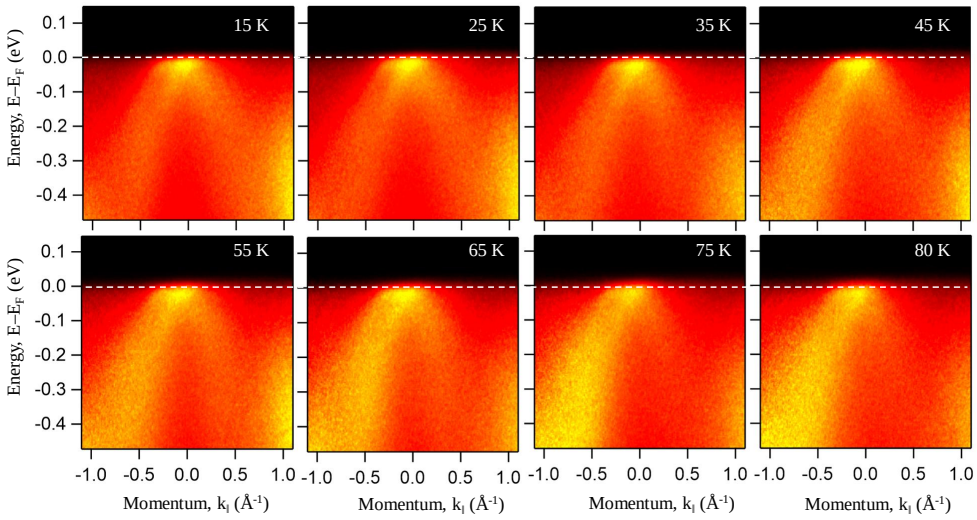

Figure 3.8: Temperature dependent ARPES data measured using *s*-polarized light with a photon energy of 90 eV.

Overall, the experimental band structure is quantitatively in agreement with the DFT calculations. Specially, the experimental observation of SOC band splitting has been explained very well from DFT calculations with spin-orbit interactions. Till date, a very few ARPES data with low energy and momentum resolution are available in the literature on FeSi, so it is difficult to compare quantitatively. However, qualitatively, our ARPES data is consistent with some of the earlier ARPES reports [144, 145]. Next, coming to the main point of this manuscript, recent ARPES and theoretical reports on CoSi and RhSi showed topological surface Fermi arcs spanned over a large area of 2D BZ [9, 10, 10, 87, 134–138, 173]. Moreover, they could record manyfold bulk Weyl fermions at Γ and

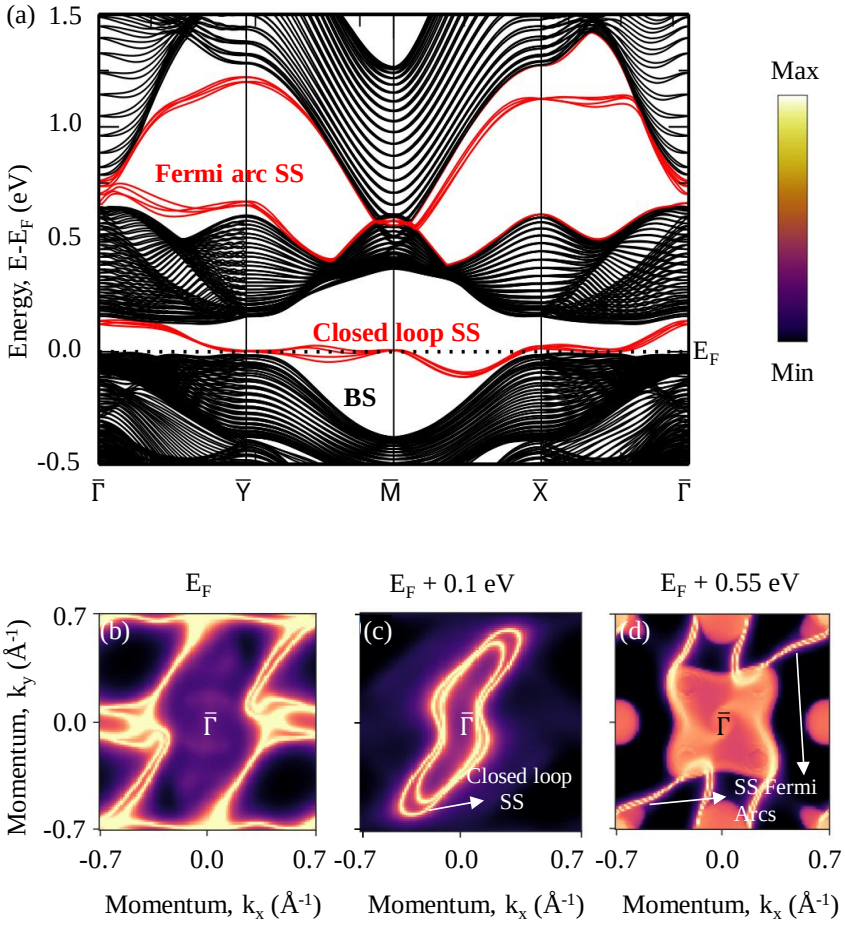

Figure 3.9: Band structure calculated for a (001) oriented FeSi slab of thickness 88.96Å. (a) Energy-momentum plot showing surface states (red colored) overlapped with the bulk band structure. Surface state Fermi map taken at E_F (b), E_F+0.1eV (c), and E_F+0.55eV (d).

R high symmetry points. In contrast, we could not observe any such surface Fermi arcs from our ARPES measurements performed on the isostructural FeSi. As predicted by the DFT calculations [see Fig. 5.3(f)], in FeSi, the manyfold spin-3/2 RSW fermions are at 0.54 eV and the triple-point spin-1 excitations are at 0.37 eV above the Fermi level. So, it would not be possible to measure them using ARPES technique. Nevertheless, based on the present understanding, irrespective of the energy position of the manyfold BCPs one would expect the associated Fermi surface arcs on the surface BZ [26, 174, 175].

Therefore, to gain more insight into the surface band structure of FeSi, density functional theory calculations (see Fig. 3.9) were carried out by our collaborators Anumita Bose, and Dr. Awadhesh Narayan in IISC, Bangalore, India. They constructed a wannier function

based model to compute the band structure of FeSi slab oriented along the [001] direction. The band structure, for a slab of thickness 88.96 Å, along the high symmetry directions is shown in Fig. 3.9(a). Most noticeably, we find only a set of trivial surface bands within the bulk band gap, and the absence of any topological protected Fermi arcs close to the Fermi level. The topological Fermi arcs, associated with manyfold fermions similar CoSi and RhSi, occur at substantially higher energies (0.55 eV above the Fermi level). Furthermore, we also considered the semi-infinite geometry, employing a Green's function method to calculate the surface states, as a function of the in-plane momenta, at different energies. These are presented in Fig. 3.9(b)-(d). In stark contrast to the case of CoSi, we find that these surface states near the Fermi level close-in on themselves as shown in Figs. 3.9(b) and 3.9(c), clearly indicating the triviality of these states. The reciprocal space extent of these surface states diminishes as one moves away from the Fermi energy, with the closed loops shrinking in size. However, though the shape of the Fermi arcs is a bit different from CoSi and RhSi, the non-trivial topological Fermi arcs can be noticed in FeSi at 0.55 eV above the Fermi level as shown in Fig. 3.9(d). Thus the surface state calculations indicate that the topological Fermi arcs present in FeSi, however, they are not accessible by conventional ARPES technique. Further, these calculations predicted trivial surface states near the Fermi level which are not well resolved in our ARPES data due to either the surface state spectral intensity is very low compared to the bulk spectral intensity or the sample surface quality is not good enough to detect them.

3.4 Conclusions

We systematically studied the low-energy electronic structure of topological chiral fermionic system, FeSi, using angle-resolved photoemission spectroscopy and density functional theory to derive the following conclusions,

1. Observation of Fermi surface from the ARPES measurements suggest that FeSi is a metal at low temperature, in agreement with our resistivity measurements.

2. Anomalous temperature dependent resistivity of FeSi can be explained by the electron-phonon interactions.

3. ARPES data show a spin-orbit band splitting of 40 meV that is nicely reproduced by the DFT calculations including SOC. Therefore, SOC effects must be considered while

discussing the physics of manyfold degenerate fermions in the transition metal monosilicides.

4. Unlike in the case of CoSi or RhSi, FeSi does not show topological surface Fermi arcs near the Fermi level as the surface state calculations predict them well above the Fermi level. Therefore, we are unable to detect the non-trivial TSSs in FeSi experimentally using the conventional ARPES technique.

Chapter 4

ARPES studies on $K_{0.65}RhO_2$: a predicted topological system

We identify highly correlated hole pocket on the Fermi surface of colossal thermoelectric material $K_{0.65}RhO_2$, studied using high-resolution ARPES and DFT calculations. Most importantly, two *kinks* at binding energies of 75 and 195 meV have been observed below the Fermi level. While the low-energy *kink* at 75 meV can be understood as a result of the electron-phonon interaction, the high-energy *kink* at 195 meV is totally a new discovery of this system, leading to anomalous band renormalization, possibly originated from the bosonic excitations at higher frequencies. We further notice that the high-energy anomaly has important implications on the colossal thermoelectric power of $K_{0.65}RhO_2$.

Results presented in this chapter are published in Phys. Rev. Materials 5, 055402 (2021)

4.1 Introduction

Strong electronic correlations are vital in yielding various exotic systems like, high-T_c superconductors [176], heavy fermionic materials[177], quantum anomalous Hall (QAH) insulators [178], half-metals [179], Mott-insulators[180], itinerant magnets [181], and high thermopower materials[182]. Electron-electron (*e-e*) correlations turn the materials to heavy fermionic systems, QAH insulators, half-metals and Mott-insulators, while the electron-magnon interactions are expected to cause the itinerant ferromagnetism [183, 184]. On the other hand, the electron-phonon (*e-ph*) interactions are thought to be playing a major role in the high-T_c superconductivity [185] and high thermoelectricity [186]

For a quite some time, the compounds of the type A_xBO_2 (A = Li, Na, and K, B = Co and Rh) have been the scientific topic of much interest due to their diverse physical properties [187–190]. Interestingly, depending on the amount of Na present in Na_xCoO_2, it exhibits superconductivity in the hydrated state for $x \approx 0.35$ [191], shows giant Seebeck coefficient for $0.7 < x < 1$ [192], possesses magnetic ordering for $x \approx 0.75$ [193, 194] and charge ordering for $x \approx 0.5$ [195]. Crystal field splitting [196], strong spin-orbit interactions [197], electron-electron [198], and electron-phonon interactions [199] are suggested for the cause of unusual physical properties. $K_{0.5}RhO_2$ has recently been predicted to be a quantum topological Hall insulator in its noncoplanar AFM phase [6], which we have discussed in details in section 1.4. Since, $K_{0.63}RhO_2$ is reported to exhibit such AFM ordering up to 50 K [200], we thoroughly investigated the low-energy electronic band structure of the layered $K_{0.65(2)}RhO_2$ single crystal using ultrahigh energy resolution ARPES technique for a better understanding of its topological properties.

4.2 Experimental details

Our collaborators, Grigory Shipunov and Dr. Saicharan Aswartham from IFW Dresden, Germany, successfully grew single crystals of K_xRhO_2 using a mixture of K_2CO_3 and Rh_2O_3. The total charge mixture of 4.5 grams was placed in an alumina crucible and heated to the 1200°C in a box furnace, after a dwelling time of 2 hours, the furnace is slowly cooled to 950°C and later fast-cooled to the room temperature. Plate-like hexagonal-shaped single crystals were grown at the bottom of the crucible. Crystals were grown in layered morphology in hexagonal structure up to few mm^2 in size. Compositional analysis

from EDX gives the phase with the stoichiometry $K_{0.65(2)}RhO_2$. As grown single crystals were crushed and measured with powder XRD (Fig.4.1(f)).

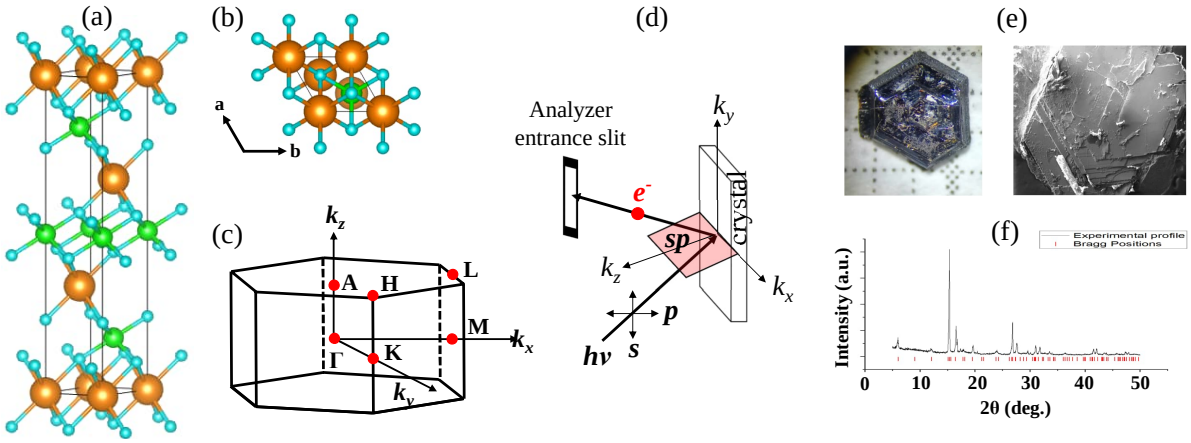

Figure 4.1: (a) Crystal structure of $KRhO_2$. (b) Projected crystal structure onto the *ab*-plane. (c) Hexagonal BZ with identified high symmetry points. (d) ARPES measurement geometry. In (d), the s and p polarized lights are defined with respect to the scattering plane (sp) which is parallel to the xz plane. (e) As grown plate-like hexagonal crystals of $K_{0.65(2)}RhO_2$ (left) and SEM image (right). (f) XRD data of crushed $K_{0.65}RhO_2$ single crystals.

ARPES measurements were performed in Swiss Light Source (SLS) at the SIS beamline using a VG-Scienta R4000 electron analyzer. Photon energy was varied between 20 and 140 eV. Overall energy resolution was set between 15 and 25 meV depending on the photon energy. The angular resolution was fixed at 0.2°. Samples were cleaved *in situ* at a sample temperature of 15 K and the chamber vacuum was better than 5×10^{-11} mbar during the measurements.

4.3 Results and discussions

ARPES data of $K_{0.65}RhO_2$ are shown in Figure 5.1. From the Fermi surface map shown in Fig. 5.1(a), we observe one nearly circular-shaped Fermi pocket centred at Γ with a Fermi vector of k=0.51±0.02 Å^{-1}. From the constant energy contour taken at a binding energy of 0.25 eV, shown in Fig. 5.1(b), we observe six tiny spectral sheets near six K points. Moreover, at this binding energy, size of the Fermi pocket centred at Γ has increased and the circular shape is turned into hexagonal shape. Energy distribution maps (EDMs) taken along the Γ-M, Γ-K, K-M directions [see the top panels in Fig. 5.1(c)] suggest

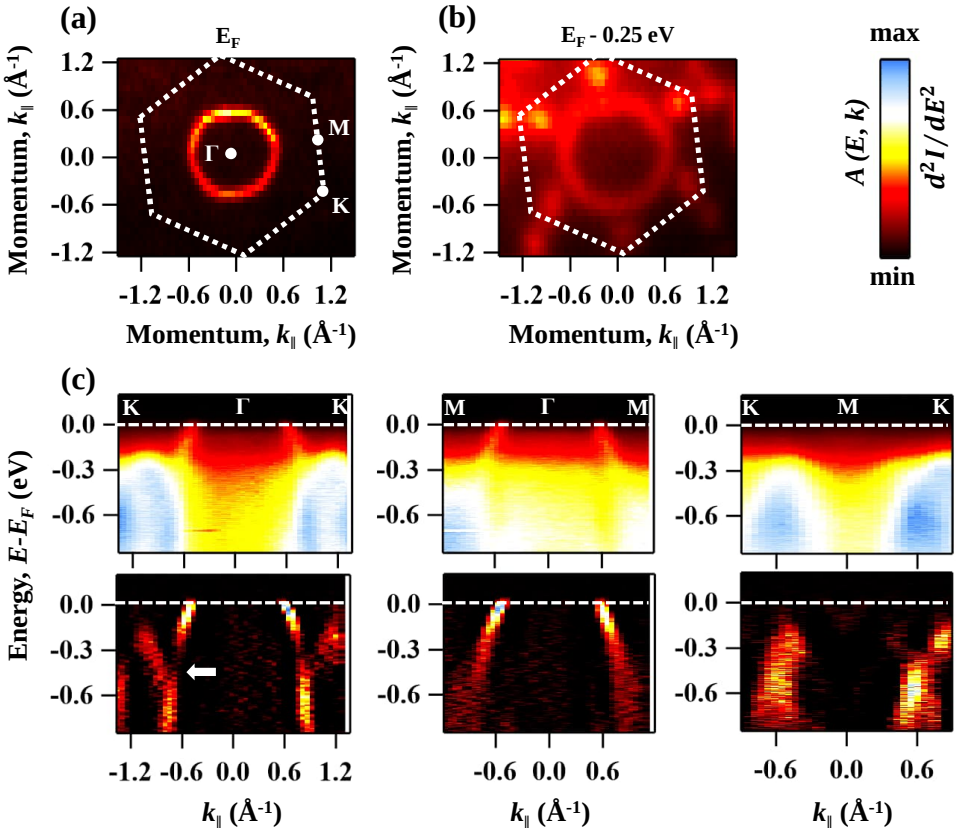

Figure 4.2: ARPES measurements of $K_{0.65}RhO_2$. The data is measured using p-polarized light with a photon energy of 140 eV. (a) Fermi surface map. (b) Constant energy map taken at a binding energy of 0.25 eV below E_F. (c) Energy distribution maps (EDMs) showing the band dispersions along the Γ-K, Γ-M, and $M-K$ high symmetry directions.

that Fermi sheet centred at Γ has holelike band dispersion. Further from the EDMs taken along the Γ-K and K-M directions, we realize that the tiny spectral sheet near the K point is originated from another holelike band dispersion with a band-top at 0.25 eV below E_F. This is further confirmed from the 2^{nd} derivative intensity (I) of the EDMs ($\frac{d^2I}{dE^2}$) as shown in the bottom panels of Fig. 5.1(c). Arrow on the 2^{nd} derivative EDM in the Γ-K direction indicates an antiband crossing between the two holelike band dispersions at ≈ 0.4 eV below E_F. Above this binding energy, the two holelike bands are well separated in the momentum space. Importantly, no antiband crossing is found from the 2^{nd} derivative EDM in the Γ-M direction, down to 0.8 eV of the binding energy. Next, comparing our experimental band structure with the available ARPES data on these type of systems, analogous to Na_xCoO_2 [201–203] and Li_xCoO_2 [204], we could also observe only one circular-shaped hole pocket from the Fermi surface map. Most importantly, in agreement with the previous report on $K_{0.62}RhO_2$ [205], we identified an antiband crossing at ≈ 0.4

eV below E_F in Γ-K direction. Further, the top of holelike band at the K point is found nearly at the same binding energy of 0.25 eV.

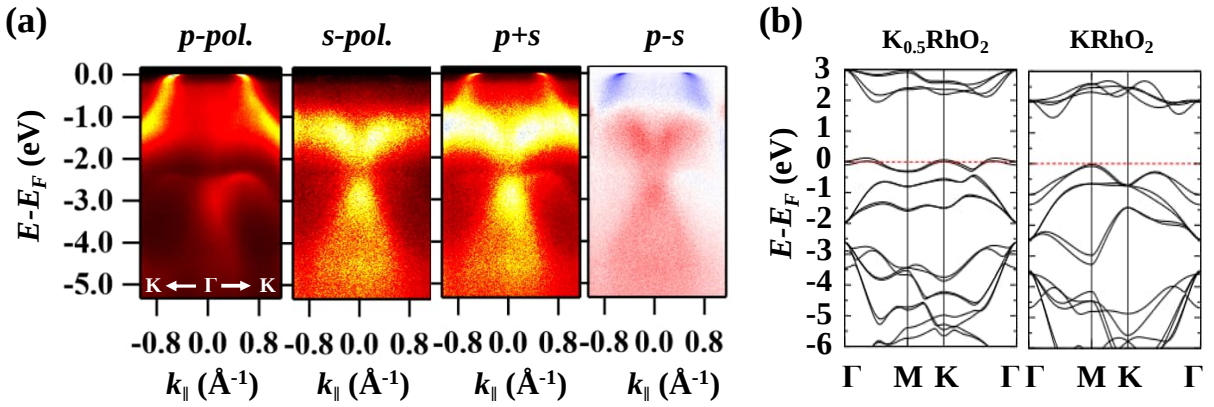

Figure 4.3: Panels in (a) from left to right represent the Energy distribution maps measured with 60 eV photon energy using p-, s- polarized lights, sum of p and s, and difference between p and s, respectively. Left panel in (b) represents an energy-momentum plot of $K_{0.5}RhO_2$ and right panel in (b) represents an energy-momentum plot of pristine $KRhO_2$ obtained from the DFT calculations.

First principles calculations were carried out based on density functional theory as implemented in quantum espresso code [206] by our collaborators, Nesta B. Joseph and Dr. Awadhesh Narayan from IISC bangalore, India. Comparison between our ARPES data and DFT calculations are presented in Fig. 4.3. As observed from the panels of Fig. 4.3(a), EDMs taken along the Γ-K direction, the bands dispersing from the Fermi level down to 1 eV are only accessible with p-polarized light, while the bands below 1 eV are accessible with s-polarized light. We can conclude from this observation that the a_{1g} band that is dominating in the vicinity of E_F has even parity [207], while the $e_g^{'}$ bands dominating below 1 eV have the odd parity with the respect to our measuring geometry [see Fig. 4.1(d)]. By subtracting s-polarized data with the p-polarized as shown in $p-s$ panel of Fig. 4.3(a), we can clearly disentangle the even-parity states (blue colored) from the odd parity states (red colored). Adding both the data of p- and s-polarized lights ($p+s$), we can compare the experimental band dispersions with the DFT calculations along the Γ-K direction in Fig. 4.3(b). From this comparison we realize that the experimental band dispersions qualitatively agree with the DFT calculations of $K_{0.5}RhO_2$. That means, the holelike band dispersions noticed from ARPES both at the Γ and K points are also reproduced from DFT. However, while experimentally the top of holelike band near K is at around 0.25 eV below E_F, the DFT calculations suggest that these bands cross

E_F. Importantly, the overall agreement between DFT calculation for the bulk and the ARPES data indicates absence of any topologically protected surface states in the material. Our measurements were conducted at a temperature below the Néel temperature (50 K) yet, we did not identify any surface bands in the system. Despite the seemingly non-trivial topological characteristics inferred from the ARPES data, our current investigation revolves around uncovering other intriguing properties of the material that could still be observed.

Having thoroughly established the low energy electronic structure of $K_{0.65}RhO_2$, experimentally, we then move on to the spectral function analysis of our experimental data. The band dispersion shown in Fig. 5.2(b) is extracted from the EDM of Fig. 5.2(a) by fitting the momentum distribution curves (MDCs) with a Lorentzian function, analogous to the spectral function $A(E,k) = \frac{-1}{\pi}\frac{\Sigma''}{(E_k - E_0 - \Sigma')^2 + (\Sigma'')^2}$. Here, $\Sigma'(E)$ and $\Sigma''(E)$ are the real and imaginary parts of the complex self-energy function defined as $\Sigma(E) = \Sigma' + i\Sigma''$. E_k is the renormalized band dispersion which is generally obtained from the ARPES measurements [see Fig. 5.2(b)] and E_0 is the bare band dispersion which is generally obtained by fitting the tight-binding parameters to the experimental data. Nevertheless, the bare band dispersion can also be obtained reasonably by fitting experimental data at higher binding energies where the electronic correlations are negligible. The black-dashed curve in Fig. 5.2(b) is one of such fitting at the higher binding energies. Then, the difference between E_k [orange data in Fig. 5.2(b)] and E_0 [solid black line in Fig. 5.2(b), momentum offset to the dashed black line] provides the real part of the self-energy $\Sigma'(E) = E_k - E_0$ as shown in Fig. 5.2(c). On the other hand, the imaginary part of self-energy shown in Fig. 5.2(d) is calculated from the energy dependent spectral width [$\Delta k(E)$], derived from the MDC fitting, multiplied by the renormalized Fermi velocity (v_F=0.6 eV-Å), $\Sigma'' = \Delta k(E) v_F$.

Most interestingly, we observe two *kinks* from the band dispersion shown in Fig. 5.2(b). These *kinks* have direct implications on the real and imaginary parts of the self-energy as shown in Figs. 5.2(c) and 5.2(d), respectively. Means, Σ'' posses two humps corresponding to these two *kinks*. In order to understand origin of the hump, we performed a fitting to Σ'' using multiple Eliashberg spectral functions [green dashed curves in Fig. 5.2(d)] following the Debye model [208]. The fitting resulted in two Debye frequencies 75±6 meV and 195±10 meV which are very much in agreement with the energy positions of the *kinks* found from the band dispersion [Fig. 5.2(b)]. In addition to multiple Eliashberg spectral functions, we needed to add a Fermi liquid-type spectral function [red dashed

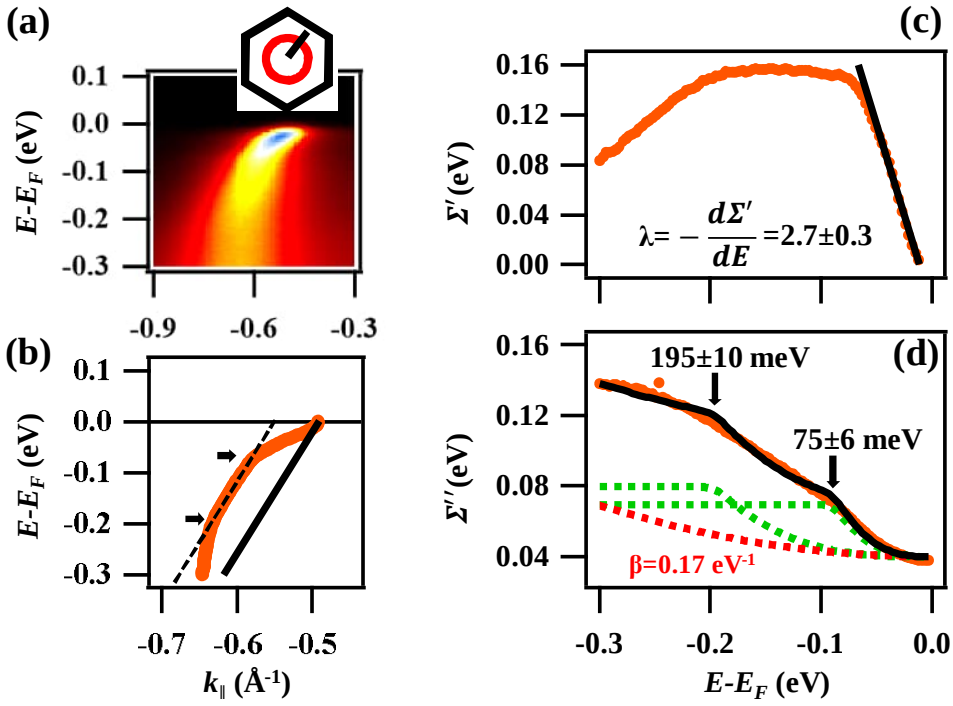

Figure 4.4: (a) Energy distribution map taken along the Γ-M orientation as shown in the inset. (b) Band dispersion extracted by fitting the momentum distribution curves of the EDM shown in (a) using a Lorentzian function. Black dashed line in (b) is a linear fit to band dispersion at the higher binding energy within the window of (-0.2eV, -0.09eV). The arrows in (b) show the energy positions of the *kinks*. (c) Real part of the self-energy ($\Sigma^{'}$) extracted from the EDM shown in (a). In (c), the black line is linear fit to the data performed to extract the coupling constant $\lambda = 2.7 \pm 0.3$. (d) Imaginary part of the self-energy ($\Sigma^{''}$) extracted from the EDM shown in (a). In (d), the black curve represents fitting with combined functions of Fermi liquid theory-type and Eliasberg spectral functions (see the text).

curve in Fig. 5.2(d)], $\Sigma^{''}(E) = \alpha + \beta E^2$, to properly fit $\Sigma^{''}$ for the binding energies beyond 0.2 eV. Here, α represents the spectral width due to impurity scattering and β represents the strength of e-e correlations. The derived β value of 0.17±0.03 eV^{-1} suggest weak e-e correlations in $K_{0.65}RhO_2$ compared to other high thermoelectric system having a β value of 1.7 eV^{-1} [209]. We extracted a total coupling constant λ=2.7±0.3 by fitting $\Sigma^{'}(E)$ linearly with the formula of $\lambda = -\frac{d\Sigma^{'}}{dE}$ near E_F as shown in Fig. 5.2(c). Interestingly, this value is quite high compared to the coupling constant (λ=0.4) reported earlier on $K_{0.62}RhO_2$ [205]. The differing coupling constants could have originated from the additional band renormalization due to the high energy anomaly at 195 meV. It is worth to mention here that such high value of coupling constants are also noticed from

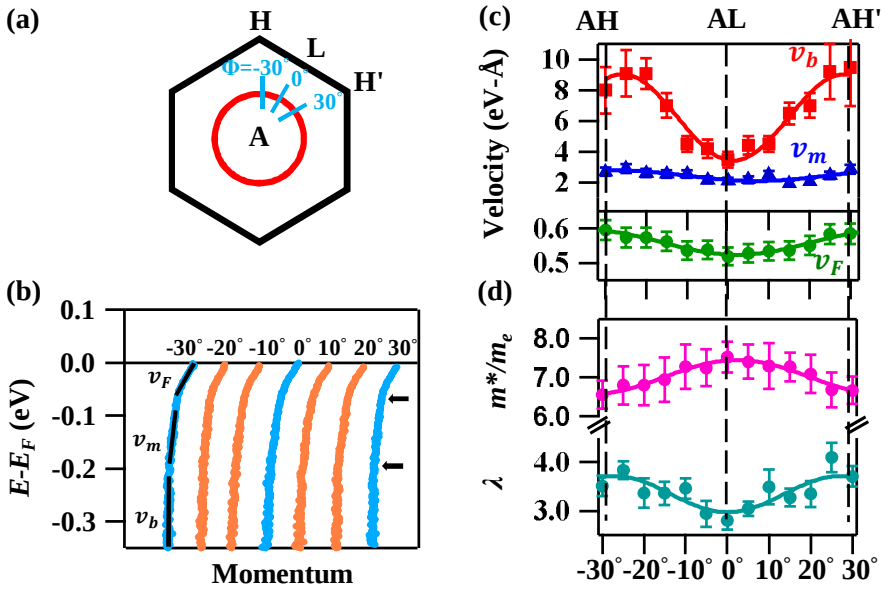

Figure 4.5: (b) In-plane momentum dependant band dispersions extracted from the EDMs taken along the cuts by varying Φ as shown in (a). (c) In-plane momentum dependant Fermi and group velocities extracted by fitting with linear function within the binding energy windows as defined in (b). (d) In-plane momentum dependent coupling constant (λ) and carrier effective mass (m^*/m_e). In (c) and (d) the data are fitted with cosine functions.

the high T_c superconductors [210]. In Ref. [210], a total coupling constant of $\lambda = 3.9$ has been reported for $(Bi,Pb)_2Sr_2CaCu_2O_{8+\delta}$ (Bi2212), with the *e-ph* interaction contribution of 2.3 and band renormalization contribution of 1.6. Following the same analogy, we subtracted the band renormalization contribution ($\lambda_b = \frac{v_b}{v_m} - 1$=1.2±0.1) from the total coupling constant to obtain an *e-ph* coupling constant of λ_{e-ph}=1.5±0.4. This value, within the error-bars, is in good agreement with the coupling constant independently obtained from the imaginary part of self-energy [210], $\lambda_{e-ph} = \frac{2\Sigma''(-\infty)}{\Omega_0 \pi}$=1.19±0.1. Here $\Sigma''(-\infty)$=140 meV and Ω_0=75±6 meV. Further in supporting our observation, a coupling constant of λ_{e-ph}=1 has been estimated for the multiboson-electron scattering in case of the misfit cobaltate, $[Bi_2Ba_2O_4][CoO_2]_2$ [209] which has the identical CoO_2 slabs to those in Na_xCoO_2.

In-plane electronic correlations are evaluated for the AHL plane as shown in Figure 5.3. Fig. 5.3(b) depicts representative band dispersions taken along the cuts AH, AL, and AH' by rotating Φ=-30° to 30° as demonstrated in Fig. 5.3(a). From Fig. 5.3(b), we can again observe multiple *kinks* from the all band dispersions almost at the same binding energy

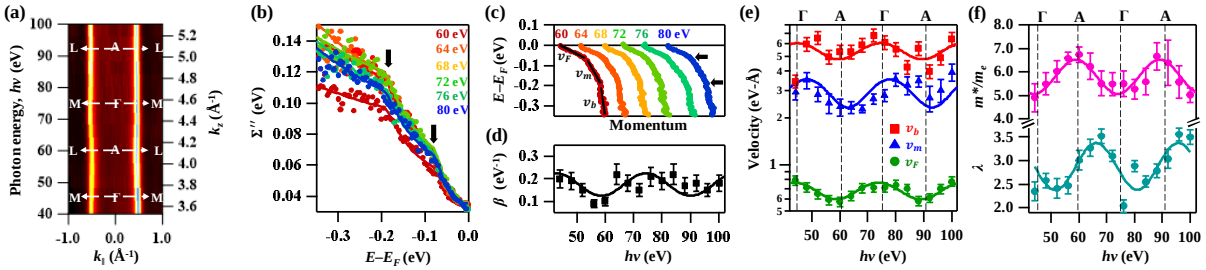

Figure 4.6: (a) Out-of-plane Fermi surface map taken in the $k_z - k_{\|}$ plane. (b) Representative k_z ($h\nu$) dependent imaginary part of the self-energy Σ''. (c) Representative k_z dependent band dispersions. (d) k_z dependent strength of electron-electron correlation extracted by fitting with Fermi liquid-type spectral function (see the text). (e) k_z dependent Fermi and group velocities extracted by fitting with linear function within the binding energy window as shown in (c). (f) k_z dependent coupling constant and carrier effective mass. In (d) and (e) the data are fitted with cosine functions.

of 75 meV and 195 meV. We also estimated Fermi velocity v_F, and group velocities, v_m and v_b, by fitting the band dispersions linearly in the binding energy windows (0, 0.07) eV, (0.1, 0.2) eV, and (0.21, 0.3) eV, respectively. The calculated Fermi and group velocities vary sinusoidally with Φ as shown in Fig. 5.3(c), having maximum Fermi and group velocities, v_F=0.6±0.03 eV-Å, v_m=2.9±0.5 eV-Å, v_b=9.1±1 eV-Å along the AH direction and minimum Fermi and group velocities, v_F=0.52±0.02 eV-Å, v_m=2.1±0.3 eV-Å, v_b=3.5±0.5 eV-Å along the AL direction. These observations are consistent with the reported Φ dependent Fermi velocities of Na_xCoO_2 [211]. The total coupling constant (λ) and the effective mass of the hole pocket, $m^* = \frac{\hbar k_F}{v_F}$, as a function of Φ are plotted in Fig. 5.3(d). From Fig. 5.3(d), we can notice that the coupling constant is maximum (λ=3.7) for the electrons dispersing along AH and is minimum (λ=2.9) for the electrons dispersing along AL. Further, the effective mass is minimum ($m^* = 6.5\ m_e$) along AH and is maximum ($m^* = 7.4\ m_e$) along AL.

Next, electronic correlations have been evaluated for the out-of-plane momentum (k_z) direction as shown in Figure 5.4. Fig. 5.4(a) depicts the Fermi surface (FS) map taken in the $k_z - k_{\|}$ plane by varying the photon energy ($h\nu$) between 40 and 100 eV insteps of 4 eV. As can be seen from the k_z FS map, no change in the Fermi vector is noticed along the k_z direction, suggesting a nearly 2D hole pocket without electron hopping in the k_z direction. In Fig. 5.4(b) we show representative imaginary part of the self-energy extracted from the EDMs measured with varying photon energies (k_z dependent). From each photon energy data, we consistently observe two humps in $\Sigma''(E)$, within the error-

bars almost at the same binding energies of 75 meV and 195 meV. This is in very good agreement with *kinks* observed from the band dispersions extracted from corresponding photon energies [see Fig. 5.4(c)]. As discussed earlier, we could reasonably fit Σ'' at every photon energy using combined double-Eliashberg and Fermi liquid-type spectral functions as shown in Fig. 5.4(b). We estimated β from the fittings and is plotted as a function of k_z (hν) as shown in Fig. 5.4(d). From Fig. 5.4(d), we can notice that the $e-e$ correlations hardly change along k_z (within the error-bars). The estimated Fermi and group velocities are plotted in Fig. 5.4(e) as a function of k_z. From Fig. 5.4(e), we can notice that all the velocities vary sinusoidally with k_z having minima at 60 and 92 eV and maxima at 43 and 75 eV photon energies. By considering the inner potential V_0=12±2 eV and using the formula $k_z = \sqrt{\frac{2m}{\hbar^2}(V_0 + E_k)}$, we identify that the photon energies 60 and 92 eV extract the bands from the AHL plane and the photon energies 45 and 75 eV extract the bands from the ΓMK plane. Thus from Fig. 5.4(e), we can find that the Fermi velocity is minimum at the A point (v_F=0.6±0.04 eV-Å) and is maximum at the Γ point (v_F=0.76±0.06 eV-Å). Similarly, the group velocities v_m and v_b are minimum at A (2.3±0.3, 4.76±0.5) eV-Å and are maximum at Γ (3.53±0.5, 6.06±0.8) eV-Å. With the help of Fermi velocity and Fermi momentum, we estimated the effective mass of the hole pocket and plotted them as a function of k_z as shown in Fig. 5.4(f). A maximum effective mass is realized ($m^* = 6.51\ m_e$) at A, while a minimum effective mass is realized ($m^* = 5.06\ m_e$) at Γ. Further, the k_z dependent total coupling constants are plotted in Fig. 5.4(f). Note here that the maximum (λ=3.37) and minimum (λ=2.38) coupling constants are shifted by hν=5 eV from the photon energy positions of the high symmetry points, while still the photon energy difference between the two extrema is invariant (≈ 15 eV).

Since we completely extracted the in-plane and the out-of-plane Fermi sheets using ARPES, with the help of Luttinger's theorem [212], we are able to estimate the hole carrier density n_h=0.33±0.03 per unit cell. This value is in very good agreement with the K deficiency percentage of the measured sample $K_{0.65(2)}RhO_2$ (1-x=0.35±0.02) from the stoichiometric $KRhO_2$. Thus, the ARPES data confirm EDAX estimate of the chemical composition. As clearly demonstrated from our ARPES data, $K_{0.65}RhO_2$ possess two *kinks*. While the *kink* at 75 meV is consistent with the previous studies of Raman spectroscopy showing active $E_{1g} + E_{2g} + A_{1g}$ Raman modes at around 500 cm^{-1} from $K_{0.63}RhO_2$ [213], the high energy *kink* at 195 meV is totally new a finding of this study. Though the origin of low energy *kink* is reasonably understood, the origin of HE *kink* is yet to be established. So

far existing ARPES studies on these systems did not concentrate on the electronic correlations beyond 0.2 eV binding energy. Therefore, we are unable to compare the HE *kink* directly with previous ARPES studies of these systems. Nevertheless, as can be seen from Figs. 5.2 and 5.4, we can reasonably fit $\Sigma''(E)$ with multiple Debye frequencies at 75 meV and 195 meV. This suggests a plausible phononic origin for the HE *kink*. In fact, such an observation of bosonic scattering at higher energies has been noticed from Fe (100) at $\approx$ 160 meV [214], graphene at $\approx$ 200 meV [215], and cuprates at $\approx$ 350-400 meV below E_F [216, 217]. The other existing mechanisms for the HE anomaly are the matrix element effects [218, 219] and spin-fluctuations [220]. As observed in this study and reported in the literature, near the Fermi level only one band disperses from E_F down to a binding energy of 0.4 eV [205, 221]. The same has been confirmed from the DFT calculations as well, especially, in AHL plane [207]. Since the observed HE *kink* is at around 195 meV and only one band dispersion present within this energy range, it is highly unlikely that the HE *kink* originated from the matrix elements. Further, the spin-fluctuations origin can be negated as the transport properties of $K_{0.65}RhO_2$ are nearly insensitive to the applied magnetic fields down to the lowest possible temperature [222]. Finally, as demonstrated in Fig. 5.1 the antiband crossing occur at $\approx$ 0.4 eV below E_F which shows no effect on the *kink* at 195 meV, ruling out the band structure origin as well. Hence, the only convincing mechanism for the HE *kink* must be the electron-boson scattering at higher frequencies. But the present available literature on these systems is insufficient to confirm the same.

Our estimate of average Fermi velocity over the entire BZ v_F=0.62$\pm$0.04 eV-Å is far less than the Fermi velocity (v_F=0.96$\pm$0.02 eV-Å) reported earlier on $K_{0.62}RhO_2$ [205]. On the other hand, the average carrier effective mass estimated from this study, m^*=6.44m_e is a factor of 4.7 less than the effective mass reported for Na_xCoO_2 [201]. From this, we can conclude that $K_{0.65}RhO_2$ is relatively less correlated compared to Na_xCoO_2, but more correlated than what was thought earlier [205]. With the help of average Fermi vector (k_F=0.51$\pm$0.02 Å^{-1}) and Fermi velocity, we estimated the Seebeck coefficient using the Boltzmann theory [182, 207], $S = \frac{2\pi^2 k_B^2 T}{3ek_F v_F}$, of 46$\pm$5 μV/K at T=300 K. This value is in excellent agrement with the Seebeck coefficient S_{300K}=46.3 μV/K derived from the transport measurements on $K_{0.63}RhO_2$ [200]. We further verified the validity of Boltzmann theory in the present context by evaluating the Seebeck coefficient for $Na_{0.65}CoO_2$. Considering k_F=0.6 Å^{-1} and averaged v_F=0.275 eV-Å from Ref. [203], we estimated the coefficient S_{300K}=89 μV/K which is in very good agrement with the value of $\approx$ 90 μV/K

obtained from the transport measurements on $Na_{0.67}CoO_2$ [223] and with the value of ≈ 85 μV/K obtained from DFT calculations on $Na_{0.67}CoO_2$ [224]. Thus, the Boltzmann theory is sufficient to understand the enhanced thermoelectric power in these systems.

4.4 Conclusions

In conclusion, we systematically studied the low-energy electronic structure of $K_{0.65}RhO_2$ using ARPES technique and DFT calculations. While we did not observe any topologically protected band dispersions, most importantly we found presence of two *kinks* at the binding energies of 75 and 195 meV below E_F. As demonstrated above the strength of *e-ph* scattering, represented by the coupling constant (λ), strongly depends on the in-plane and out-of-plane momenta. Most importantly, from this study we discover that the high-energy *kink* at 195 meV, leading to anomalous band renormalization near the Fermi level, plays a crucial role in obtaining the colossal thermoelectric power in these systems.

Chapter 5

Electronic, magnetic, and transport studies on AFM-TI, $Mn_{1-x}Sn_xBi_2Te_4$

We investigated the effect of nonmagnetic Sn doping on the electronic and magnetic properties of AFM TI $MnBi_2Te_4$. We observe that the Sn doping reduces out-of-plane AFM interactions in $Mn_{1-x}Sn_xBi_2Te_4$ for up to 68% of Sn concentration and above, the system is found to be a paramagnetic. In this way, the AHE observed at a very high critical field of 7.8 T in $MnBi_2Te_4$ is reduced to 2 T at 68% of Sn doping. Electrical transport measurements suggest that all compositions are metallic in nature, while the low temperature resistivity is sensitive to the AFM ordering and to the doping-induced disorder. Hall effect study demonstrates that Sn actually dopes electrons into the system, thus, enhancing the electron carrier density almost by two orders at 68% of Sn. In contrast, $SnBi_2Te_4$ is found to be a *p*-type metal. ARPES studies show that the topological properties are intact at least up to 55% of Sn doping as the Dirac surface states are present near the Fermi level. But in $SnBi_2Te_4$ we are unable to detect the surface states due to heavy hole doping. Thus, the Sn doping significantly affects the electronic and magnetic properties of $MnBi_2Te_4$.

Results Presented in this chapter are published in Physica B: Condensed Matter 657, 414799 (2023)

5.1 Introduction

Introduction of magnetism into a TI has been known to give rise to various exotic quantum phenomena such as axion [225–227] and Chern insulating states [228–230], Majorana zero modes [231], and Weyl semimetallic phase [7, 57, 232]. However experimental realization of such peculiar systems has been quite challenging due to the lack of intrinsic magnetism in TIs. Earlier, magnetic ordering in the TIs, $(Bi/Sb)_2Te_3$, was achieved by doping with the magnetic ions like Cr/V [228, 229, 233, 234] in order to induce QAH insulating phase. In this way, a ferromagnetic (FM) order is induced to break the TRS in the system. When TRS breaks, the degeneracy of surface Dirac point is lifted and the gap opening is followed by the chiral edge states, responsible for the QAH effect as observed in these systems. However, so far this method showed QAH insulator states at very low temperatures (<1 K) [229, 235].

Interestingly, $MnBi_2Te_4$ was recently discovered to be one of such intrinsic TI with spontaneous AFM order [55, 236–246], in which the layers of ferromagnetically ordered Mn ions are coupled antiferromagnetically along the c-axis. Here, the long range magnetic ordering breaks TRS but the combination of TRS (Θ) and half-lattice translational operator ($T_{1/2}$) connecting the two nearest Mn layers, i.e. $S = \Theta T_{1/2}$ remains protected [240]. As a result, $MnBi_2Te_4$ becomes a potential candidate for hosting intriguing topological properties. It was also found that $MnBi_2Te_4$ thin flakes exhibit axion insulating state for even number of layers [56]. Chern insulating state is noticed for odd number of layers at zero magnetic field [55]. But at much higher magnetic fields even number of layers also show Chern insulating phase [56]. Similar to even number layered thin flakes, bulk $MnBi_2Te_4$ shows magnetization, thus requiring a very high magnetic fields (7.8 T) to obtain the QAH effect [247]. One approach to see QAH effect in $MnBi_2Te_4$ at lower fields is by weakening the interlayer AFM exchange coupling by doping with nonmagnetic ion like Sn at the Mn site.

In this work, we report comprehensively on the effect of Sn doping on the electronic and magnetic properties of the magnetic TI $MnBi_2Te_4$. For this, we studied various single crystals of $Mn_{1-x}Sn_xBi_2Te_4$ with x = 0, 0.2, 0.55, 0.68, 0.86, and 1. We realized that Sn doping has a significant effect on the AFM ordering. That is, we observe a decrease in Néel temperature (T_N) from 24 K for $MnBi_2Te_4$ to 6 K for 68% of Sn doping, while x = 0.86 and 1 are found to be paramagnetic in nature. Further, we observe that the out-of-plane magnetic ordering is intact up to $x = 0.68$, while for in-plane there is a change from

linear M(H) behavior to a very weak ferromagnetic type M(H) curve with a saturated magnetization of 0.8 μ_B/f.u with increasing Sn. We find a cusp on the resistivity data at the Néel temperature, which decreases with increasing Sn up to $x = 0.68$, consistent with magnetic studies. In addition, from $x = 0.55$ and 0.68 compositions, we observe low temperature resistivity upturn due to Sn doping induced disorder. On the other hand, $SnBi_2Te_4$ show Fermi-liquid type resistivity as the disordered is significantly reduced by fully replacing Mn with Sn. We further notice that Sn induces electron carriers into $MnBi_2Te_4$. As a result, the electron carrier concentration increase by two orders at a Sn concentration of 68% compared to $MnBi_2Te_4$. In contrast to $MnBi_2Te_4$, $SnBi_2Te_4$ is found to be a p-type system. The Fermi level shift in the electronic band dispersions observed from ARPES studies on $x = 0.55$ and $x = 1$ single crystals is consistent with carrier concentrations estimated from the Hall measurements. We further notice that the topological properties are intact up to 55% of Sn doping as the surface Dirac states are present in the valance band, while in $SnBi_2Te_4$ we are unable to detect them due to heavy hole doping.

5.2 Experimental details

We synthesized high quality single crystals of $Mn_{1-x}Sn_xBi_2Te_4$ with $x = 0$, 0.2, 0.55, 0.68, 0.86, and 1 using the solid state reaction route [248]. Constituent elements of Mn (99.9%), Sn (99.99%), Bi (99.99%), and Te (99.99%) were taken in stoichiometric ratio, mixed thoroughly in argon atmosphere, and kept in an alumina crucible before sealing it in a quartz ampoule under a vacuum of 10^{-4} mbar. The sealed quartz ampoule was then heated in a chamber furnace up to 900^{o}C at a rate of 150^{o}C/h, and kept at that temperature for 24 h. The ampoule was then cooled at a rate of 2^{o}C/h. The growth temperature of $MnBi_2Te_4$ is 590^{o}C and for $SnBi_2Te_4$ it is 600^{o}C [249]. After the controlled cooling, we performed prolonged annealing within the temperature range of 590^{o}C to 600^{o}C for a maximum of seven days depending on the amount of Sn doping concentration. Finally, the ampoule was quenched in cold water. In this way, we got shiny and plate-like single crystals with a maximum size of 3×3 mm^2.

As grown single crystals were structurally analyzed using the high-resolution X-ray diffractometer (Rigaku smartLab 9 kW) having Cu–K_α radiation. The chemical composition of the crystals were thoroughly examined using energy dispersive X-ray spectroscopy (EDS)

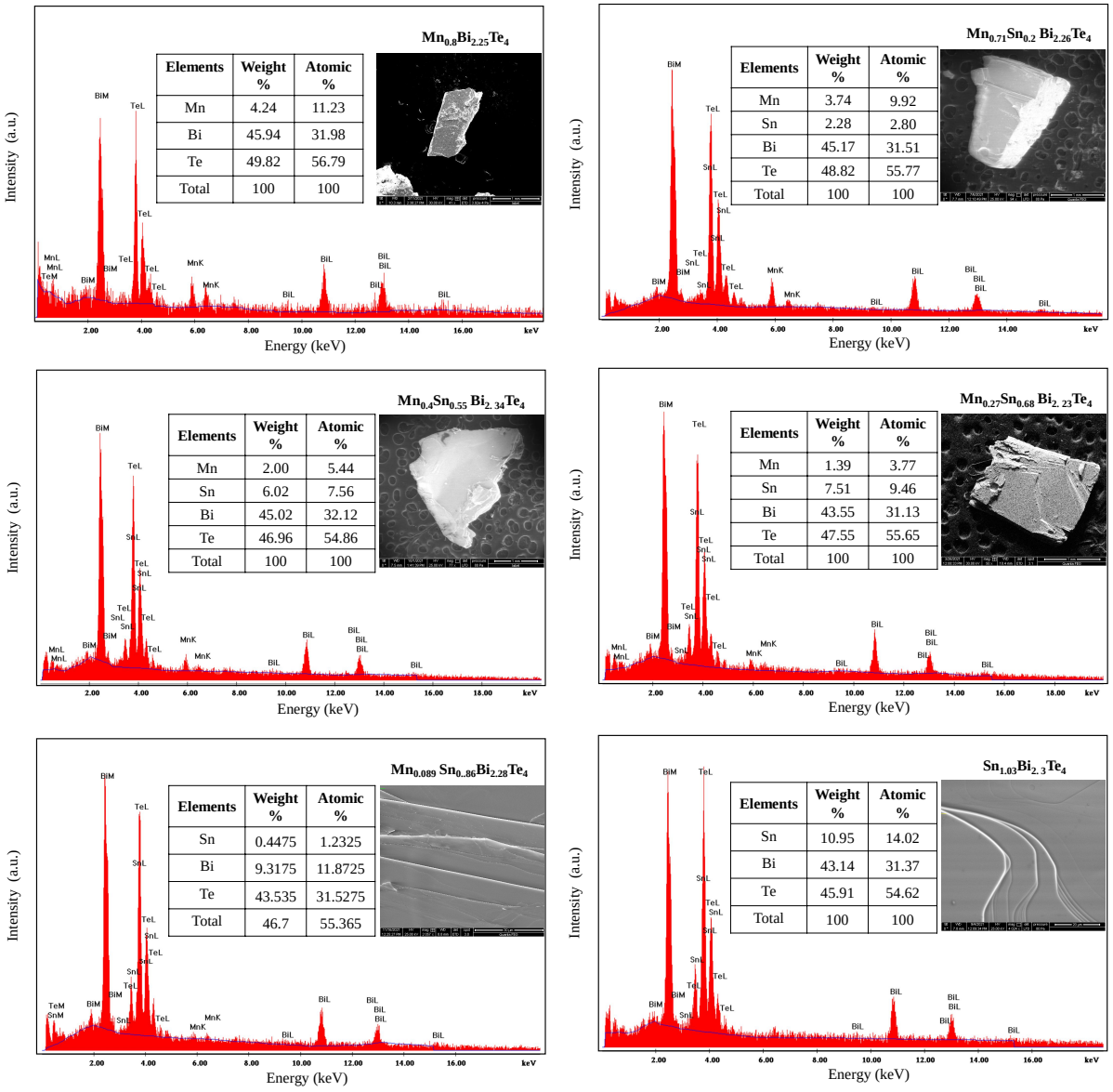

Figure 5.1: Energy dispersive X-ray spectra (EDS) collected from $Mn_{1-x}Sn_xBi_2Te_4$ single crystals from x=0 to x=1

on cleaved sample surfaces [see Fig. 5.1]. For convenience, herein, we will use respective nominal composition to represent each sample. Transport and magnetic properties were measured using Quantum Design Physical Property Measurement System (PPMS) with magnetic field up to 9 T by varying the temperature between 2 and 300 K during the measurements. All magnetic measurements were performed in the DC mode using the VSM option of the PPMS. For ZFC measurements, the sample was cooled down from 300 K to 2 K at zero magnetic field, after which the magnetic field was turned on to collect the

data during heating. For FC measurements, data were collected while cooling the sample in presence of an applied magnetic field. All the transport measurements were carried out in the DC mode with 5000 μA applied current. XPS and ARPES measurements were performed at the undulator based Angle Resolved Photoelectron Spectroscopy beamline (ARPES BL-10), Indus-2, India. All samples were cleaved in-situ in the chamber vacuum of 5×10^{-11} mbar and performed low energy electron diffraction (LEED) measurements using SPECS ErLEED 1000A to examine the sample surface quality. Both the XPS and ARPES measurements were carried out at a sample temperature of 20 K using SPECS Phoibos150 electron analyser. ARPES measurements were performed with a photon energy of hν = 70 eV. The energy and angular resolutions were set at 40 meV and 0.1°, respectively, for the ARPES studies. XPS measurements were performed with a photon energy of hν = 800 eV and at an energy resolution of 0.4 eV.

5.3 Results and discussion

$MnBi_2Te_4$ crystallizes in the rhombohedral structure with a space group of $R\bar{3}m$, consists Te–Bi–Te–Mn–Te–Bi–Te septuple layers as shown in Fig. 7.1(a). Fig. 7.1(b) shows the XRD data of $Mn_{1-x}Sn_xBi_2Te_4$ single crystals for x = 0, 0.2, 0.55, 0.68, 0.86, and 1. XRD data of all crystals show clear reflections from (00l) plane without any impurity peaks. The lower panel in Fig. 7.1(b) shows shift in the (0 0 30) peak to lower 2θ when the (0 0 21) peak position is fixed. This relative peak shift to lower 2θ values signifies a continuous increase in the c lattice parameter with Sn doping. Low energy electron diffraction (LEED) images taken on the freshly cleaved surfaces of x = 0.55 and x = 1 single crystals are shown in Fig. 7.1(e). The LEED pattern of both samples are in hexagonal symmetry with clear first order diffraction spots coming from (001) crystal planes. This is in good agreement with the XRD data, again confirming the high quality of single crystals. XPS data collected on x = 0.55 and x = 1 samples are shown in Figs. 7.1(c) and (d), respectively. Both crystals exhibit major core level peaks at 157.35 eV of Bi $4f_{7/2}$ and 162.75 eV of Bi $4f_{5/2}$, which can be assigned to the Bi^{3+} ions from the Bi–Te bond [250, 251]. Additionally, we noticed two major peaks of Sn $3d_{3/2}$ and Sn $3d_{5/2}$ at 493.3 eV and 484.85 eV, respectively, from Sn^{2+} ions associated to the Sn–Te bond [252]. Te 3d core levels at 582.2 eV (Te $3d_{3/2}$) and 571.85 eV (Te $3d_{5/2}$) corresponding to the Te^{2-} ions from Sn–Te, Mn–Te, and Bi–Te bonds of $Mn_{0.45}Sn_{0.55}Bi_2Te_4$ [253] and also from Sn–Te, and Bi–Te bonds in $SnBi_2Te_4$. The peaks corresponding to Mn^{2+} from Mn–Te

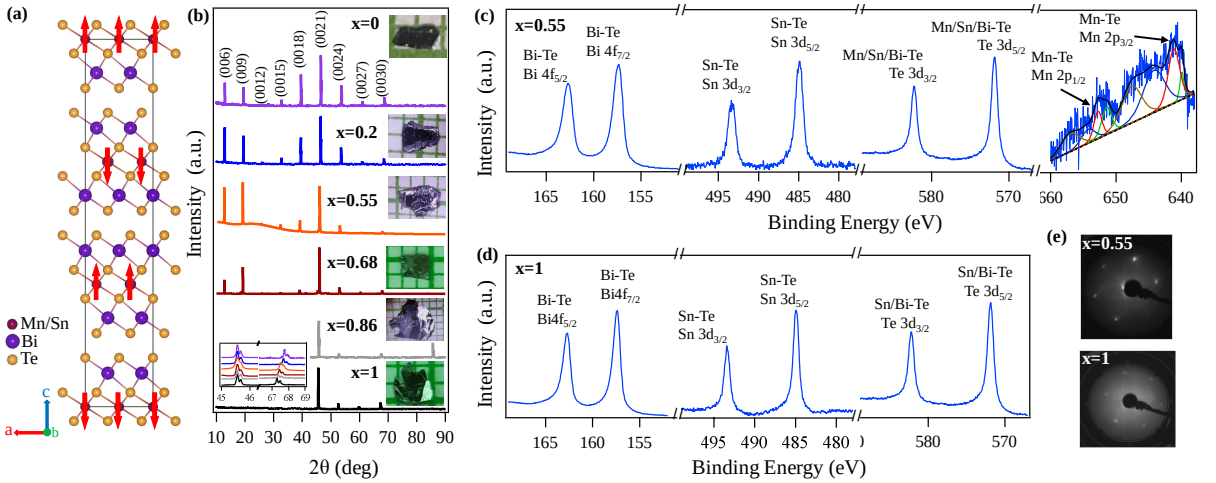

Figure 5.2: (a) Rhombohedral crystal structure of $MnBi_2Te_4$. Red arrows indicate the Mn^{2+} ion spins in AFM state. (b) Single crystal XRD patterns showing $(00l)$ reflections from all the compositions. Insets in (b) show photographic images of $Mn_{1-x}Sn_xBi_2Te_4$ single crystals. Bottom-left inset in (b) shows the zoomed-in XRD pattern demonstrating the shift in (0 0 30) peak position with Sn doping. (c) and (d) Show XPS spectra exhibiting the Bi 4f, Sn 3d, Te 3d, and Mn 2p core levels for $x = 0.55$ and Bi 4f, Te 3d, and Sn 3d core levels for $x = 1$, respectively. (e) Shows LEED data taken with 70 eV photon energy revealing hexagonal pattern for both $x = 0.55$ and $x = 1$ single crystals.

bonds appear at 641.1 eV of Mn $2p_{3/2}$ and 652.8 eV of Mn $2p_{1/2}$ [247, 254]. We further noticed a few low intensity peaks related to Mn^{2+} at 639.9 eV and 651.45 eV of the Mn–O bond as observed in a previous report on this system [247]. $MnBi_2Te_4$ is known to easily get oxidized when exposed to air, making it difficult to handle. As a result of which, we observe minor oxidation peaks of Mn–O bonds caused by the oxidation on the sample surface [247, 254]. However, the bulk physical properties should not be affected by the surface oxidation [247]. In addition, two satellites corresponding to the Mn $2p$ core-levels appear at 647.6 eV and 656.8 eV, and two more satellites corresponding to the Mn–O bonding appear at 644.2 eV and 654.2 eV due to the charge transfer from outer shells of Te $5p$ to the unfilled Mn $3d$ orbitals [253].

To elucidate the effect of Sn doping on the magnetic properties of $MnBi_2Te_4$, we performed thorough magnetic measurements on various Sn doping concentrations. Fig. 7.2(a) depicts field-cooled (FC) and zero-field-cooled (ZFC) magnetic susceptibility (χ) plotted as a function of temperature up to 40 K with magnetic field applied in-plane ($H \parallel ab$) and out-of-plane ($H \parallel c$) orientations. The FC and ZFC curves overlap for all samples, suggesting negligible magnetic hysteresis [255–257]. In agreement with the previous re-

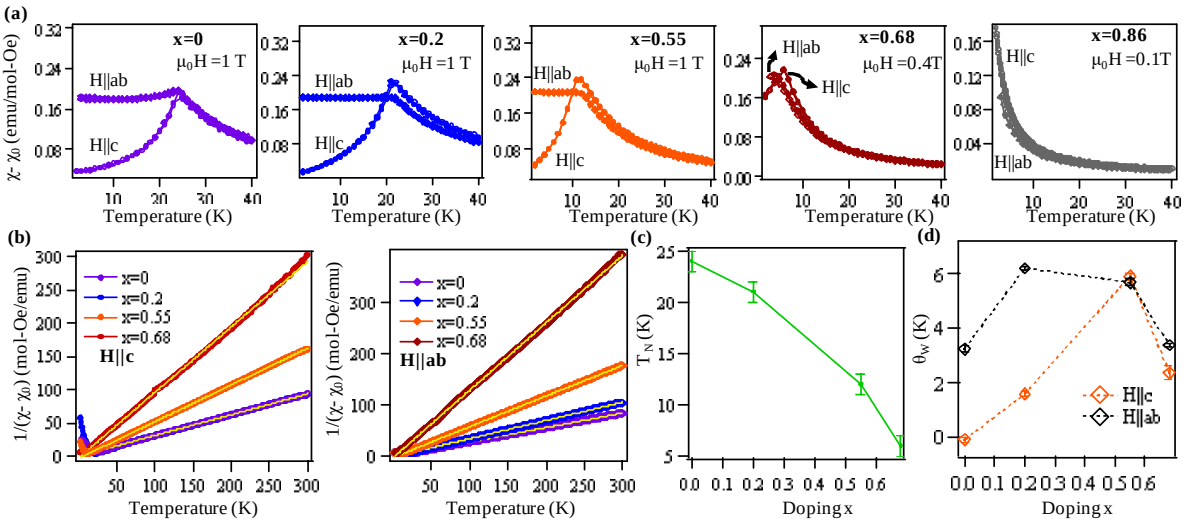

Figure 5.3: (a) Temperature dependent magnetic susceptibility (χ) measured in field-cooled and zero field-cooled modes with H||c and H||ab. (b) Inverse magnetic susceptibility plotted as a function of temperature with H||c and H||ab. Doping dependent (c) Néel temperature (T_N), (d) Curie–Weiss temperature (θ_W) for H||c and H||ab.

ports [239, 241], $MnBi_2Te_4$ shows AFM ordering at a Néel temperature (T_N) of 24 K, thereby causing a sharp decrease in the magnetic susceptibility below T_N for $H \parallel c$, whereas the magnetic susceptibility for $H \parallel ab$ remains almost constant below T_N. Next with increasing Sn substitution in $Mn_{1-x}Sn_xBi_2Te_4$, the 2D ferromagnetic sublattice gets diluted, causing the decrease in T_N linearly from 24 K for $x = 0$ to 6 K for $x = 0.68$ as shown in Fig. 7.2(c). The large decrease in T_N implies a significant weakening of interlayer AFM coupling, while the overall AFM ordering is intact up to 68% of Sn concentration. An earlier magnetic study suggested for a magnetic transition from AFM to paramagnetic for the 66% of Sn doped $Mn_{1-x}Sn_xBi_2Te_4$ [258]. The discrepancy between our study and that of Ref. [258] could be that the low temperature AFM ordering is dominated by the applied magnetic field when measured with 1 T [Fig. 5.4]. Thus, we measured the magnetic data with a field of 0.4 T to see the AFM ordering at 6 K for x = 0.68.

Figure 7.2(b) shows the inverse magnetic susceptibility plotted as a function of temperature with $H \parallel c$ and $H \parallel ab$. From the Curie–Weiss law fitting to the data, we obtained Curie–Weiss temperature (θ_W) for each composition and is plotted in Fig. 7.2(d) as a function of Sn concentration. Earlier reports on $MnBi_2Te_4$ showed positive Curie–Weiss

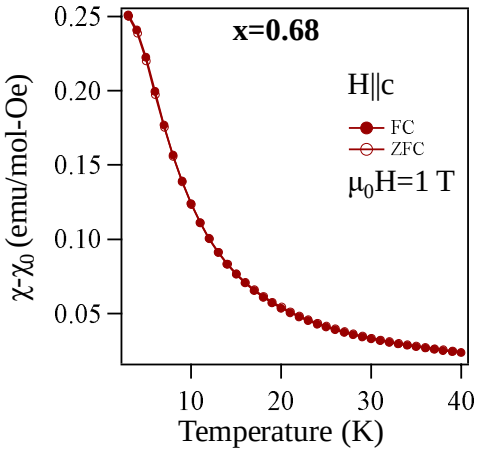

Figure 5.4: Temperature dependent magnetic susceptibility (χ) data measured in both field-cooled (FC) and zero field-cooled (ZFC) mode for $H||c$ from x=0.68

temperature for $H \parallel ab$ due to the in-plane FM exchange interaction and a negative Curie–Weiss temperature for $H \parallel c$ due to the out-of-plane AFM interactions [247]. In agreement to that, we obtained the Curie–Weiss temperatures $\theta_W^c = -0.08$ K and $\theta_W^{ab} = 3$ K. Also, for $H \parallel ab$, we obtained the Curie constant $C = 3.538$ emu-K/mol-Oe and $\chi_0 = -0.00149$ emu/mol-Oe. We calculated the effective magnetic moment $\mu_{eff} = 5.3\ \mu_B$/Mn for $MnBi_2Te_4$ [236, 247] using the formula $C = N_A\mu_{eff}^2/3Nk_B$. By considering the J = 5/2 [236] for Mn^{2+} ions, $\mu_{eff} = 2\sqrt{J(J+1)}\ \mu_B$/Mn = 5.9 μ_B/Mn which is close to the obtained value for $MnBi_2Te_4$. As shown in Fig. 7.2(d), we found different Curie–Weiss temperatures for in-plane (θ_W^{ab}) and out-of-plane (θ_W^c) field directions for the samples $x = 0$ and 0.2, but at higher Sn concentrations both Curie–Weiss temperatures become almost equal due to decreasing magnetic anisotropy with increasing Sn concentration.

Figures 7.3(a)–(e) show field dependent magnetization M(H) isotherms measured with $H \parallel c$ and $H \parallel ab$. The crystallographic c-axis is known to be spin-easy axis for $MnBi_2Te_4$. In agreement to this, Fig. 7.3(a) shows a spin-flop (SF) transition at a critical field of H_c^{SF} = 3.3 T for $H \parallel c$ at 3 K, which gradually decreases to lower fields with increasing temperature up to the Néel temperature. Beyond the Néel temperature, the system transforms to paramagnetic (PM) in nature. During the spin-flop transition, the spin-structure of the system switches from an AFM state to a canted-AFM (CAFM) state, which upon further increase in magnetic field reaches to FM state due to complete polarization of the spins at a critical field of $H_c^{FM} = 7.8$ T for $MnBi_2Te_4$ [259]. With increasing Sn concentration,

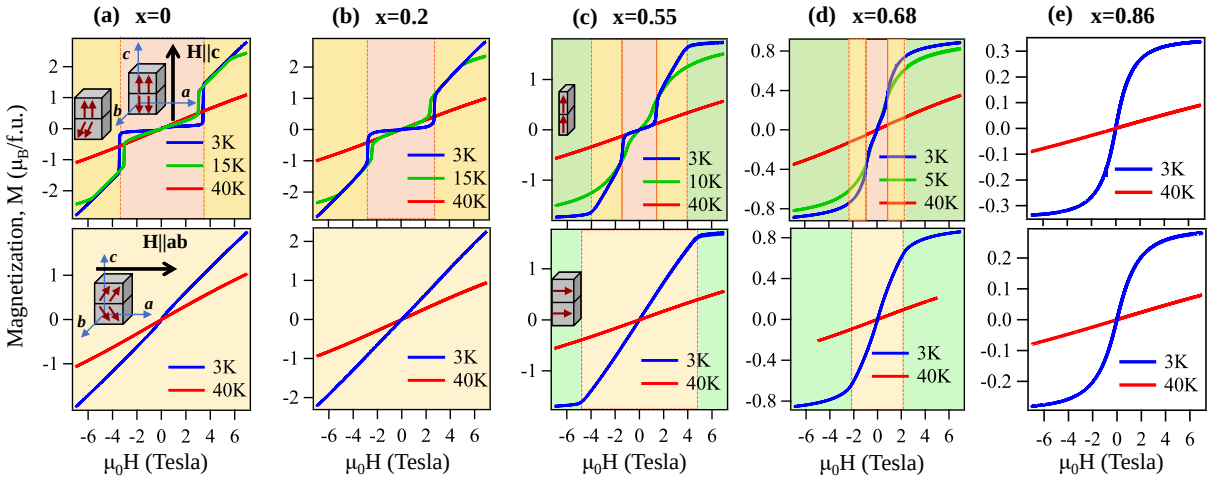

Figure 5.5: Magnetization isotherms taken from (a) $x = 0$, (b) $x = 0.2$, (c) $x = 0.55$, (d) $x = 0.68$, and (e) $x = 0.86$ for the field applied parallel to c-axis (H‖c) (top figure) and parallel to ab-plane (H‖ab) (bottom figure) measured up to 7 T. The insets are schematics representing the Mn spins in their respective color regions for two nearest Mn inter-layers (SLs).

the spin-flop transition critical field decreases for $H \parallel c$. That means, for $x = 0.2$ the critical field of spin-flop transition $H_c^{SF} = 2.5$ T [see Fig. 7.3(b)], which gradually goes down to $H_c^{SF} = 0.7$ T for $x = 0.68$ [see Fig. 7.3(d)]. These observations further support our earlier argument that the AFM transition in $x = 0.68$ sample can be detected only with the magnetic fields below 0.7 T. Further increase in Sn concentration to $x = 0.86$, the spin-flop transition is completely disappeared and the system turns to be a very weak ferromagnet as it shows a sigmoid-like M(H) isotherm at 3 K for $H \parallel c$ [see Fig. 7.3(e)].

Increase in Sn concentration not only decreases the spin-flop critical fields [H_c^{SF}], but also the saturation magnetization (M_S). $MnBi_2Te_4$ is known to show a saturation magnetization of 3.56 μ_B/f.u. at 8 T for $H \parallel c$ [259], it goes down to a negligible saturation magnetization of 0.32 μ_B/f.u for $x = 0.86$. In fact at 3 K, we notice magnetization saturation at 4 T for $x = 0.55$ and at 2.2 T for $x = 0.68$ due to weak FM ordering induced with Sn doping. On the other hand, for $H \parallel ab$, the magnetization M(H) isotherms of $x = 0$, 0.2, and 0.55 show linear dependents on H due to gradual polarization of spins towards the applied field direction. However, the magnetic saturation is noticed for $x = 0.55$ at around 5 T. Interestingly, for $x = 0.68$ and 0.86 the nature of the M(H) curves at lower fields resembles to a weak ferromagnet with sigmoid-like shape and magnetic saturation is around 2 T. These observations suggest that Sn doping into $MnBi_2Te_4$ transforms the system to a weak ferromagnet.

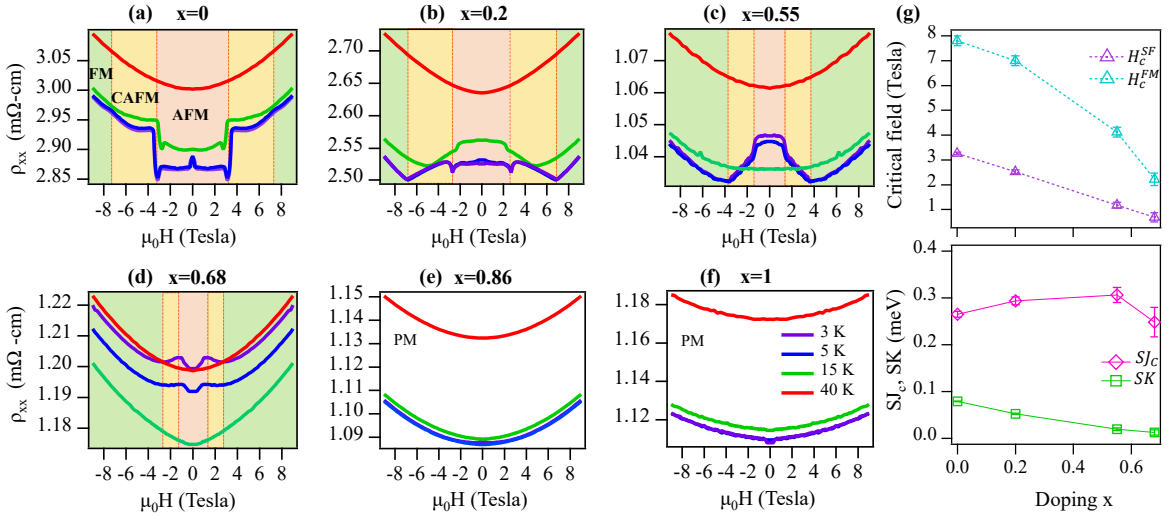

Figure 5.6: Field dependent magnetoresistance (ρ_{xx}) from (a) $x = 0$, (b) $x = 0.2$, (c) $x = 0.55$, (d) $x = 0.68$, (e) $x = 0.86$, and (f) $x = 1$ measured at 3 K, 5 K. 15 K, and 40 K. Top panel in (g) shows doping dependent critical fields of spin-flop transition (H_c^{SF}) and ferromagnetic moment saturation (H_c^{FM}). Bottom panel in (g) shows calculated effective interlayer coupling (SJ_c) and effective single ion anisotropy (SK) between two Mn layers plotted as a function of Sn doping.

Next, field dependent magnetoresistance (MR) up to 9 T measured at various temperatures from all the compositions is plotted in Figs. 5.6(a)–(f). During the measurements, the magnetic field was applied along the c-axis (the easy axis) with current applied parallel to ab-plane. $\rho_{xx}(H)$ of $MnBi_2Te_4$ and all other compositions show negligible variation in the AFM state. This is because the spin scattering induced by AFM ordering could be dominating the Lorentz effect [239]. However, as the field reaches above H_c^{SF} (CAFM), the canted spins start to align along the c-axis. Therefore, the scattering rates start to decrease to lower the MR. Although the samples from x = 0.2 to 0.68 show decrease in MR with increasing field in the CAFM state, in contrast, we do not observe decrease in MR with increasing field in $MnBi_2Te_4$ in the CAFM state [see Fig. 5.6(a)], possibly due to the topological Hall effect which we will discuss later. Furthermore, the critical fields found from MR data are matching very well with that of H_c^{SF} and H_c^{FM} from the M(H) data. We notice that the field dependent MR behavior is consistent with M(H) data up to Néel temperature, and above T_N we observe a parabolic field dependent MR, in agreement with an earlier report [260]. Similar parabolic behavior is present above ferromagnetic saturation H_c^{FM} for lower temperatures (3 and 5 K) due to Lorentz effect. Additionally, we observe a sharp upward jump at the spin flop transition for $MnBi_2Te_4$. Although quite suppressed, similar transition is present in $x = 0.2$. This behavior has

been previously reported in $Mn(Sb_xBi_{1-x})_2Te_4$ for $x = 0.25$ [257]. Here the magnetic coupling mechanism present in the vicinity of the Fermi level was held responsible. As discussed later in Fig. 5.8(g) $x = 0$ and 0.2 have lower $n-$type carrier density, hence the Fermi level is closer to the band gap. This might be the reason why we observe similar upward jump in both of the samples. Next, $x = 0.86$ and 1 ($SnBi_2Te_4$) show parabolic field dependent MR at all the measured sample temperatures due to their paramagnetic nature [see Figs. 5.6(e) and (f)]

The doping dependence of critical fields is shown in Fig. 5.6(g). Both H_c^{SF} and H_c^{FM} decrease monotonically with increasing Sn concentration. Using the values of H_c^{SF} and H_c^{FM}, we obtained the effective interlayer coupling (SJ_c) and effective single ion anisotropy (SK) by $SK = \frac{g\mu_B}{2}\frac{H_c^{SF\,2}}{H_c^{FM}}$ and $SJ_c = \frac{g\mu_B}{4\delta}(H_c^{FM} + \frac{H_c^{SF\,2}}{H_c^{FM}})$ [259, 261]. Here g is the Landé g-factor and δ is the fraction of Mn ions per Mn site. The obtained value of SJ_c and SK are plotted in the lower panel of Fig. 5.6(g). While SK monotonically decreases with increasing x due to reduction of Mn ions, we see a very little change in SJ_c. That means, ingoing from $x = 0$ to $x = 0.68$ SJ_c changes little from 0.27 meV to 0.25 meV, while SK decreases significantly from 0.79 meV to 0.13 meV. The negligible change in the effective interlayer coupling (SJ_c) can be understood from the XRD data shown in Fig. 7.1(b) which shows a very little shift in the $(00l)$ plane with doping, demonstrating nearly constant c parameter.

Temperature dependent stacked in-plane resistivity (ρ_{xx}) data are plotted in Fig. 5.7(a). ρ_{xx} of all compositions suggest an overall metallic behavior. From the normalized resistance shown in Fig. 5.7(b) we notice a cusp at around 24 K from $x = 0$, 21 K from $x = 0.2$, 10 K from $x = 0.55$, and 5 K from $x = 0.68$ due to the spin-fluctuations triggered around Néel temperature. In addition, compositions of $x = 0.55$ and $x = 0.68$ show upturn resistivity with minima at 15 K and at 28 K, respectively. Note here that these temperature minima are higher than their respective Néel temperatures, suggesting rather a different mechanism for increasing resistivity at low temperatures such as the disorder induced electron–electron ($e - e$) interactions [262], weak localization (WL) [263], or the Kondo effect [264]. In order to explore further on the origin of resistivity upturn, we performed field dependent resistivity on $x = 0.68$ and plotted the data as shown in Fig. 5.7(c). From Fig. 5.7(c) we can see that up to 9 T the resistivity upturn does not suppress, contradicting to the possibility of Kondo effect or weak localization in which cases usually the resistivity upturn suppresses [264]. Thus, low temperature resistivity upturn found from the $x = 0.55$ and 0.68 compositions could have originated from the disorder induced $e - e$

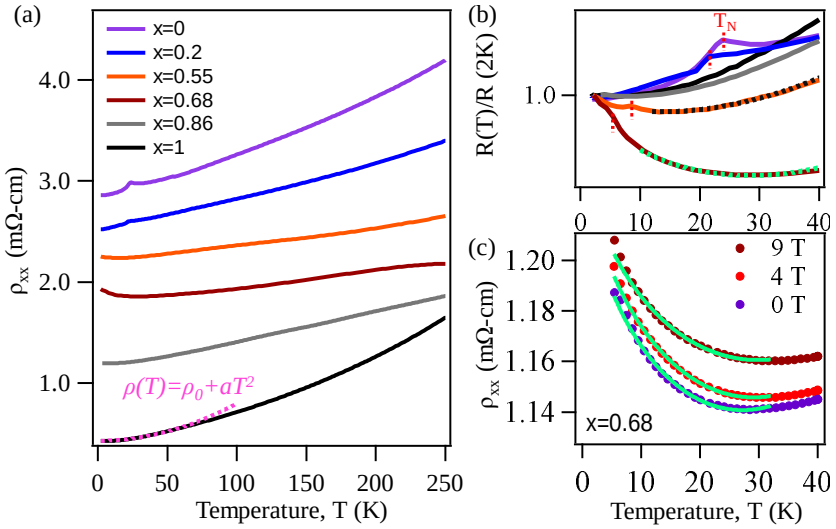

Figure 5.7: (a) Stacked in-plane resistivity ρ_{xx} plotted as a function of temperature from all the compositions. (b) Normalized in-plane resistance (R(T)/R(2 K)) plotted at low temperatures. (c) $\rho_{xx}(T)$ of $x = 0.68$, measured with 0 T, 4 T, and 9 T applied magnetic fields for $H \parallel c$. The dashed curves (b) and the solid curves in (c) are the fits to $e-e$ scattering equation.

scattering with Sn doping [262, 265, 266]. To confirm this, we did fit the low temperature resistivity upturn using the relation of e-e scattering, $\rho = \rho_0 - \alpha T^{1/2} + \beta T^2$ [see Figs. 5.7(b,c)]. The term $\alpha T^{1/2}$ represents e-e elastic scattering and the term βT^2 represents the e-e inelastic scattering (Fermi-liquid type) [267]. Similarly, we could fit the resistivity upturn of x = 0.55 [Fig. 5.7(b)] with the same consideration. Nevertheless, the resistivity upturn is absent from $SnBi_2Te_4$ and rather we find a clean Fermi-liquid type resistivity curve that is satisfying the T^2 law.

Field dependent Hall resistivity (ρ_{xy}) data at 3, 5, 15, and 40 K for all compositions are shown in Fig. 5.8. As can be seen from Figs. 5.8(a)–(f), the ρ_{xy}(H) decreases with increasing Sn concentration up to $x = 0.68$ and then the slope reverses for $x = 1$ ($SnBi_2Te_4$) as shown in Fig. 5.8(f). The change in slope of ρ_{xy}(H) clearly hints at increase in electron carrier concentration up to $x = 0.68$ which then becomes p-type for $x = 1$. Further, from a closer look at the Hall data of $MnBi_2Te_4$, we can notice a change in slope at the spin-flop critical field of $H_c^{SF} = 3.2$ T and at the ferromagnetic ordering field of $H_c^{FM} = 7.8$ T. The total Hall resistivity ($\rho_{xy}(H)$) can be expressed by $\rho_{xy}(H) = R_0\mu_0 H + \rho_{xy}^A$. Here, the term $R_0\mu_0 H$ represents ordinary Hall resistivity (OHR) and the term ρ_{xy}^A represents anomalous Hall resistivity (AHR). To extract the anomalous Hall resistivity (ρ_{xy}^A) for the compositions

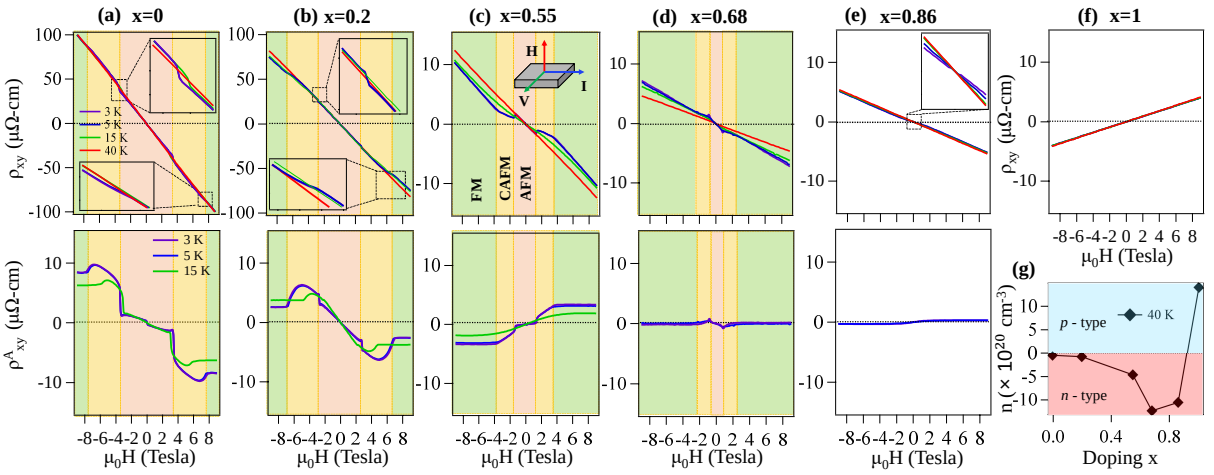

Figure 5.8: (a)–(f) Field dependent Hall resistivity (ρ_{xy}) measured at 3, 5, 15, and 40 K. (red, yellow, green, and white colored regions in (a)–(d) represents AFM, CAFM, FM, and PM states of the system, respectively). The lower panels of (a)–(e) shows the anomalous Hall resistivity (ρ^A_{xy}) obtained after subtracting the normal Hall resistivity from ρ_{xy}. (g) Charge carrier density (n) plotted as a function of Sn doping concentration.

$x = 0$ to 0.86, we subtracted the ordinary Hall contribution from total Hall resistivity by linearly fitting $\rho_{xy}(H)$ at higher-field region. The resultant ρ^A_{xy} is plotted as a function of field in the bottom panel of Figs. 5.8(a)–(e). The slope changes at H_c^{SF} and H_c^{FM} are very prominent in the obtained ρ^A_{xy}. Moreover, ρ^A_{xy} of $MnBi_2Te_4$ exhibits almost linear field dependence in the AFM region, consistent with the $M(H)$ data [see Fig. 7.3(a)]. But interestingly, we clearly observe a cusp in ρ^A_{xy} of $MnBi_2Te_4$ in the CAFM region [55, 261]. Similar behavior is also observed from $x = 0.2$. We suggest, the cusp in the AHR possibly originated from the topological Hall effect due to non-collinear spin-structure [268] in the CAFM state which dissipates with increasing Sn doping concentration. Further, both $x = 0$ and $x = 0.2$ have negative anomalous Hall resistivity above H_c^{FM} which switches to positive ρ^A_{xy} for $x = 0.55$ and remains positive for $x = 0.68$ and $x = 0.86$ when measured at 3 K. Similar behavior has previously been observed in $Mn_{1-x}Pb_xBi_2Te_4$ for $x = 0.53$ [261]. These observations suggests that replacing 50% of Mn in $MnBi_2Te_4$ with nonmagnetic ions changes the band structure near Fermi level, leading to sign reversal at the higher fields in ρ^A_{xy}. However, we observe negligible ρ^A_{xy} from $x = 0.68$ and $x = 0.86$ as they are already at the verge of paramagnetic to possess significant AHE [see Figs. 7.2(a) and (e)].

Next, the charge carrier concentration has been estimated from the Hall data and plotted in Fig. 5.8(g) for all the compositions at 40 K. We find an electron carrier density of 5.4×10^{19} cm^{-3} for $x = 0$, 8.18×10^{19} cm^{-3} for $x = 0.2$, 4.59×10^{20} cm^{-3} for $x = 0.55$,

1.2×10^{21} cm^{-3} for $x = 0.68$, and 1.04×10^{21} cm^{-3} for $x = 0.86$ from the linear Hall resistivity data collected at 40 K, where all samples become paramagnets [269]. Thus, in going from $x = 0$ to $x = 0.68$ the electron carrier density increased by an order of 2. On the other hand, for $x = 1$ ($SnBi_2Te_4$) we estimated a hole carrier density of 1.39×10^{21}cm^{-3}, in good agreement with previous reports on the hole carrier concentration of $SnBi_2Te_4$ [270–272]. Further, our observation of increase in electron density with Sn doping is in good agreement with a previous report [258].

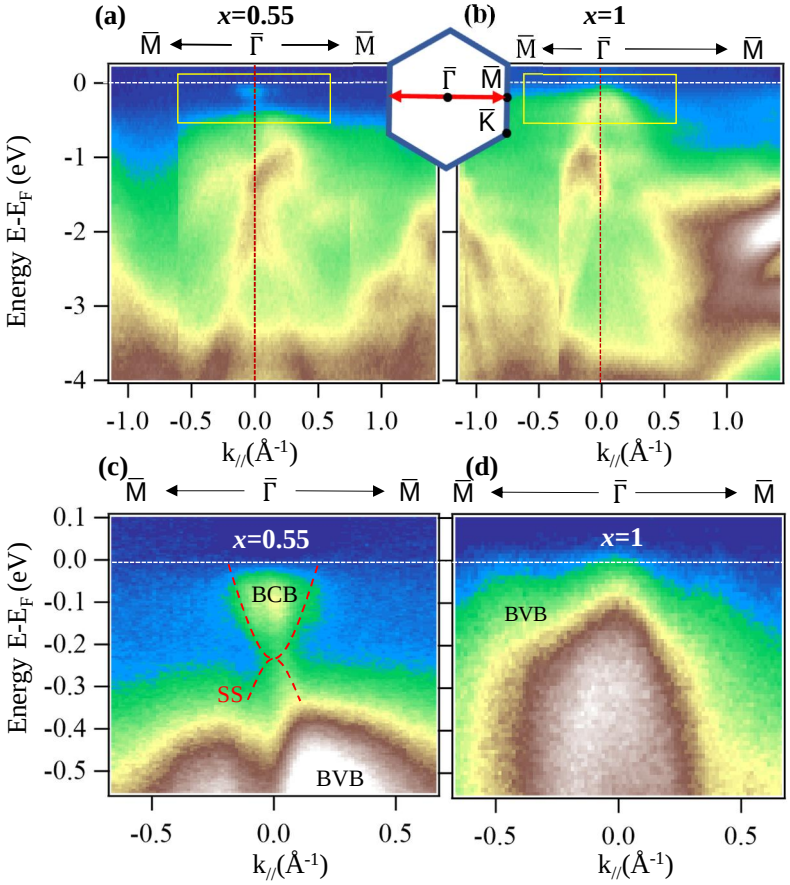

Figure 5.9: (a) and (b) Energy distribution maps (EDMs) from $x = 0.55$ and $x = 1$ compositions, respectively, taken along $\overline{\Gamma} - \overline{M}$ direction with 70 eV photon energy using linearly polarized light. (c) and (d) are the zoomed-in EDMs of $x = 0.55$ and $x = 1$ near E_F. In the figure, BCB and BVB stand for bulk conduction and valance bands, respectively. SS stands for surface states.

In order to understand the effect of Sn doping on the electronic band dispersions near the Fermi level, we performed ARPES measurements on $x = 0.55$ and $x = 1$ compositions as shown in Fig. 5.9 measured with 70 eV photon energy of linearly polarized light. Figs. 5.9(a) and (b) depict energy distribution maps (EDMs) plotted for $x = 0.55$ and

x = 1, respectively, along $\overline{\Gamma} - \overline{M}$ orientation as schematically shown in the inset. Fig. 5.9(c) and (d) depict zoomed-in images of Figs. 5.9(a) and (b), respectively, showing band dispersions near the Fermi level. From Fig. 5.9(c), we can notice that the surface Dirac state in $x = 0.55$ is connecting the bulk conduction band (BCB) and bulk valence band (BVB) like in the parent $MnBi_2Te_4$ [273–275]. However, the surface Dirac states are completely disappeared when Mn is totally replaced by Sn [see Fig. 5.9(d)]. In addition, we find that the bulk valance band in $x = 1$ shifted closer to the Fermi level while the bulk conduction band shifted above the Fermi level due to Fermi level shifting towards higher binding energy with hole doping. This is in good agreement with the dominant hole carrier density estimated from the Hall measurements in the case of $SnBi_2Te_4$.

Despite $MnBi_2Te_4$ being TI with intrinsic magnetic ordering, there are mainly two obstacles on the path of realizing Chern insulating state in this system. One of them is the high magnetic fields needed to obtain FM order [273] and the other one is the dominant bulk electron carriers induced by the excess Bi and the antisite defects in single crystals [257], shifting the Fermi level into the bulk conduction band. Doping Sn at the Mn site appeared to be a promising technique for suppressing the n-type bulk carriers as $SnBi_2Te_4$ is isostructural to $MnBi_2Te_4$ and has high $p-$type carrier concentration [271]. But the magnetism, an important ingredient to realize the Chern insulating state, seems to be disappearing beyond 68% of Sn doping while still the electron carriers dominating the transport. On the other hand, when the electron density decreased at higher Sn doping ($x = 0.86$) the system turns into nonmagnetic [see Fig. 5.8].

5.4 Conclusions

In conclusion, we have successfully grown high quality single crystals of $Mn_{1-x}Sn_xBi_2Te_4$ (x = 0, 0.2, 0.55, 0.68, 0.86 and 1). We noticed that Sn doping in $MnBi_2Te_4$ is an effective way of acquiring quantum Hall state at lower magnetic fields as the critical field of FM ordering goes from 7.8 T to 2.2 T in going from x = 0 to x = 0.68. Electrical resistivity is found to be sensitive to the AFM ordering temperature (T_N), but with Sn doping the low temperature resistivity shows upturn due to the doping induced disorder. However, low temperature upturn is absent in $SnBi_2Te_4$ as the disorder is reduced. Hall effect study shows electron doping into the system with Sn, and thus, enhancing the electron carrier density almost by two orders with 68% of Sn concentration. In contrast,

$SnBi_2Te_4$ is found to be a *p*-type system. ARPES studies show that topological properties are intact up to 55% of Sn doping in $MnBi_2Te_4$, but the Dirac surface states disappear when Mn is completely replaced by Sn ($SnBi_2Te_4$). Thus, our studies presented here clearly demonstrate the effect of Sn doping on the electronic and magnetic properties of $MnBi_2Te_4$.

Chapter 6

ARPES studies on 3D-TI Bi_2Se_3 in the presence of magnetic impurities

As magnetic ordering in TIs can break the TRS, the TIs are predicted to open up a band gap at the Dirac point in the presence of magnetic impurities. To experimentally observe the effect of magnetic impurities on the electronic structure, we have performed high-resolution ARPES experiments on 3D TI Bi_2Se_3 along with various magnetically doped compounds such as $Co_{0.1}Bi_2Se_3$, $Mn_{0.1}Bi_2Se_3$, and $Eu_{0.1}Bi_{1.9}Se_3$. Though no band gap opening at the Dirac point was observed due to very small amount of doping, a clear shift of the Dirac point to higher binding energy was observed. Our measurements show the presence of conducting surface and insulating bulk states for all the compounds and also indicate that all the magnetic elements we doped in Bi_2Se_3 provide additional electrons to the compound, which eventually causes a shift of the Dirac point.

Results Presented in this chapter are published in AIP Conference Proceedings 2265, 030355 (2020)

6.1 Introduction

Unlike normal insulators, TIs are a class of quantum materials which have insulating bulk states and conducting surface states. Interestingly, the metallic surface state is robust to all the disorder potential, which does not break the TRS [3, 40, 54, 276]. These unusual properties of TIs not only help to have a better understanding of quantum materials in physics but also have a very promising future in quantum information processing. After the observation of topological properties in HgTe [2, 38], a number of compounds were proposed to have the topological properties [4, 277–281]. Recently Bi_2Se_3, Bi_2Te_3, and a few other compounds were identified to be 3D TIs [43, 44, 282]. Bi_2Se_3, like other 3D TIs, has a Dirac cone in the surface state and a large band gap in the bulk [4]. To open up a gap at the Dirac point, either the TRS or the inversion symmetry needs to be broken. One way to break the TRS is by introducing magnetic impurities [283]. From theoretical calculations, it has been shown that the presence of magnetic impurities causes gap opening at the Dirac point and introduces ferromagnetic ordering in the TSS by Ruderman-Kittel-Kasuya-Yosida (RKKY) interaction [46]. To investigate the effect of magnetic impurities on the electronic structure of 3D TI B_2Se_3, here we have performed ARPES measurements on $Co_{0.1}Bi_2Se_3$, $Mn_{0.1}Bi_2Se_3$, and $Eu_{0.1}Bi_{1.9}Se_3$, along with pure Bi_2Se_3 single crystal.

6.2 Experimental details

Single crystals of Bi_2Se_3, the Co and Mn intercalated crystals, $Co_{0.1}Bi_2Se_3$, $Mn_{0.1}Bi_2Se_3$, and Eu doped $Eu_{0.1}Bi_{1.9}Se_3$, were grown by self-flux method [284–286], where the stoichiometric mixture of all the elements were mixed and heated at 950^o C and slowly cooled down to 650^{o}C. To perform the ARPES measurements, the samples were cleaved in-situ in the preparation chamber having vacuum of the order of 1×10^{-10} and then moved to the measurement chamber, where the measurements were done using He-Iα (hν=21.2 eV) lamp under high vacuum (9×10^{-11} mbar) at a constant temperature of 15K with energy resolution of 10 meV.

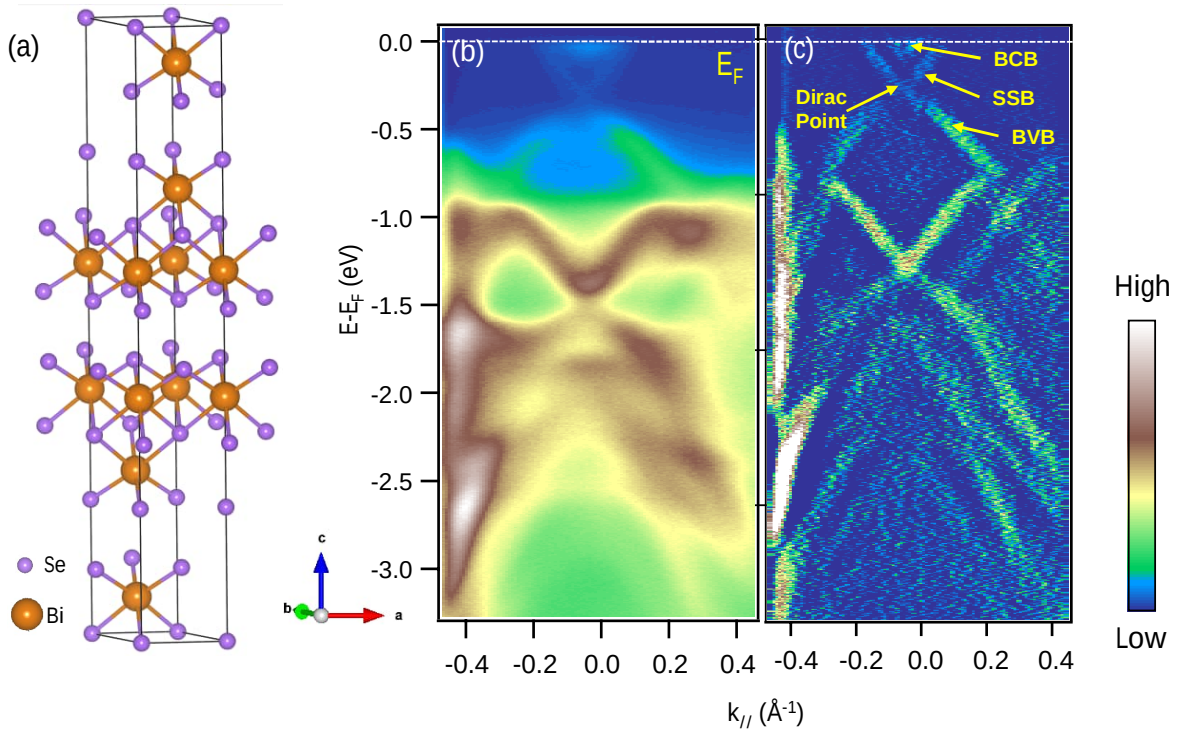

Figure 6.1: (a) Rhombohedral crystal structure of Bi_2Se_3.(b) Large energy range scan for Bi_2Se_3, obtained from ARPES.(c) observation of bulk conduction band (BCB), bulk valence band (BVB), surface-state band (SSB) and the Dirac point from the second derivative w.r.t. $k_{//}$ (Å) near the Fermi level.

6.3 Results and discussions

Figure 1(a) shows the crystal structure of Bi_2Se_3, where we can see the presence of Bi-Se layers within the triangle lattice. Bi_2Se_3 contains rhombohedral crystal structure with space group D^5_{3d} ($R\bar{3}m$). The structure of Bi_2Se_3 is consisted of quintuple layers, which are actually five layers in the sequence of Se-Bi-Se-Bi-Se [287]. Two neighboring quintuple layers are weakly bonded by van der Waals bond. So, when an element is intercalated, the atoms enter the van der Waals gap of the crystal [288] and form a layer that changes the electronic band structure of the crystal. To investigate the variations, we measured the band structures of Bi_2Se_3 intercalated with magnetic Co, Mn, and Eu along with pure Bi_2Se_3 single crystals by ARPES. Figure 1(b) shows the ARPES intensity plot for undoped Bi_2Se_3. From the energy distribution map and its second derivative [Fig: 1(c)], we observe a bulk band gap of 225 meV between the bulk conduction band (BCB) and the bulk valence band (BVB). As Bi_2Se_3 is a TI, the presence of a topologically protected

conducting surface state band (SSB) and the Dirac point is also clearly visible in Fig: 1(c) [41].

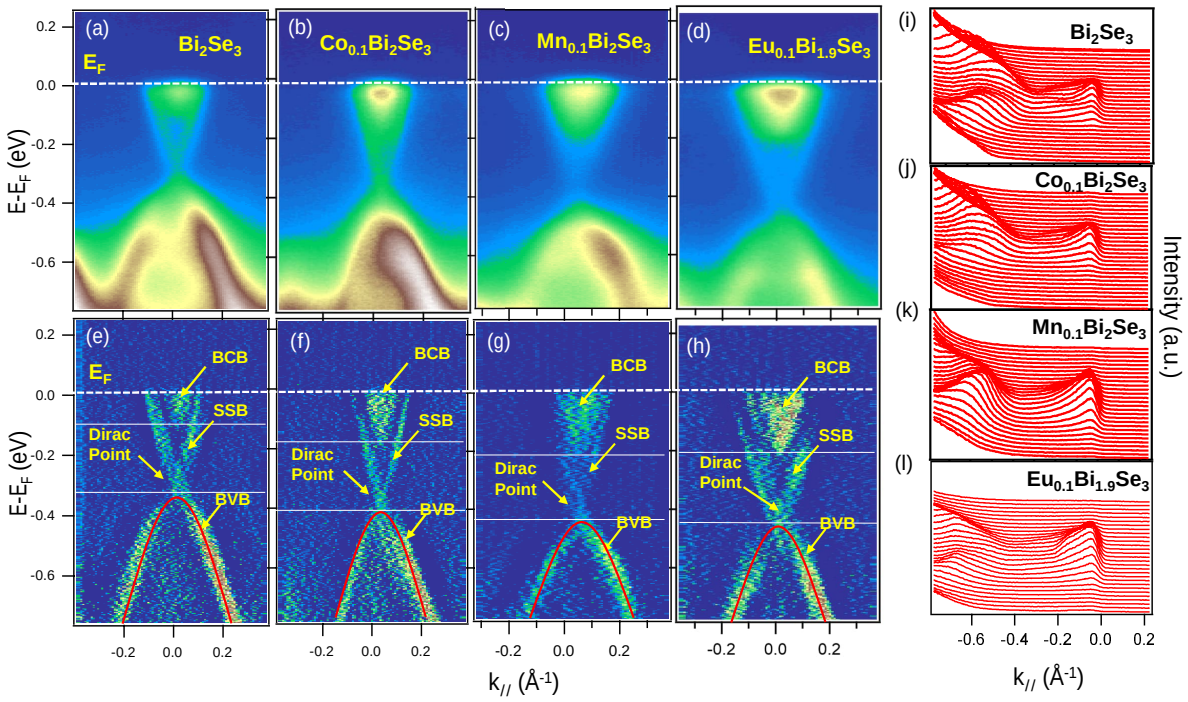

Figure 6.2: Change in band structures in ARPES plots with the change in doped/intercalated elements. (a)-(d) EDMs measured from ARPES of Bi_2Se_3, and the intercalated Bi_2Se_3 ($Co_{0.1}Bi_2Se_3$, $Mn_{0.1}Bi_2Se_3$, and $Eu_{0.1}Bi_{1.9}Se_3$). (e)-(d) Second derivatives of (a)-(d) w.r.t. $k_{//}$ showing the Dirac point shift and change in bulk band gap for different intercalation. (i)-(l) EDCs for all the EDMs from (a)-(d).

Figure 2 shows the ARPES spectra of parent compound Bi_2Se_3 along with $Co_{0.1}Bi_2Se_3$, $Mn_{0.1}Bi_2Se_3$, and $Eu_{0.1}Bi_{1.9}Se_3$ (Figs. 2(a)-(d)). From Figs. 2(e)(f) and the EDCs of the ARPES plots (Figs. 2(i)-(1)), we can see the clear presence of conducting surface states (i.e., no band gap opening at the Dirac point) in all the intercalated samples and so in the doped samples. But the bulk band gap between BVB and BCB changes when the magnetic materials are deposited. The bulk band gap of 225 meV was observed for Bi_2Se_3 (Fig. 2(e)), which decreases to 219 meV and 206 meV with the intercalation of Co and Mn respectively (Figs. 2(f)-(g)). But for doping of lanthanide element Eu, the bulk band gap increases to 247 meV (Fig. 2(h)). Besides the change in the bulk band gap, the Dirac point also shifts downward in the doped samples. The Dirac point shifts 75 meV for Co intercalation, which increases to 99 meV when Mn intercalation and 138 meV for Eu doping (Figs. 2(f)-(h)).

6.4 Conclusions

In conclusion, we discussed the ARPES data of Bi_2Se_3, $Co_{0.1}Bi_2Se_3$, $Mn_{0.1}Bi_2Se_3$, and $Eu_{0.1}Bi_{1.9}Se_3$. Theoretically, it has been predicted that the presence of magnetic impurities breaks the TRS of TIS and opens up a band gap in the surface state [17]. But in the measured compounds, the percentage of magnetic impurities are only 10%, which is very low. As a result, the topological properties of Bi_2Se_3 are unaffected. Though there is no band opening due to doping, the Dirac point shifts to higher binding energies with the intercalation of Co, Mn, and Eu. The dopants induct electrons into the system. And more electron doping causes more shift to the Dirac point, which signifies that Mn donates more electrons to the samples than Co. The Dirac point shift is the most for Eu doping, which means that Eu provides much more electrons to Bi_2Se_3 than Co or Mn.

Chapter 7

Electronic Band Structure Studies of Magnetic WSM, Mn_3Ge

Using ARPES and DFT calculations, we systematically studied the electronic band structure of Mn_3Ge in the vicinity of the Fermi level. We observe several bands crossing the Fermi level, confirming the metallic nature of the studied system. We further observe several flat bands along various high symmetry directions, consistent with the DFT calculations. The calculated partial density of states (PDOS) suggests a dominant Mn $3d$ orbital contribution to the total valence band DOS. With the help of orbital-resolved band structure calculations, we qualitatively identify the orbital information of the experimentally obtained band dispersions. Out-of-plane electronic band dispersions are explored by measuring the ARPES data at various photon energies. Importantly, our study suggests relatively weaker electronic correlations in Mn_3Ge compared to Mn_3Sn.

Results presented in this chapter are communicated to an international journal for publication (under review).

7.1 Introduction

The coexistence of magnetism and topology in magnetic semimetals manifests several intriguing quantum materials in the condensed matter such as the WSMs [289–292]. Mn_3Ge is one such magnetic WSM from the family of Mn_3X (X= Sn & Ge) kagome systems, with noncollinear AFM order, demonstrating exotic electronic properties like giant AHE [293–296], anomalous Nernst effect [297–301], Kerr effect [302–304], and flat bands along with Weyl nodes near the Fermi level [305, 306], leading to compelling quantum technological application [307, 308]. Usually, the Weyl points are manifested either by the broken TRS or by the broken inversion symmetry. Out of these two categories, the TRS broken systems are in principle magnetic WSMs which also host strong electronic correlations [309–311], exhibiting several fascinating bulk electronic and magnetic properties. On the other hand, in the case of the Mn_3X family of materials, it is the translational plus TRS breaking that gives rise to the Weyl physics [300, 306, 312, 313]. The Weyl system can host a minimum of two pairs of Weyl nodes. Each pair of Weyl nodes with opposite chirality acts as the source and sink of the Berry curvature, leading to large AHE [293, 294, 314, 315]. Thus, a systematic study of the low-energy electronic band structure of these systems is crucial for understanding the observed large AHE.

Although there exist many DFT calculations exploring the topological properties of Mn_3X (X=Sn & Ge) systems by studying their electronic band structure near the Fermi level [7, 316, 317], so far only one ARPES report is available experimentally demonstrating the electronic band structure of Mn_3Sn [7]. The DFT calculations predict several Weyl points near the Fermi level from both Mn_3Sn and Mn_3Ge. However, experimentally, it is hard to detect these Weyl points due to difficulties in resolving the valence band electronic structure. Because of this complexity, not much excitement is generated in the research community for experimentally studying the electronic band structure of these very fascinating magnetic topological WSMs.

In this manuscript, we present the low-energy electronic band structure of Mn_3Ge studied by using the ARPES technique and compared it with the calculated band structure using DFT. We find a qualitative agreement between the ARPES data and DFT calculations. However, detection of the theoretically predicted Weyl points from our ARPES data has been quite challenging as they are predicted well above the Fermi level [305, 306]. Since Mn_3X compounds are suggested to show strong electronic correlations [7, 318], instead of searching for the Weyl points, we focused on the details of low-energy electronic band

structure along the in-plane ($k_{//}$) and the out-of-plane (k_z) orientations. The partial density of state (PDOS) calculations confirm the presence of dominant Mn 3d orbital characters near the Fermi level. We further carried out the orbital-resolved DFT calculations and compared them with the ARPES data to understand the orbital contributions to the experimental electronic band structure. In addition, as the Mn_3Ge is constructed from layered kagome lattice, these are predicted to host flat bands [319–321]. Our ARPES data demonstrate the presence of such flat bands along different high-symmetry directions of the BZ.

7.2 Experimental Details

Mn_3Ge single crystals were grown by the melt-growth method [293]. To grow the crystals, stoichiometric amounts of high quality Mn (99.95%) and Ge (99.999%) powders were mixed thoroughly under an argon environment and sealed in a quartz tube at 10^{-4} mbar vacuum. The quartz tube was kept at 1050^{o}C for 24 hours before cooling down to 740^{o}C at a rate of 2^o/hr. After prolonged annealing for 120 hrs, the tube was quenched in ice water. In this way, we could grow the single crystals of Mn_3Ge with a typical size of 2×3 mm^2. As grown single crystals were studied structurally using the X-ray diffraction (XRD) technique to confirm the hexagonal crystal structure with a space group of $P6_3/mmc$ (194). The energy dispersive X-ray spectroscopy (EDS) study suggests an actual chemical composition of $Mn_{2.94\pm0.03}Ge$ for the single crystals which were used for the ARPES measurements. The ARPES measurements were performed at CASSIOPÉE beamline in the SOLEIL synchrotron radiation centre, France, equipped with a SCIENTA R4000 analyzer. The samples were cleaved $in-situ$ under a chamber vacuum of $\approx 5\times10^{-11}$ mbar. The data were collected using photon energies between 83 and 143 eV at a sample temperature of 35 K. The total energy resolution was set to 15 meV.

7.3 Results and Discussion

Mn_3Ge crystallizes in the hexagonal structure as shown in Fig. 7.1(a) with a nonsymmorphic space group of $P6_3/mmc$ (No. 194). One unit cell consists of two layers of Mn_3Ge, while each layer consists of three Mn and one Ge atoms. The two layers of Mn_3Ge stacked along the c-axis are connected by inversion symmetry. The three Mn atoms in a layer

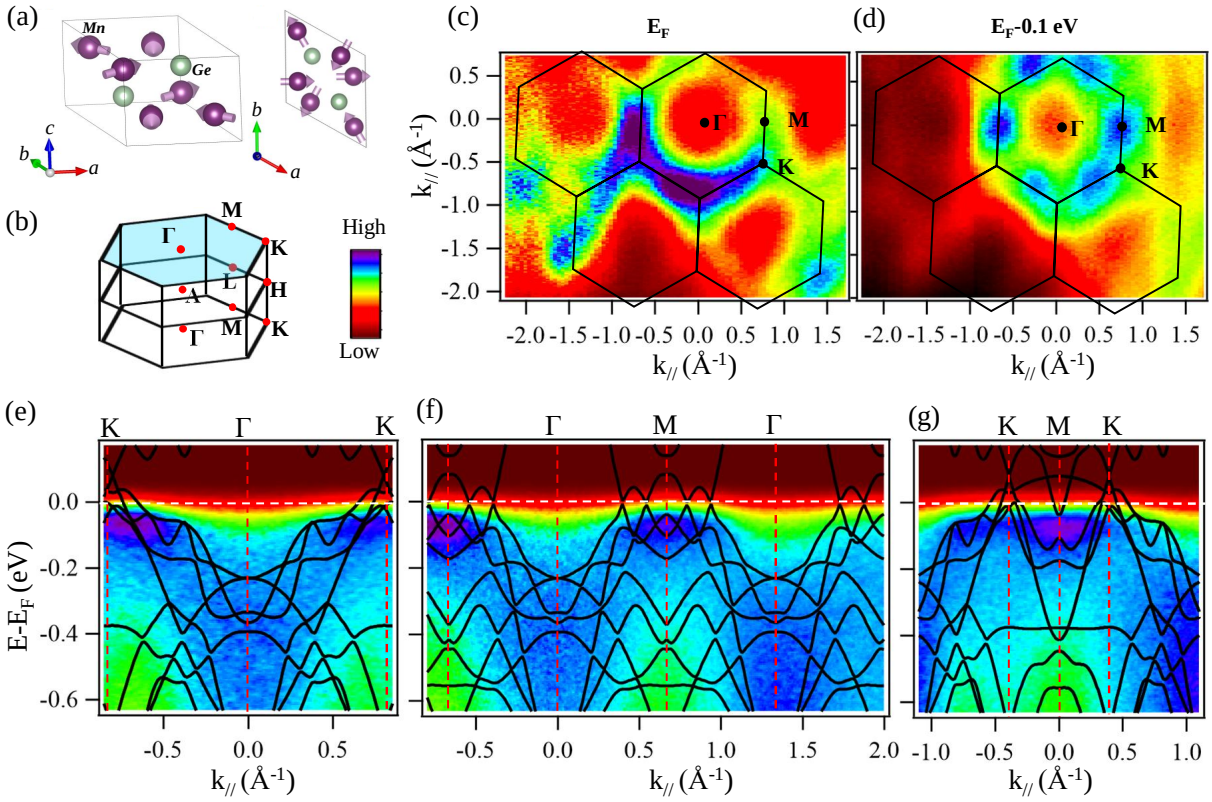

Figure 7.1: Hexagonal (a) crystal structure and (b) BZ of Mn_3Ge. (c) In-plane Fermi surface map. (d) Constant energy contour map taken at 0.1 eV below the Fermi level. Energy distribution maps (EDMs) taken along (e) $\Gamma - K$, (f) $\Gamma - M$, and (g) $M - K$ high symmetry directions. The overlapped black-solid curves in (e)–(g) are the DFT band structure.

form a kagome lattice consisting of triangles and hexagons with the Ge atom positioned at the center of the hexagon [306, 316]. Fig. 7.1(b) shows the hexagonal BZ along with various high symmetry points located at their respective positions. Fig. 7.1(c) shows an in-plane Fermi surface (FS) map measured using $p-$polarized light with a photon energy of $h\nu$=120 eV. Later, we will show that the 120 eV photon energy extracts the electronic bands from $k_z \approx 4.0\ \pi/c$ plane, i.e., the ΓKM plane of the BZ. From Fig. 7.1(c), we can notice that the FS map has a hexagonal symmetry that is consistent with the hexagonal symmetry of the crystal structure. Fig. 7.1(d) shows a constant energy map taken at 100 meV below the Fermi level (E_F). The constant energy map taken at E_F-100 meV is consistent with the Fermi surface of Mn_3Sn [7, 318], where we can observe six high-intensity Fermi pockets at six M points of the BZ. For a better understanding of the nature of Fermi pockets, energy distribution maps (EDMs) taken along the $\Gamma - K$, $\Gamma - M$, and $M - K$ high symmetry directions are shown in Figs. 7.1(e), 7.1(f), and 7.1(g), respectively.

From these EDMs, we notice several well-dispersive electronic bands crossing E_F at high symmetry points M and K, while we could not find any band crossing E_F at the high symmetry point Γ.

Band structure calculations on Mn_3Ge were performed by our collaborators Anumita Bose and Dr. Awadhesh Narayan in IISC Bangalore, India. These calculations employed DFT within the generalized gradient approximation (GGA) of Perdew, Burke, and Ernzerhof (PBE) exchange and correlation potential [322] as implemented in the Quantum Espresso simulation package [323, 324].The electronic band structure calculated using the DFT is overlapped on the EDMs as shown in Figs. 7.1(e)-(g). It is to be noted that the Fermi level of the DFT band structure is shifted by 180 meV towards higher binding energy to match the experimental band dispersions as the Mn deficiency gives a net effect of hole doping into the system. Nevertheless, we find a qualitatve agreement between the DFT band structure and the ARPES data for all high symmetry directions, as can be seen from Figs. 7.1(e)-(g). An earlier report on Mn_3Sn showed the presence of strong electronic correlations, as they had to perform a band renormalization by a factor of five to the DFT band structure in order to obtain a good overlap with ARPES data [7]. In our case, we renormalized the DFT band structure by a factor of 1.18 to match our ARPES data, suggesting that the electronic correlations in Mn_3Ge are relatively weaker compared to Mn_3Sn. This observation is consistent with an earlier theoretical study, which says that Mn_3Ge has a wider bandwidth leading to a smaller band renormalization of a factor of 2 [306].

Fig. 7.2(a) shows the PDOS calculated using the DFT. From Fig. 7.2(a) it is evident that the Mn $3d$ orbital characters dominate the valence band structure, particularly near E_F only the Mn $3d$ orbitals are present. ARPES spectra collected along the $\Gamma - K$ direction with $p-$ and $s-$polarized lights are displayed in Figs. 7.2(b) and 7.2(c), respectively. As per the measuring geometry shown Fig. 7.2(d), the $p-$polarized light extracts the even parity Mn $3d$ orbital characters like d_{xz}, $d_{x^2-y^2}$, and d_{z^2} and the $s-$polarized light extracts the odd parity orbital characters like d_{xy} and d_{yz} in the vicinity of Fermi level. Orbital-resolved band structures for all Mn $3d$ characters are shown in Fig. 7.2(e). By closely comparing the ARPES data shown in Figs. 7.2(b) and 7.2(c) with DFT band structure shown in Fig. 7.2(e), we can qualitatively identify that the $p-$polarized light predominantly extracts the d_{z^2} and $d_{x^2-y^2}$ orbitals, while the $s-$polarized light predominantly extracts the d_{yz} orbital character. Moreover, Mn_3Ge is known to possess flat bands due to the localization of the Mn $3d$ electrons within the kagome lattice [7, 325]. In agreement

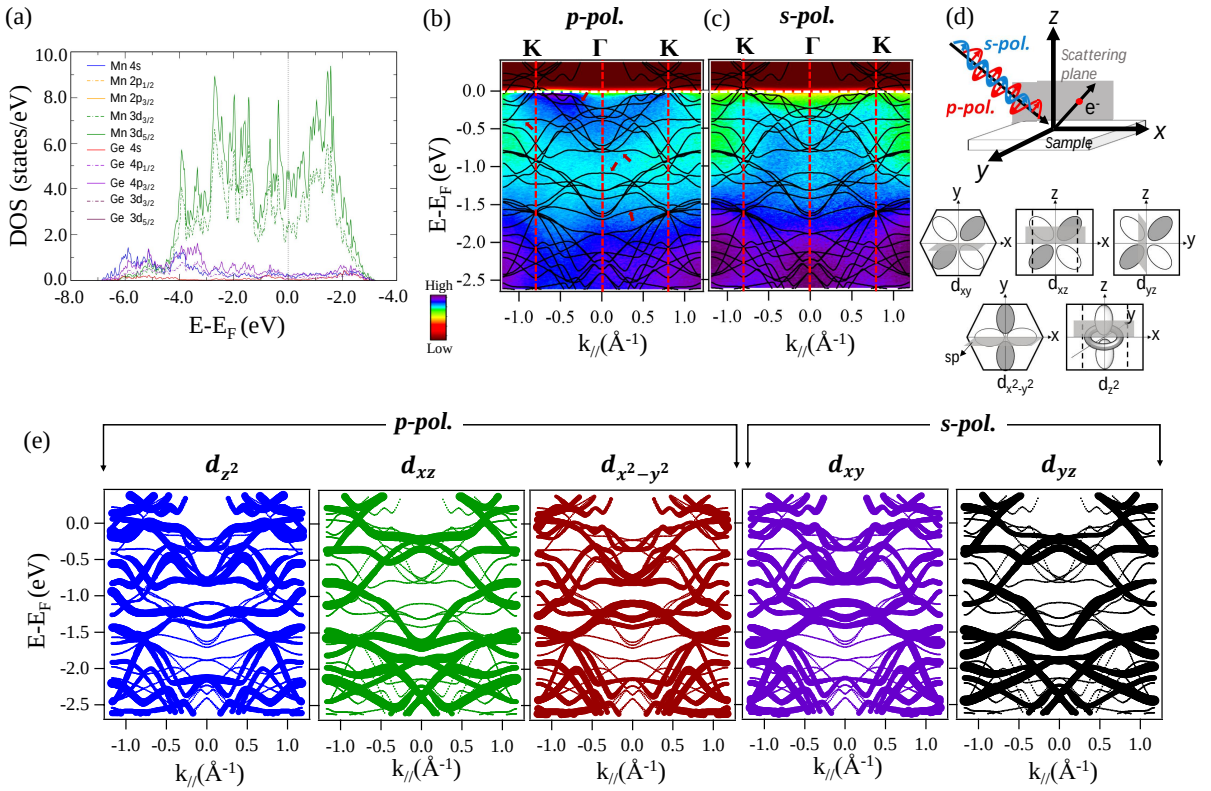

Figure 7.2: (a) PDOS of Mn_3Ge. ARPES spectra along the $\Gamma-K$ direction measured with (b) $p-$polarized and (c) $s-$polarized lights overlapped with the DFT band structure (with SOC). In (a) and (b) panel arrows show the (E,k) location of various flat bands. The top panel in (d) shows schematic ARPES measuring geometry with $p-$ and $s-$polarized lights defined with respect to the scattering plane (sp). The bottom panel in (d) shows various Mn $3d$ orbitals projected onto the hexagonal BZ and oriented w.r.t. the scattering plane. In this measuring geometry, the $p-$polarized light has the even parity and the $s-$polarized light has the odd parity. Similarly, w.r.t. to sp the orbital characters d_{xz}, $d_{x^2-y^2}$, and d_{z^2} have the even parity, while d_{xy} and d_{yz} have the odd parity. (e) Orbital-resolved DFT band structure (without SOC) calculated for Mn $3d$ orbitals, d_{z^2}, d_{xz}, $d_{x^2-y^2}$, d_{xy}, and d_{yz}.

with that, we also observe flat band around K-point at a binding energy of -0.38 eV from the DFT calculations. A hint of flat-band is also visible in the EDM taken along the $\Gamma-K$ direction measured with $p-$polarized [see Fig. 7.2(b)].

Fig. 7.3(a) shows out-of-plane (k_z) Fermi surface map of Mn_3Ge measured by varying the photon energy between 83 and 143 eV with an energy interval of 3 eV using $p-$polarized light. Using an inner potential of V_0=12.5±0.5 eV, we identified that the photon energy 122 eV extracts the electronic states from k_z=4.0 π/c (5.84 Å^{-1}) plane and the photon

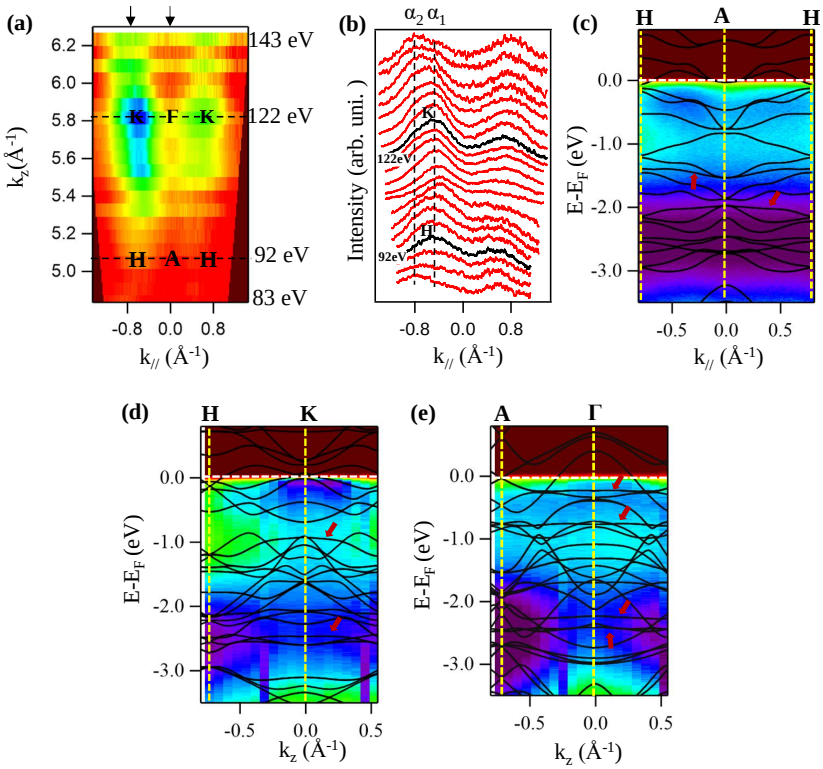

Figure 7.3: (a) Out-of-plane (k_z) Fermi surface map of Mn_3Ge. (b) Stacked momentum dispersive curves (MDCs) taken at the Fermi level from the EDMs measured using the photon energies between 83 and 143 eV. (c), (d), and (e) EDMs taken along the $A-H$, $K-H$, and $\Gamma-A$ high symmetry directions, respectively. The EDMs shown in (d) and (e) are taken along the cuts shown by the down-arrows in (a). The overlapped black-solid curves in (c)–(e) are the DFT band structure. Also the arrows in (c)-(e) show the (E,k) location of several flat bands

energy 92 eV extracts the states from k_z=3.5 π/c (5.12 $Å^{-1}$) plane, following the relation $k_z = \sqrt{\frac{2m_e}{\hbar^2}[E_{kin}cos^2\theta + V_0]}$. Here, m_e is the electron mass and the lattice constant c=4.305 Å. Therefore, the ARPES data shown in Fig. 7.1 measured with 120 eV of photon energy are nearly extracted from k_z=4.0 π/c (ΓKM) plane. Fig. 7.3(b) depicts stacked momentum dispersive curves (MDC) taken at E_F from the EDMs measured using the photon energies between 83 and 143 eV. From the MDCs, we can identity two bands α_1 and α_2 at around K point which are hardly dispersing in going from K to H except that the α_1 and α_2 band intensities vary with photon energy due to the matrix element effects.

Next, the EDM shown in Fig. 7.3(c) is measured with a photon energy of 92 eV corresponding to the band dispersion along the $A-H$ high symmetry direction. As can be seen from Fig. 7.3(c), the overlapped DFT band structure of the $A-H$ direction quan-

titatively matches the experimental band dispersions, supporting the interpretation that the 92 eV photon energy extracts the electronic states from the AHL plane. Figs. 7.3(d) and 7.3(e) show the EDMs taken along the $H-K$ and $A-\Gamma$ directions, respectively. Again, the calculated band structure is qualitatively overlapped on these k_z dependent EDMs. Particularly, we noticed a flat band at around -0.23 eV below the Fermi level from the EDM of the $A-\Gamma$ direction [see Fig. 7.3(e)] and several other flat bands are also noticed far below the Fermi level (-2.5 to -3 eV) from the EDMs of the $H-K$ and $A-H$ directions. These experimental observations are consistent with our DFT calculations.

Overall, we find a qualitative agreement between the experimental and DFT band structures of Mn_3Ge. However, we were unable to detect the Weyl points and the surface Fermi arcs from our ARPES measurements as they are predicted at 90 meV above the Fermi level [305, 306]. Moreover, our sample has a 2% of Mn ($Mn_{2.94}Ge$) deficiency compared to the stoichiometric Mn_3Ge, leading to a further shift of the experimental Fermi level towards the higher binding energy, making it difficult to capture the predicted dispersive surface Fermi arcs. Interestingly, unlike Mn_3Sn which shows band renormalization by a factor of 5, we do not observe significant band renormalization in the experimental band structure of Mn_3Ge when compared with the DFT calculations. Nevertheless, the experimental band structure of this study is as lousy as Mn_3Sn despite weaker electronic correlations [306]. We think, the defects in the case of Mn deficient Mn_3Ge (our study) or the impurities in the case of Mn excess Mn_3Sn [306] responsible for the lousy ARPES data rather than the electronic correlations.

7.4 Conclusions

In conclusion, we have systematically investigated the in-plane and out-of-plane electronic band structure of the non-collinear AFM WSM Mn_3Ge using ARPES and DFT calculations. Overall, the ARPES data match qualitatively with the DFT band structure near the Fermi level. Consistent with DFT predictions, we could observe several flat bands near and well below the Fermi level. Calculated PDOS suggests that the Mn $3d$ orbital characters dominate the valence band structure, particularly near the Fermi level. Further, with the help of orbital-resolved band structure calculations, we identify various Mn $3d$ orbital contributions to the experimentally obtained band structure. We suggest relatively weaker electronic correlations in Mn_3Ge compared to Mn_3Sn.

Chapter 8

Summary of works

A total of five projects are discussed in this thesis. First, we have performed ARPES measurements on the topological system FeSi, which is predicted to host manifold degenerate fermions like spin-1 Weyl fermion and spin-3/2 RSW fermions. Although the band structure matches with the DFT calculation, the Fermi arcs associated with these fermions could not be observed by ARPES as they appear 0.54 eV above the Fermi level. Additionally, we observe the presence of spin-orbit band splitting along the X-M direction, which confirms the importance of consideration of SOC while performing band structure calculations in these systems.

The second project presents the ARPES measurements on $K_{0.65}RhO_2$, a system predicted to be a quantum topological Hall insulator. The ARPES data shows no topologically protected band dispersions. However, we observe the presence of strong electron-phonon coupling which is strongly momentum dependent both in-plane and out-of-plane directions. We also observe the presence of a high-energy kink at 195 meV, possibly arising from electron boson coupling that causes anomalous band renormalization near the Fermi level.

In the third project, we performed magnetic, transport, and electronic structure studies on $Mn_{1-x}Sn_xBi_2Te_4$ (x=0 to 1), an AFM TI. This reveals that the gradual weakening of AFM ordering with nonmagnetic Sn substitution in Mn sites decreases the magnetic field required to obtain FM ordering in AFM $MnBi_2Te_4$ from 7.8 T (x=0) to 2 T (x=0.68). This opens up the possibility of obtaining a QAH state when working with a few layers. Although the electronic structure confirms that the topological properties remain intact

up to x=0.55, the heavy electron doping in the system will be an obstacle to realizing the Chern insulating state. Introducing elements which can dope holes into the system might help overcome this issue.

In the fourth project, we explored the influence of adding magnetic impurities to the 3D TI Bi_2Se_3. By using ARPES measurements, we analyzed the band structures of pure Bi_2Se_3, $Co_{0.1}Bi_2Se_3$, $Mn_{0.1}Bi_2Se_3$, and $Eu_{0.1}Bi_{1.9}Se_3$. Despite theoretical expectations of gap opening at the Dirac point due to disrupted TRS, our findings revealed that a minor impurity concentration (10%) does not induce this effect. The sole impact of the impurities on the band structure was a noticeable upward shift of the Fermi level, signifying electron doping into the system.

The fifth project studies the low-energy electronic structure of Mn_3Ge, a WSM with non-collinear antiferromagnetic ordering. Notably, the non-zero Berry curvature between its Weyl nodes gives rise to a giant AHE. So far, this was the only experimental evidence of the existence of these nodes. Our aim was to observe these Weyl nodes through ARPES measurements directly. However, the complex valence band structure obstructed the experimental realization of these nodes. The ARPES measurements reveal several flat-bands along various high symmetry directions of Mn_3Ge. We further identified the specific orbital details of the experimentally observed band dispersion by comparing ARPES data taken with both $p-$ and $s-$ polarizations to the orbital-resolved band structure calculations.

Bibliography

[1] Klaus von Klitzing. The quantized Hall effect. *Rev. Mod. Phys.*, 58:519–531, Jul 1986.

[2] B Andrei Bernevig, Taylor L Hughes, and Shou-Cheng Zhang. Quantum spin Hall effect and topological phase transition in HgTe quantum wells. *science*, 314(5806):1757–1761, 2006.

[3] M. Z. Hasan and C. L. Kane. *Colloquium* : Topological insulators. *Rev. Mod. Phys.*, 82:3045–3067, Nov 2010.

[4] David Hsieh, Dong Qian, Lewis Wray, Yiman Xia, Yew San Hor, Robert Joseph Cava, and M Zahid Hasan. A topological dirac insulator in a quantum spin hall phase. *Nature*, 452(7190):970–974, 2008.

[5] Yujun Deng, Yijun Yu, Meng Zhu Shi, Zhongxun Guo, Zihan Xu, Jing Wang, Xian Hui Chen, and Yuanbo Zhang. Quantum anomalous Hall effect in intrinsic magnetic topological insulator $MnBi_2Te_4$. *Science*, 367(6480):895–900, 2020.

[6] Jian Zhou, Qi-Feng Liang, Hongming Weng, Y. B. Chen, Shu-Hua Yao, Yan-Feng Chen, Jinming Dong, and Guang-Yu Guo. Predicted Quantum Topological Hall Effect and Noncoplanar Antiferromagnetism in $K_{0.5}RhO_2$. *Phys. Rev. Lett.*, 116:256601, Jun 2016.

[7] K Kuroda, T Tomita, M-T Suzuki, C Bareille, AA Nugroho, Pallab Goswami, M Ochi, M Ikhlas, M Nakayama, S Akebi, et al. Evidence for magnetic weyl fermions in a correlated metal. *Nature materials*, 16(11):1090–1095, 2017.

[8] Hao Yang, Yan Sun, Yang Zhang, Wu-Jun Shi, Stuart SP Parkin, and Binghai Yan. Topological weyl semimetals in the chiral antiferromagnetic materials mn3ge and mn3sn. *New Journal of Physics*, 19(1):015008, 2017.

[9] Peizhe Tang, Quan Zhou, and Shou-Cheng Zhang. Multiple types of topological fermions in transition metal silicides. *Phys. Rev. Lett.*, 119:206402, Nov 2017.

[10] Daichi Takane, Zhiwei Wang, Seigo Souma, Kosuke Nakayama, Takechika Nakamura, Hikaru Oinuma, Yuki Nakata, Hideaki Iwasawa, Cephise Cacho, Timur Kim, Koji Horiba, Hiroshi Kumigashira, Takashi Takahashi, Yoichi Ando, and Takafumi Sato. Observation of chiral fermions with a large topological charge and associated fermi-arc surface states in cosi. *Phys. Rev. Lett.*, 122:076402, Feb 2019.

[11] Guoqing Chang, Jia-Xin Yin, Titus Neupert, Daniel S. Sanchez, Ilya Belopolski, Songtian S. Zhang, Tyler A. Cochran, Zǐji ā Chéng, Ming-Chien Hsu, Shin-Ming Huang, Biao Lian, Su-Yang Xu, Hsin Lin, and M. Zahid Hasan. Unconventional photocurrents from surface fermi arcs in topological chiral semimetals. *Phys. Rev. Lett.*, 124:166404, Apr 2020.

[12] M. P. Seah and W. A. Dench. Quantitative electron spectroscopy of surfaces: A standard data base for electron inelastic mean free paths in solids. *Surf. Interface Anal.*, 1(1):2–11, feb 1979.

[13] https://www.rrcat.gov.in/technology/accel/srul/beamlines/arpes.html.

[14] K. v. Klitzing, G. Dorda, and M. Pepper. New method for high-accuracy determination of the fine-structure constant based on quantized hall resistance. *Phys. Rev. Lett.*, 45:494–497, Aug 1980.

[15] A. Stern and N. H. Lindner. Topological quantum computation–from basic concepts to first experiments. *Science*, 339(6124):1179–1184, mar 2013.

[16] Congjun Wu, B. Andrei Bernevig, and Shou-Cheng Zhang. Helical Liquid and the Edge of Quantum Spin Hall Systems. *Physical Review Letters*, 105(7):077001, 2010.

[17] Guoqing Chang, Su-Yang Xu, Daniel S. Sanchez, Shin-Ming Huang, Chi-Cheng Lee, Tay-Rong Chang, Guang Bian, Hao Zheng, Ilya Belopolski, Nasser Alidoust, Horng-Tay Jeng, Arun Bansil, Hsin Lin, and M. Zahid Hasan. A strongly robust type II Weyl fermion semimetal state in Ta_3S_2. *Science Advances*, 2(6), 2016.

[18] A. H. Castro Neto, F. Guinea, N. M. R. Peres, K. S. Novoselov, and A. K. Geim. The electronic properties of graphene. *Rev. Mod. Phys.*, 81:109–162, Jan 2009.

[19] V. Mourik, K. Zuo, S. M. Frolov, S. R. Plissard, E. P. A. M. Bakkers, and L. P. Kouwenhoven. Signatures of majorana fermions in hybrid superconductor-semiconductor nanowire devices. *Science*, 336(6084):1003–1007, apr 2012.

[20] Q. L. He, L. Pan, A. L. Stern, E. C. Burks, X. Che, G. Yin, J. Wang, B. Lian, Q. Zhou, W. Choi, et al. Chiral majorana fermion modes in a quantum anomalous hall insulator–superconductor structure. *Science*, 357:294, 2017.

[21] Mojammel A. Khan, D. E. Graf, I. Vekhter, D. A. Browne, J. F. DiTusa, W. Adam Phelan, and D. P. Young. Quantum oscillations and a nontrivial Berry phase in the noncentrosymmetric topological superconductor candidate BiPd. *Phys. Rev. B*, 99:020507, Jan 2019.

[22] M.-X. Wang, H. Liu, J.-P. Xu, L. Fu, S.-C. Zhang, and D. Wang. Quantum transport evidence for the three-dimensional Dirac semimetal phase in Cd_3As_2. *Science*, 336:52, 2012.

[23] Z. K. Liu, B. Zhou, Y. Zhang, Z. J. Wang, H. M. Weng, D. Prabhakaran, S.-K. Mo, Z. X. Shen, Z. Fang, X. Dai, Z. Hussain, and Y. L. Chen. Discovery of a Three-Dimensional Topological Dirac Semimetal, Na_3Bi. *Science*, 343(6173):864–867, jan 2014.

[24] Xiaochun Huang, Lingxiao Zhao, Yujia Long, Peipei Wang, Dong Chen, Zhanhai Yang, Hui Liang, Mianqi Xue, Hongming Weng, Zhong Fang, Xi Dai, and Genfu Chen. Observation of the Chiral-Anomaly-Induced Negative Magnetoresistance in 3D Weyl Semimetal TaAs. *Phys. Rev. X*, 5:031023, Aug 2015.

[25] Stevan Nadj-Perge, Ilya K. Drozdov, Jian Li, Hua Chen, Sangjun Jeon, Jungpil Seo, Allan H. MacDonald, B. Andrei Bernevig, and Ali Yazdani. Observation of Majorana fermions in ferromagnetic atomic chains on a superconductor. *Science*, 346(6209):602–607, 2014.

[26] Barry Bradlyn, Jennifer Cano, Zhijun Wang, M. G. Vergniory, C. Felser, R. J. Cava, and B. Andrei Bernevig. Beyond dirac and weyl fermions: Unconventional quasiparticles in conventional crystals. *Science*, 353(6299):aaf5037, jul 2016.

[27] D. J. Thouless, M. Kohmoto, M. P. Nightingale, and M. den Nijs. Quantized Hall Conductance in a Two-Dimensional Periodic Potential. *Phys. Rev. Lett.*, 49:405–408, Aug 1982.

[28] F. D. M. Haldane. Model for a Quantum Hall Effect without Landau Levels: Condensed-Matter Realization of the 'Parity Anomaly'. *Physical Review Letters*, 61(18):2015, 1983.

[29] L. Landau. Diamagnetismus der metalle. *Zeitschrift für Physik*, 64(9-10):629–637, 1930.

[30] B. I. Halperin. Quantized hall conductance, current-carrying edge states, and the existence of extended states in a two-dimensional disordered potential. *Physical Review B*, 25(4):2185–2195, 1982.

[31] Markus Büttiker. Quantization of the conductance of a bloch quantum dot. *Physical Review B*, 38(14):9375–9389, 1988.

[32] Felix Bloch. Über die quantenmechanik der elektronen in kristallgittern. *Zeitschrift für Physik*, 52(7-8):555–600, 1929.

[33] Michael V. Berry. Quantal phase factors accompanying adiabatic changes. *Proceedings of the Royal Society of London. A. Mathematical and Physical Sciences*, 392(1802):45–57, 1984.

[34] Marco Abate and Francesca Tovena. *Curves and Surfaces*. Springer Milan, 2012.

[35] Bert Mendelson. *Introduction to Topology: Third Edition*. Dover Publications, 2012.

[36] J. E. Hirsch. Spin Hall effect. *Physical Review Letters*, 83(9):1834, 1999.

[37] C. L. Kane and E. J. Mele. Z_2 Topological Order and the Quantum Spin Hall Effect. *Physical Review Letters*, 95(14):146802, 2005.

[38] M. König, S. Wiedmann, C. Brüne, A. Roth, H. Buhmann, L. W. Molenkamp, X.-L. Qi, and S.-C. Zhang. Quantum Spin Hall Insulator State in HgTe Quantum Wells. *Science*, 318(5851):766–770, 2007.

[39] Liang Fu and C. L. Kane. Topological insulators with inversion symmetry. *Phys. Rev. B*, 76:045302, Jul 2007.

[40] Liang Fu, C. L. Kane, and E. J. Mele. Topological insulators in three dimensions. *Physical Review Letters*, 98(10):106803, 2007.

[41] Haijun Zhang, Chao-Xing Liu, Xiao-Liang Qi, Xi Dai, Zhong Fang, and Shou-Cheng Zhang. Topological insulators in Bi_2Se_3, Bi_2Te_3 and Sb_2Te_3 with a single Dirac cone on the surface. *Nature Physics*, 5(6):438–442, 2009.

[42] Hadj M. Benia, Carola Straßer, Klaus Kern, and Christian R. Ast. Surface band structure of $Bi_{1-x}Sb_x(111)$. *Phys. Rev. B*, 91:161406, Apr 2015.

[43] Y. L. Chen, J. G. Analytis, J. H. Chu, Z. K. Liu, S.-K. Mo, X. L. Qi, H. J. Zhang, D. H. Lu, X. Dai, Z. Fang, S. C. Zhang, I. R. Fisher, Z. Hussain, and Z. X. Shen. Experimental realization of a three-dimensional topological insulator, Bi_2Te_3. *Science*, 325(5937):178–181, 2009.

[44] Y. Xia, D. Qian, D. Hsieh, L. Wray, A. Pal, H. Lin, A. Bansil, D. Grauer, Y. S. Hor, R. J. Cava, and M. Z. Hasan. Observation of a large-gap topological-insulator class with a single Dirac cone on the surface. *Nature Physics*, 5(6):398–402, 2009.

[45] F. D. M. Haldane. Model for a quantum hall effect without landau levels: Condensed-matter realization of the "parity anomaly". *Phys. Rev. Lett.*, 61:2015–2018, Oct 1988.

[46] Qin Liu, Chao-Xing Liu, Cenke Xu, Xiao-Liang Qi, and Shou-Cheng Zhang. Magnetic Impurities on the Surface of a Topological Insulator. *Phys. Rev. Lett.*, 102:156603, Apr 2009.

[47] A. Budewitz, K. Bendias, P. Leubner, T. Khouri, S. Shamim, S. Wiedmann, H. Buhmann, and L. Molenkamp. Quantum anomalous Hall effect in Mn doped HgTe quantum wells. *arXiv preprint arXiv:1706.05789*, 2017.

[48] Cui-Zu Chang, Jinsong Zhang, Xiao Feng, Jie Shen, Zuocheng Zhang, Minghua Guo, Kang Li, Yunbo Ou, Pang Wei, Li-Li Wang, et al. Experimental observation of the quantum anomalous hall effect in a magnetic topological insulator. *Science*, 340(6129):167–170, 2013.

[49] Cui-Zu Chang, Weiwei Zhao, Duk Y Kim, Jinsong Zhang, Badih Assaf, Don Heiman, Shou-Cheng Zhang, Chaoxing Liu, Moses H W Chan, and Jagadeesh S Moodera. High-precision realization of robust quantum anomalous hall state in a hard ferromagnetic topological insulator. *Nature Materials*, 14(5):473–477, 2015.

[50] Aaron L Sharpe, Eli J Fox, Arthur W Barnard, Joe Finney, Kenji Watanabe, Takashi Taniguchi, MA Kastner, and David Goldhaber-Gordon. Emergent ferromagnetism near three-quarters filling in twisted bilayer graphene. *Science*, 365(6453):605–608, 2019.

[51] M Serlin, CL Tschirhart, H Polshyn, Y Zhang, J Zhu, K Watanabe, T Taniguchi, L Balents, and AF Young. Intrinsic quantized anomalous hall effect in a moiré heterostructure. *Science*, 367(6480):900–903, 2020.

[52] Fabian R Geisenhof, Felix Winterer, Anna M Seiler, Jakob Lenz, Tianyi Xu, Fan Zhang, and R Thomas Weitz. Quantum anomalous hall octet driven by orbital magnetism in bilayer graphene. *Nature*, 598(7879):53–58, 2021.

[53] Tingxin Li, Shengwei Jiang, Bowen Shen, Yang Zhang, Lizhong Li, Zui Tao, Trithep Devakul, Kenji Watanabe, Takashi Taniguchi, Liang Fu, et al. Quantum anomalous hall effect from intertwined moiré bands. *Nature*, 600(7890):641–646, 2021.

[54] Xiao-Liang Qi and Shou-Cheng Zhang. Topological insulators and superconductors. *Rev. Mod. Phys.*, 83:1057–1110, Oct 2011.

[55] Yujun Deng, Yijun Yu, Meng Zhu Shi, Zhongxun Guo, Zihan Xu, Jing Wang, Xian Hui Chen, and Yuanbo Zhang. Quantum anomalous Hall effect in intrinsic magnetic topological insulator $MnBi_2Te_4$. *Science*, 367(6480):895–900, 2020.

[56] Chang Liu, Yongchao Wang, Hao Li, Yang Wu, Yaoxin Li, Jiaheng Li, Ke He, Yong Xu, Jinsong Zhang, and Yayu Wang. Robust axion insulator and Chern insulator phases in a two-dimensional antiferromagnetic topological insulator. *Nature materials*, 19(5):522–527, 2020.

[57] Xiangang Wan, Ari M. Turner, Ashvin Vishwanath, and Sergey Y. Savrasov. Topological semimetal and Fermi-arc surface states in the electronic structure of pyrochlore iridates. *Phys. Rev. B*, 83:205101, May 2011.

[58] B. Q. Lv, H. M. Weng, B. B. Fu, X. P. Wang, H. Miao, J. Ma, P. Richard, X. C. Huang, L. X. Zhao, G. F. Chen, Z. Fang, X. Dai, T. Qian, and H. Ding. Experimental discovery of weyl semimetal taas. *Phys. Rev. X*, 5:031013, Jul 2015.

[59] A. A. Soluyanov and D. Vanderbilt. Weyl semimetals from noncentrosymmetric topological insulators. *Physical Review B*, 91(20):201104, 2015.

[60] N. P. Armitage, E. J. Mele, and A. Vishwanath. Weyl and dirac semimetals in three-dimensional solids. *Reviews of Modern Physics*, 90(1):015001, 2018.

[61] Madhab Neupane, Su-Yang Xu, Raman Sankar, Nasser Alidoust, Guang Bian, Chang Liu, Ilya Belopolski, Tay-Rong Chang, Horng-Tay Jeng, Hsin Lin, Arun Bansil, Fangcheng Chou, and M. Zahid Hasan. Observation of a three-dimensional topological Dirac semimetal phase in high-mobility Cd_3As_2. *Nature Communications*, 5, may 2014.

[62] Z. K. Liu, J. Jiang, B. Zhou, Z. J. Wang, Y. Zhang, H. M. Weng, D. Prabhakaran, S-K. Mo, H. Peng, P. Dudin, T. Kim, M. Hoesch, Z. Fang, X. Dai, Z. X. Shen, D. L. Feng, Z. Hussain, and Y. L. Chen. A stable three-dimensional topological Dirac semimetal Cd_3As_2. *Nature Materials*, 13(7):677–681, may 2014.

[63] Sergey Borisenko, Quinn Gibson, Danil Evtushinsky, Volodymyr Zabolotnyy, Bernd Büchner, and Robert J. Cava. Experimental realization of a three-dimensional dirac semimetal. *Phys. Rev. Lett.*, 113:027603, Jul 2014.

[64] S.-Y. Xu, I. Belopolski, N. Alidoust, M. Neupane, G. Bian, C. Zhang, R. Sankar, G. Chang, Z. Yuan, C.-C. Lee, S.-M. Huang, H. Zheng, J. Ma, D. S. Sanchez, B. Wang, A. Bansil, F. Chou, P. P. Shibayev, H. Lin, S. Jia, and M. Z. Hasan. Discovery of a weyl fermion semimetal and topological fermi arcs. *Science*, 349(6248):613–617, jul 2015.

[65] P. A. M. Dirac. The quantum theory of the electron. *Proceedings of the Royal Society of London. Series A*, 117(778):610–624, 1928.

[66] H. Weyl. Elektron und gravitation. *Zeitschrift für Physik*, 56(5-6):330–352, 1929.

[67] C. Shekhar, A. K. Nayak, Y. Sun, M. Schmidt, M. Nicklas, I. Leermakers, U. Zeitler, Y. Skourski, J. Wosnitza, Z. Liu, et al. Extremely large magnetoresistance and ultrahigh mobility in the topological weyl semimetal candidate nbp. *Nature Physics*, 11:645–649, 2015.

[68] Nitesh Kumar, Mun K. Chan, H. Lin, M. Neupane, D. S. Sanchez, I. Belopolski, M. Uchida, Y. Suzuki, S. Nishizaki, T. Kondo, et al. Thermodynamic signatures of weyl fermions in nbp. *Scientific Reports*, 9:20950, 2019.

[69] S. Y. Xu, I. Belopolski, N. Alidoust, M. Neupane, G. Bian, C. Zhang, R. Sankar, G. Chang, Z. Yuan, C. C. Lee, et al. Discovery of a weyl fermion state with fermi arcs in niobium arsenide. *Nature Physics*, 11:748, 2015.

[70] S. Thirupathaiah, Rajveer Jha, Banabir Pal, J. S. Matias, P. Kumar Das, P. K. Sivakumar, I. Vobornik, N. C. Plumb, M. Shi, R. A. Ribeiro, and D. D. Sarma. $MoTe_2$: An uncompensated semimetal with extremely large magnetoresistance. *Phys. Rev. B (R)*, 95:241105, Jun 2017.

[71] S. Thirupathaiah, Rajveer Jha, Banabir Pal, J. S. Matias, P. Kumar Das, I. Vobornik, R. A. Ribeiro, and D. D. Sarma. Temperature-independent band structure of WTe_2 as observed from angle-resolved photoemission spectroscopy. *Phys. Rev. B*, 96:165149, Oct 2017.

[72] K. Deng, G. Wan, P. Deng, K. Zhang, S. Ding, E. Wang, M. Yan, H. Huang, H. Zhang, Z. Xu, et al. Signature of type-II Weyl semimetal phase in $MoTe_2$. *Nature Communications*, 8:13973, 2017.

[73] Yun Wu, Daixiang Mou, Na Hyun Jo, K. Sun, Lunan Huang, S. L. Bud'ko, P. C. Canfield, J. Park, A. Richardella, J. Kally, et al. Evidence for topological type-II Weyl semimetal WTe_2. *Nature Communications*, 8:2150, 2017.

[74] Indrani Kar, Joydeep Chatterjee, Luminita Harnagea, Y. Kushnirenko, A. V. Fedorov, Deepika Shrivastava, B. Büchner, P. Mahadevan, and S. Thirupathaiah. Metal-chalcogen bond-length induced electronic phase transition from semiconductor to topological semimetal in ZrX_2 (X = Se and Te). *Phys. Rev. B*, 101:165122, Apr 2020.

[75] J. Kubler and C. Felser. Weyl fermions in antiferromagnetic mn_3sn and mn_3ge. *Europhysics Letters*, 120:47002, 2018.

[76] C.-Y. Huang, H. Aramberri, H. Lin, and N. Kioussis. Noncollinear magnetic modulation of Weyl nodes in ferrimagnetic Mn_3Ga. *Physical Review B*, 102:094403, 2020.

[77] Achintya Low, Susanta Ghosh, Sayan Routh, and Setti Thirupathaiah. Experimental realization of room temperature topological hall effect in kagome antiferromagnet. *arXiv preprint arXiv:2112.15409*, 2021.

[78] T. Yu, R. Liu, Y. Peng, P. Zheng, G. Wang, X. Ma, Z. Yuan, and Z. Yin. Correlated electronic structure of the kagome metal Mn_3Sn. *Physical Review B*, 106:205103, 2022.

[79] Achintya Low, Susanta Ghosh, Soumya Ghorai, and Setti Thirupathaiah. Effect of Electron-Phonon Scattering on the Anomalous Hall Conductivity of Fe $_3$ Sn: A Kagome Ferromagnetic Metal. *arXiv preprint arXiv:2308.11177*, 2023.

[80] Susanta Ghosh, Achintya Low, Soumya Ghorai, Kalyan Mandal, and Setti Thirupathaiah. Tuning of electrical, magnetic, and topological properties of magnetic Weyl semimetal $Mn_{3+x}Ge$ by Fe doping. *Journal of Physics: Condensed Matter*, 2023.

[81] Naoki Kiyohara, Takahiro Tomita, and Satoru Nakatsuji. Giant anomalous hall effect in the chiral antiferromagnet mn_3Ge. *Phys. Rev. Appl.*, 5:064009, Jun 2016.

[82] Woori Ju, Jinwon Jeong, En-Jin Cho, Han-Jin Noh, Kyoo Kim, and Byeong-Gyu Park. Fine details of sixfold Dirac fermions in pyrite-structured $PdSb_2$. *Phys. Rev. B*, 106:205125, Nov 2022.

[83] Bruce D Popp. *Henri Poincaré: Electrons to Special Relativity*. Springer, 2020.

[84] Theo Hahn, editor. *International Tables for Crystallography*, volume A. Wiley, Chester, 5th edition, 2002.

[85] William Rarita and Julian Schwinger. On a theory of particles with half-integral spin. *Phys. Rev.*, 60:61–61, Jul 1941.

[86] Chen Fang, Matthew J. Gilbert, Xi Dai, and B. Andrei Bernevig. Multi-weyl topological semimetals stabilized by point group symmetry. *Phys. Rev. Lett.*, 108:266802, Jun 2012.

[87] Guoqing Chang, Su-Yang Xu, Benjamin J. Wieder, Daniel S. Sanchez, Shin-Ming Huang, Ilya Belopolski, Tay-Rong Chang, Songtian Zhang, Arun Bansil, Hsin Lin, and M. Zahid Hasan. Unconventional chiral fermions and large topological fermi arcs in rhsi. *Phys. Rev. Lett.*, 119:206401, Nov 2017.

[88] Susmita Changdar, S. Aswartham, Anumita Bose, Y. Kushnirenko, G. Shipunov, N. C. Plumb, M. Shi, Awadhesh Narayan, B. Büchner, and S. Thirupathaiah.

Electronic structure studies of FeSi: A chiral topological system. *Phys. Rev. B*, 101:235105, Jun 2020.

[89] Susmita Changdar, Grigory Shipunov, Nesta B. Joseph, Nicholas C. Plumb, Ming Shi, Bernd Büchner, Awadhesh Narayan, Saicharan Aswartham, and Setti Thirupathaiah. Anomalous band renormalization due to a high-energy kink in $K_{0.65}RhO_2$ with colossal thermoelectric power factor. *Phys. Rev. Mater.*, 5:055402, May 2021.

[90] William G. Pfann. Principles of zone-melting. *JOM*, 4:747–753, 1952.

[91] K.N. Mason. Growth and characterization of transition metal silicides. *Progress in Crystal Growth and Characterization*, 2:269–307, 1979.

[92] Paul C. Canfield and Z. Fisk. Growth of single crystals from metallic fluxes. *Philosophical magazine B*, 65(6):1117–1123, 1992.

[93] Christian A. Juillerat, Vladislav V. Klepov, Gregory Morrison, Kristen A. Pace, and Hans-Conrad Zur Loye. Flux crystal growth: a versatile technique to reveal the crystal chemistry of complex uranium oxides. *Dalton Transactions*, 48(10):3162–3181, 2019.

[94] Susmita Changdar, Rabia Sultana, Soma Banik, V. P. S. Awana, and Setti Thirupathaiah. Angle resolved photoemission spectroscopy study on electronic band structure of topological insulator Bi_2Se_3 in the presence of magnetic impurities. *AIP Conference Proceedings*, 2265(1):030355, 11 2020.

[95] Susmita Changdar, Susanta Ghosh, Kritika Vijay, Indrani Kar, Sayan Routh, PK Maheshwari, Soumya Ghorai, Soma Banik, and S Thirupathaiah. Nonmagnetic Sn doping effect on the electronic and magnetic properties of antiferromagnetic topological insulator $MnBi_2Te_4$. *Physica B: Condensed Matter*, 657:414799, 2023.

[96] J.-Q. Yan, S. Nandi, B. Saparov, P. Čermák, Y. Xiao, Y. Su, W. T. Jin, A. Schneidewind, Th. Brückel, R. W. McCallum, T. A. Lograsso, B. C. Sales, and D. G. Mandrus. Magnetic and structural transitions in $La_{0.4}Na_{0.6}Fe_2As_2$ single crystals. *Phys. Rev. B*, 91:024501, Jan 2015.

[97] Jimin Kim, Hoon Kim, Hyun-Woo J. Kim, Sunwook Park, Jin-Kwang Kim, Junyoung Kwon, Jungho Kim, Hyeong Woo Seo, Jun Sung Kim, and B. J. Kim. Single crystal growth of iridates without platinum impurities. *Phys. Rev. Mater.*, 6:103401, Oct 2022.

[98] William Henry Bragg and William Lawrence Bragg. The reflection of x-rays by crystals. *Proceedings of the Royal Society of London. Series A, Containing Papers of a Mathematical and Physical Character*, 88(605):428–438, 1913.

[99] IC Madsen and RJ Hill. Effect of divergence and receiving slit dimensions on peak profile parameters in rietveld analysis of x-ray diffractometer data. *Journal of applied crystallography*, 21(5):398–405, 1988.

[100] Andreas Förster, Stefan Brandstetter, and Clemens Schulze-Briese. Transforming x-ray detection with hybrid photon counting detectors. *Philosophical Transactions of the Royal Society A*, 377(2147):20180241, 2019.

[101] Betty Isabelle Bleaney, Betty Isabelle Bleaney, and Brebis Bleaney. *Electricity and Magnetism, Volume 2*, volume 2. Oxford University Press (UK), 2013.

[102] L. J. van der PAUW. *A method of measuring specific resistivity and Hall effect of discs of arbitrary shape*, pages 174–182. 1991.

[103] B. H. Bransden and C. J Joachain. *Quantum Mechanics (2nd ed.)*. 1999.

[104] Andrea Damascelli, Zahid Hussain, and Zhi-Xun Shen. Angle-resolved photoemission studies of the cuprate superconductors. *Reviews of Modern Physics*, 75(2):473–541, Apr 2003.

[105] *Very high resolution photoelectron spectroscopy, author=Hüfner, Stephan*, volume 715. Springer, 2007.

[106] B Hellsing, Asier Eiguren, and Eugene V Chulkov. Electron-phonon coupling at metal surfaces. *Journal of Physics: Condensed Matter*, 14(24):5959, 2002.

[107] K. S. Novoselov, A. K. Geim, S. V. Morozov, D. Jiang, M. I. Katsnelson, I. V. Grigorieva, S. V. Dubonos, and A. A. Firsov. Two-dimensional gas of massless dirac fermions in graphene. *Nature*, 438(7065):197–200, nov 2005.

[108] A. H. Castro Neto, F. Guinea, N. M. R. Peres, K. S. Novoselov, and A. K. Geim. The electronic properties of graphene. *Rev. Mod. Phys.*, 81:109–162, Jan 2009.

[109] Wei Zhang, Rui Yu, Wanxiang Feng, Yugui Yao, Hongming Weng, Xi Dai, and Zhong Fang. Topological Aspect and Quantum Magnetoresistance of $\beta-Ag_2Te$. *Phys. Rev. Lett.*, 106(15), apr 2011.

[110] Fran çois Virot, Roland Hayn, Manuel Richter, and Jeroen van den Brink. Metacinnabar (β-HgS): A Strong 3D Topological Insulator with Highly Anisotropic Surface States. *Phys. Rev. Lett.*, 106:236806, Jun 2011.

[111] Binghai Yan, Lukas Müchler, and Claudia Felser. Prediction of weak topological insulators in layered semiconductors. *Phys. Rev. Lett.*, 109:116406, Sep 2012.

[112] S. M. Young, S. Zaheer, J. C. Y. Teo, C. L. Kane, E. J. Mele, and A. M. Rappe. Dirac semimetal in three dimensions. *Phys. Rev. Lett.*, 108:140405, Apr 2012.

[113] Zhijun Wang, Yan Sun, Xing-Qiu Chen, Cesare Franchini, Gang Xu, Hongming Weng, Xi Dai, and Zhong Fang. Dirac semimetal and topological phase transitions in A_3Bi (A = Na , K, Rb). *Phys. Rev. B*, 85(19):195320, may 2012.

[114] Zhijun Wang, Hongming Weng, Quansheng Wu, Xi Dai, and Zhong Fang. Three-dimensional Dirac semimetal and quantum transport in Cd_3As_2. *Phys. Rev. B*, 88:125427, Sep 2013.

[115] Madhab Neupane, Su-Yang Xu, Raman Sankar, Nasser Alidoust, Guang Bian, Chang Liu, Ilya Belopolski, Tay-Rong Chang, Horng-Tay Jeng, Hsin Lin, Arun Bansil, Fangcheng Chou, and M. Zahid Hasan. Observation of a three-dimensional topological Dirac semimetal phase in high-mobility Cd_3As_2. *Nature Communications*, 5, may 2014.

[116] C. Zhang, Z. Yuan, S. Xu, Z. Lin, B. Tong, M. Zahid Hasan, J. Wang, C. Zhang, and S. Jia. Tantalum Monoarsenide: an Exotic Compensated Semimetal. *ArXiv e-prints*, February 2015.

[117] N J Ghimire, Yongkang Luo, M Neupane, D J Williams, E D Bauer, and F Ronning. Magnetotransport of single crystalline NbAs. *Journal of Physics: Condensed Matter*, 27(15):152201, mar 2015.

[118] Chandra Shekhar, Ajaya K. Nayak, Yan Sun, Marcus Schmidt, Michael Nicklas, Inge Leermakers, Uli Zeitler, Yurii Skourski, Jochen Wosnitza, Zhongkai Liu, Yulin Chen, Walter Schnelle, Horst Borrmann, Yuri Grin, Claudia Felser, and Binghai Yan. Extremely large magnetoresistance and ultrahigh mobility in the topological Weyl semimetal candidate NbP. *Nature Physics*, 11(8):645–649, jun 2015.

[119] N. Xu, Z. J. Wang, A. P. Weber, A. Magrez, P. Bugnon, H. Berger, C. E. Matt, J. Z. Ma, B. B. Fu, B. Q. Lv, N. C. Plumb, M. Radovic, E. Pomjakushina, K. Conder,

T. Qian, J. H. Dil, J. Mesot, H. Ding, and M. Shi. Discovery of Weyl Semimetal State Violating Lorentz Invariance in $MoTe_2$. April 2016.

[120] A. Tamai, Q. S. Wu, I. Cucchi, F. Y. Bruno, S. Riccò, T. K. Kim, M. Hoesch, C. Barreteau, E. Giannini, C. Besnard, A. A. Soluyanov, and F. Baumberger. Fermi Arcs and Their Topological Character in the Candidate Type-II Weyl Semimetal $MoTe_2$. *Phys. Rev. X*, 6:031021, Aug 2016.

[121] Ke Deng, Guoliang Wan, Peng Deng, Kenan Zhang, Shijie Ding, Eryin Wang, Mingzhe Yan, Huaqing Huang, Hongyun Zhang, Zhilin Xu, Jonathan Denlinger, Alexei Fedorov, Haitao Yang, Wenhui Duan, Hong Yao, Yang Wu, Shoushan Fan, Haijun Zhang, Xi Chen, and Shuyun Zhou. Experimental Observation of Topological Fermi Arcs in Type-II Weyl Semimetal $MoTe_2$. *Nature Physics*, 12(12):1105–1110, sep 2016.

[122] Lunan Huang, Timothy M. McCormick, Masayuki Ochi, Zhiying Zhao, Michi-To Suzuki, Ryotaro Arita, Yun Wu, Daixiang Mou, Huibo Cao, Jiaqiang Yan, Nandini Trivedi, and Adam Kaminski. Spectroscopic Evidence for a Type-II Weyl Semimetallic State in $MoTe_2$. *Nature Materials*, 15(11):1155–1160, jul 2016.

[123] A. Liang, J. Huang, S. Nie, Y. Ding, Q. Gao, C. Hu, S. He, Y. Zhang, C. Wang, B. Shen, J. Liu, P. Ai, L. Yu, X. Sun, W. Zhao, S. Lv, D. Liu, C. Li, Y. Zhang, Y. Hu, Y. Xu, L. Zhao, G. Liu, Z. Mao, X. Jia, F. Zhang, S. Zhang, F. Yang, Z. Wang, Q. Peng, H. Weng, X. Dai, Z. Fang, Z. Xu, C. Chen, and X. J. Zhou. Electronic Evidence for Type II Weyl Semimetal State in $MoTe_2$. April 2016.

[124] Zhen Wang, Yi Zheng, Zhixuan Shen, Yunhao Lu, Hanyan Fang, Feng Sheng, Yi Zhou, Xiaojun Yang, Yupeng Li, Chunmu Feng, and Zhu-An Xu. Helicity-protected ultrahigh mobility Weyl fermions in NbP. *Phys. Rev. B*, 93:121112, Mar 2016.

[125] J. Jiang, Z.K. Liu, Y. Sun, H.F. Yang, C.R. Rajamathi, Y.P. Qi, L.X. Yang, C. Chen, H. Peng, C-C. Hwang, S.Z. Sun, S-K. Mo, I. Vobornik, J. Fujii, S.S.P. Parkin, C. Felser, B.H. Yan, and Y.L. Chen. Signature of type-II weyl semimetal phase in MoTe2. *Nat. Commun.*, 8:13973, jan 2017.

[126] S. Thirupathaiah, I. Morozov, Y. Kushnirenko, A. V. Fedorov, E. Haubold, T. K. Kim, G. Shipunov, A. Maksutova, O. Kataeva, S. Aswartham, B. Büchner, and

S. V. Borisenko. Spectroscopic evidence of topological phase transition in 3D Dirac semimetal $Cd_3(As_{1-x}P_x)_2$. *ArXiv e-prints*, February 2018.

[127] Guoqing Chang, Benjamin J. Wieder, Frank Schindler, Daniel S. Sanchez, Ilya Belopolski, Shin-Ming Huang, Bahadur Singh, Di Wu, Tay-Rong Chang, Titus Neupert, Su-Yang Xu, Hsin Lin, and M. Zahid Hasan. Topological quantum properties of chiral crystals. *Nature Materials*, 17(11):978–985, oct 2018.

[128] Chetan Nayak, Steven H. Simon, Ady Stern, Michael Freedman, and Sankar Das Sarma. Non-abelian anyons and topological quantum computation. *Rev. Mod. Phys.*, 80:1083–1159, Sep 2008.

[129] Roman M. Lutchyn, Jay D. Sau, and S. Das Sarma. Majorana fermions and a topological phase transition in semiconductor-superconductor heterostructures. *Phys. Rev. Lett.*, 105:077001, Aug 2010.

[130] Tudor D. Stanescu, editor. *Introduction to Topological Quantum Matter & Quantum Computation*. CRC Press, dec 2016.

[131] E. Haubold, K. Koepernik, D. Efremov, S. Khim, A. Fedorov, Y. Kushnirenko, J. van den Brink, S. Wurmehl, B. Büchner, T. K. Kim, M. Hoesch, K. Sumida, K. Taguchi, T. Yoshikawa, A. Kimura, T. Okuda, and S. V. Borisenko. Experimental realization of type-II Weyl state in noncentrosymmetric $TaIrTe_4$. *Phys. Rev. B*, 95:241108, Jun 2017.

[132] Masatoshi Sato and Satoshi Fujimoto. Topological phases of noncentrosymmetric superconductors: Edge states, majorana fermions, and non-abelian statistics. *Phys. Rev. B*, 79:094504, Mar 2009.

[133] Dmitry A. Pshenay-Severin and Alexander T. Burkov. Electronic structure of b20 (FeSi-type) transition-metal monosilicides. *Materials*, 12(17):2710, aug 2019.

[134] Zhicheng Rao, Hang Li, Tiantian Zhang, Shangjie Tian, Chenghe Li, Binbin Fu, Cenyao Tang, Le Wang, Zhilin Li, Wenhui Fan, Jiajun Li, Yaobo Huang, Zhehong Liu, Youwen Long, Chen Fang, Hongming Weng, Youguo Shi, Hechang Lei, Yujie Sun, Tian Qian, and Hong Ding. Observation of unconventional chiral fermions with long fermi arcs in CoSi. *Nature*, 567(7749):496–499, mar 2019.

[135] Chandra Shekhar. Chirality meets topology. *Nature Materials*, 17(11):953–954, oct 2018.

[136] Daniel S. Sanchez, Ilya Belopolski, Tyler A. Cochran, Xitong Xu, Jia-Xin Yin, Guoqing Chang, Weiwei Xie, Kaustuv Manna, Vicky Süß, Cheng-Yi Huang, Nasser Alidoust, Daniel Multer, Songtian S. Zhang, Nana Shumiya, Xirui Wang, Guang-Qiang Wang, Tay-Rong Chang, Claudia Felser, Su-Yang Xu, Shuang Jia, Hsin Lin, and M. Zahid Hasan. Topological chiral crystals with helicoid-arc quantum states. *Nature*, 567(7749):500–505, mar 2019.

[137] Yihao Yang, Hong xiang Sun, Jian ping Xia, Haoran Xue, Zhen Gao, Yong Ge, Ding Jia, Shou qi Yuan, Yidong Chong, and Baile Zhang. Topological triply degenerate point with double fermi arcs. *Nat. Phys.*, 15(7):645–649, apr 2019.

[138] Niels B. M. Schröter, Ding Pei, Maia G. Vergniory, Yan Sun, Kaustuv Manna, Fernando de Juan, Jonas. A. Krieger, Vicky Süss, Marcus Schmidt, Pavel Dudin, Barry Bradlyn, Timur K. Kim, Thorsten Schmitt, Cephise Cacho, Claudia Felser, Vladimir N. Strocov, and Yulin Chen. Chiral topological semimetal with multifold band crossings and long fermi arcs. *Nat. Phys.*, 15(8):759–765, may 2019.

[139] Yan Sun, Shu-Chun Wu, and Binghai Yan. Topological surface states and Fermi arcs of the noncentrosymmetric Weyl semimetals TaAs, TaP, NbAs, and NbP. *Phys. Rev. B*, 92:115428, Sep 2015.

[140] Castor Fu, M. P. C. M. Krijn, and S. Doniach. Electronic structure and optical properties of FeSi, a strongly correlated insulator. *Physical Review B*, 49(3):2219–2222, jan 1994.

[141] C.-H. Park, Z.-X. Shen, A. G. Loeser, D. S. Dessau, D. G. Mandrus, A. Migliori, J. Sarrao, and Z. Fisk. Direct observation of a narrow band near the gap edge of FeSi. *Phys. Rev. B*, 52(24):R16981–R16984, dec 1995.

[142] M. A. Chernikov, L. Degiorgi, E. Felder, S. Paschen, A. D. Bianchi, H. R. Ott, J. L. Sarrao, Z. Fisk, and D. Mandrus. Low-temperature transport, optical, magnetic and thermodynamic properties of $Fe_{1-x}Co_xSi$. *Phys. Rev. B*, 56:1366–1375, Jul 1997.

[143] K. Ishizaka, T. Kiss, T. Shimojima, T. Yokoya, T. Togashi, S. Watanabe, C. Q. Zhang, C. T. Chen, Y. Onose, Y. Tokura, and S. Shin. Ultraviolet laser photoemission spectroscopy of FeSi: Observation of a gap opening in density of states. *Phys. Rev. B*, 72(23), dec 2005.

[144] M. Klein, D. Zur, D. Menzel, J. Schoenes, K. Doll, J. Röder, and F. Reinert. Evidence for Itineracy in the Anticipated Kondo Insulator FeSi: A Quantitative Determination of the Band Renormalization. *Phys. Rev. Lett.*, 101:046406, Jul 2008.

[145] M. Arita, K. Shimada, Y. Takeda, M. Nakatake, H. Namatame, M. Taniguchi, H. Negishi, T. Oguchi, T. Saitoh, A. Fujimori, and T. Kanomata. Angle-resolved photoemission study of the strongly correlated semiconductor FeSi. *Phys. Rev. B*, 77(20), may 2008.

[146] Y. N. Zhao, H. L. Han, Y. Yu, W. H. Xue, and T. Gao. First-principles studies of the electronic and dynamical properties of monosilicides MSi (M = Fe, Ru, Os), journal = EPL (Europhysics Letters). 85(4):47005, feb 2009.

[147] Alla E. Petrova, Vladimir N. Krasnorussky, Anatoly A. Shikov, William M. Yuhasz, Thomas A. Lograsso, Jason C. Lashley, and Sergei M. Stishov. Elastic, thermodynamic, and electronic properties of MnSi, FeSi, and CoSi. *Phys. Rev. B*, 82:155124, Oct 2010.

[148] Brian C. Sales, Olivier Delaire, Michael A. McGuire, and Andrew F. May. Thermoelectric properties of Co-, Ir-, and Os-doped FeSi alloys: Evidence for strong electron-phonon coupling. *Phys. Rev. B*, 83:125209, Mar 2011.

[149] Paromita Dutta and Sudhir K. Pandey. Investigating the electronic structure of MSi (M = Cr, Mn, Fe & Co) and calculating U & J by using cDFT. *Comput. Condens. Matter*, 16:e00325, sep 2018.

[150] V. Jaccarino, G. K. Wertheim, J. H. Wernick, L. R. Walker, and Sigurds Arajs. Paramagnetic Excited State of FeSi. *Phys. Rev.*, 160:476–482, Aug 1967.

[151] Yoshinori Takahashi and Tôru Moriya. A theory of nearly ferromagnetic semiconductors. *Journal of the Physical Society of Japan*, 46(5):1451–1459, may 1979.

[152] Yoshinori Takahashi. Theory of magnetization process of FeSi. *J Phys : Condens Matter*, 10(41):L671–L676, oct 1998.

[153] N. E. Sluchanko, V. V. Glushkov, S. V. Demishev, A. A. Menovsky, L. Weckhuysen, and V. V. Moshchalkov. Crossover in magnetic properties of FeSi. *Phys. Rev. B*, 65:064404, Jan 2002.

[154] Z. Schlesinger, Z. Fisk, Hai-Tao Zhang, M. B. Maple, J. DiTusa, and G. Aeppli. Unconventional charge gap formation in FeSi. *Phys. Rev. Lett.*, 71(11):1748–1751, sep 1993.

[155] Yuankan Fang, Sheng Ran, Weiwei Xie, Shen Wang, Ying Shirley Meng, and M. Brian Maple. Evidence for a conducting surface ground state in high-quality single crystalline FeSi. *PNAS*, 115(34):8558–8562, aug 2018.

[156] J. M. Tomczak, K. Haule, and G. Kotliar. Signatures of electronic correlations in iron silicide. *Proceedings of the National Academy of Sciences*, 109(9):3243–3246, feb 2012.

[157] O. Delaire, K. Marty, M. B. Stone, P. R. C. Kent, M. S. Lucas, D. L. Abernathy, D. Mandrus, and B. C. Sales. Phonon softening and metallization of a narrow-gap semiconductor by thermal disorder. *Proceedings of the National Academy of Sciences*, 108(12):4725–4730, mar 2011.

[158] S N Evangelou and D M Edwards. Temperature-induced local moments in MnSi and FeSi. *J. Phys. C: Solid State Phys.*, 16(11):2121–2131, apr 1983.

[159] Yoshinori Takahashi. Spin-fluctuation theory of FeSi. *J. Phys.: Condens. Matter*, 9(12):2593–2605, mar 1997.

[160] J. Kübler, B. Yan, and C. Felser. Non-vanishing berry phase in chiral insulators. *EPL (Europhysics Letters)*, 104(3):30001, nov 2013.

[161] A. Damascelli, K. Schulte, D. van der Marel, and A. A. Menovsky. Infrared spectroscopic study of phonons coupled to charge excitations in FeSi. *Phys. Rev. B*, 55:R4863–R4866, Feb 1997.

[162] B. C. Sales, E. C. Jones, B. C. Chakoumakos, J. A. Fernandez-Baca, H. E. Harmon, J. W. Sharp, and E. H. Volckmann. Magnetic, transport, and structural properties of $Fe_{1-x}Ir_xSi$. *Phys. Rev. B*, 50:8207–8213, Sep 1994.

[163] S. V. Borisenko. "one-cubed" arpes user facility at bessy ii. *Synchrotron Radiation News*, 25(5):6–11, 2012.

[164] S. V. Borisenko, V. B. Zabolotnyy, D. V. Evtushinsky, T. K. Kim, I. V. Morozov, A. N. Yaresko, A. A. Kordyuk, G. Behr, A. Vasiliev, R. Follath, and B. Büchner. *J. Vis. Exp.*, 68:e50129, 2012.

[165] P. Samuely, P. Szabó, M. Mihalik, N. Hudáková, and A.A. Menovsky. Gap formation in kondo insulator FeSi: Point contact spectroscopy. *Physica B*, 218(1-4):185–188, feb 1996.

[166] B. Buschinger, C. Geibel, F. Steglich, D. Mandrus, D. Young, J.L. Sarrao, and Z. Fisk. Transport properties of FeSi. *Physica B: Condensed Matter*, 230-232:784–786, feb 1997.

[167] S. Paschen, E. Felder, M. A. Chernikov, L. Degiorgi, H. Schwer, H. R. Ott, D. P. Young, J. L. Sarrao, and Z. Fisk. Low-temperature transport, thermodynamic, and optical properties of fesi. *Phys. Rev. B*, 56:12916–12930, Nov 1997.

[168] M. Fäth, J. Aarts, A. A. Menovsky, G. J. Nieuwenhuys, and J. A. Mydosh. Tunneling spectroscopy on the correlation effects in FeSi. *Phys. Rev. B*, 58:15483–15490, Dec 1998.

[169] S. Thirupathaiah, S. de Jong, R. Ovsyannikov, H. A. Dürr, A. Varykhalov, R. Follath, Y. Huang, R. Huisman, M. S. Golden, Yu-Zhong Zhang, H. O. Jeschke, R. Valentí, A. Erb, A. Gloskovskii, and J. Fink. Orbital character variation of the Fermi surface and doping dependent changes of the dimensionality in $BaFe_{2-x}Co_xAs_2$ from angle-resolved photoemission spectroscopy. *Phys. Rev. B*, 81(10):104512, Mar 2010.

[170] T. Valla, A. V. Fedorov, P. D. Johnson, and S. L. Hulbert. Many-Body Effects in Angle-Resolved Photoemission: Quasiparticle Energy and Lifetime of a Mo(110) Surface State. *Phys. Rev. Lett.*, 83:2085–2088, Sep 1999.

[171] A.-M. Racu, D. Menzel, J. Schoenes, and K. Doll. Crystallographic disorder and electron-phonon coupling in $Fe_{1-x}Co_xSi$ single crystals: Raman spectroscopy study. *Phys. Rev. B*, 76:115103, Sep 2007.

[172] D. Menzel, P. Popovich, N. N. Kovaleva, J. Schoenes, K. Doll, and A. V. Boris. Electron-phonon interaction and spectral weight transfer in $Fe_{1-x}Co_xSi$. *Phys. Rev. B*, 79:165111, Apr 2009.

[173] Niels B. M. Schröter, Samuel Stolz, Kaustuv Manna, Fernando de Juan, Maia G. Vergniory, Jonas A. Krieger1, Ding Pei, Pavel Dudin, Timur K. Kim, Cephise Cacho, Barry Bradlyn, Horst Borrmann, Marcus Schmidt, Roland Widmer, Vladimir

Strokov, and Claudia Felser. Observation and manipulation of maximal Chern numbers in the chiral topological semimetal PdGa. Jul 2019.

[174] Yan Sun, Shu-Chun Wu, Mazhar N. Ali, Claudia Felser, and Binghai Yan. Prediction of Weyl Semimetal in Orthorhombic $MoTe_2$. *Phys. Rev. B*, 92:161107, Oct 2015.

[175] Chenlu Wang, Yan Zhang, Jianwei Huang, Simin Nie, Guodong Liu, Aiji Liang, Yuxiao Zhang, Bing Shen, Jing Liu, Cheng Hu, Ying Ding, Defa Liu, Yong Hu, Shaolong He, Lin Zhao, Li Yu, Jin Hu, Jiang Wei, Zhiqiang Mao, Youguo Shi, Xiaowen Jia, Fengfeng Zhang, Shenjin Zhang, Feng Yang, Zhimin Wang, Qinjun Peng, Hongming Weng, Xi Dai, Zhong Fang, Zuyan Xu, Chuangtian Chen, and X. J. Zhou. Observation of Fermi arc and its connection with bulk states in the candidate type-II Weyl semimetal WTe_2. *Phys. Rev. B*, 94:241119, Dec 2016.

[176] Douglas J. Scalapino. The electron-phonon interaction and strong-coupling superconductors. In *Superconductivity*, pages 449–560. Routledge.

[177] G. R. Stewart. Heavy-fermion systems. *Rev. Mod. Phys.*, 56:755–787, Oct 1984.

[178] Jinyu Liu, Jin Hu, Huibo Cao, Yanglin Zhu, Alyssa Chuang, D. Graf, D. J. Adams, S. M. A. Radmanesh, L. Spinu, I. Chiorescu, and Zhiqiang Mao. Nearly massless Dirac fermions hosted by Sb square net in $BaMnSb_2$. *Sci. Rep.*, 6(1), jul 2016.

[179] R. A. de Groot, F. M. Mueller, P. G. van Engen, and K. H. J. Buschow. New class of materials: Half-metallic ferromagnets. *Phys. Rev. Lett.*, 50:2024–2027, Jun 1983.

[180] N F Mott. The basis of the electron theory of metals, with special reference to the transition metals. *Proceedings of the Physical Society. Section A*, 62(7):416–422, jul 1949.

[181] T Moriya and Y Takahashi. Itinerant electron magnetism. *Annual Review of Materials Science*, 14(1):1–25, aug 1984.

[182] D. K. C. MacDonald. *Thermoelectricity: An Introduction to the Principles*. Number pp. 1–65. Dover Publications, 2006.

[183] J A Hertz and D M Edwards. Electron-magnon interactions in itinerant ferromagnetism. i. formal theory. *Journal of Physics F: Metal Physics*, 3(12):2174–2190, dec 1973.

[184] D M Edwards and J A Hertz. Electron-magnon interactions in itinerant ferromagnetism. II. strong ferromagnetism. *Journal of Physics F: Metal Physics*, 3(12):2191–2205, dec 1973.

[185] A. Lanzara, P. V. Bogdanov, X. J. Zhou, S. A. Kellar, D. L. Feng, E. D. Lu, T. Yoshida, H. Eisaki, A. Fujimori, K. Kishio, J.-I. Shimoyama, T. Noda, S. Uchida, Z. Hussain, and Z.-X. Shen. Evidence for ubiquitous strong electron–phonon coupling in high-temperature superconductors. *Nature*, 412(6846):510–514, aug 2001.

[186] X.-P. Wang, P. Richard, A. van Roekeghem, Y.-B. Huang, E. Razzol, T. Qian, H.-D. Wang, C.-H. Dong, M.-H. Fang, M. Shi, and H. Ding. Observation of an isotropic superconducting gap at the Brillouin zone center of $Tl_{0.63}K_{0.37}Fe_{1.78}Se_2$. *EPL*, 99:67001, 2012.

[187] J. van Elp, J. L. Wieland, H. Eskes, P. Kuiper, G. A. Sawatzky, F. M. F. de Groot, and T. S. Turner. Electronic structure of CoO, Li-doped CoO, and $LiCoO_2$. *Phys. Rev. B*, 44:6090–6103, Sep 1991.

[188] I. Terasaki, Y. Sasago, and K. Uchinokura. Large thermoelectric power in $NaCo_2O_4$ single crystals. *Phys. Rev. B*, 56:R12685–R12687, Nov 1997.

[189] J. Sugiyama, H. Nozaki, Y. Ikedo, K. Mukai, J. H. Brewer, E. J. Ansaldo, G. D. Morris, D. Andreica, A. Amato, T. Fujii, and A. Asamitsu. Static Magnetic Order in Metallic $K_{0.49}CoO_2$. *Phys. Rev. Lett.*, 96:037206, Jan 2006.

[190] S Shibasaki, T Nakano, I Terasaki, K Yubuta, and T Kajitani. Transport properties of the layered Rh oxide $K_{0.49}RhO_2$. *J. Phys.: Condens. Matter*, 22(11):115603, mar 2010.

[191] Raymond Schaak, Tomasz Klimczuk, M Foo, and R Cava. Superconductivity Phase Diagram of $Na_xCoO_2.1.3H_2O$. *Nature*, 424:527–9, 08 2003.

[192] Minhyea Lee, Liliana Viciu, Lu Li, Yayu Wang, M Foo, S Watauchi, Robert Pascal, R Cava, and N Ong. Large Enhancement of the Thermopower in Na_xCoO_2 at High Na Doping. *Nature Materials*, 5:537–40, 07 2006.

[193] L. M. Helme, A. T. Boothroyd, R. Coldea, D. Prabhakaran, D. A. Tennant, A. Hiess, and J. Kulda. Three-Dimensional Spin Fluctuations in $Na_{0.75}CoO_2$. *Phys. Rev. Lett.*, 94:157206, Apr 2005.

[194] S. P. Bayrakci, I. Mirebeau, P. Bourges, Y. Sidis, M. Enderle, J. Mesot, D. P. Chen, C. T. Lin, and B. Keimer. Magnetic Ordering and Spin Waves in $Na_{0.82}CoO_2$. *Phys. Rev. Lett.*, 94:157205, Apr 2005.

[195] Maw Lin Foo, Yayu Wang, Satoshi Watauchi, H. W. Zandbergen, Tao He, R. J. Cava, and N. P. Ong. Charge Ordering, Commensurability, and Metallicity in the Phase Diagram of the Layered Na_xCoO_2. *Phys. Rev. Lett.*, 92:247001, Jun 2004.

[196] R. Okazaki, Y. Nishina, Y. Yasui, S. Shibasaki, and I. Terasaki. Optical study of the electronic structure and correlation effects in $K_{0.49}RhO_2$. *Phys. Rev. B*, 84:075110, Aug 2011.

[197] W. Koshibae and S. Maekawa. Effects of Spin and Orbital Degeneracy on the Thermopower of Strongly Correlated Systems. *Phys. Rev. Lett.*, 87:236603, Nov 2001.

[198] Yayu Wang, Nyrissa Rogado, R Cava, and N Ong. Spin Entropy as the Likely Source of Enhanced Thermopower in $Na_xCo_2O_4$. *Nature*, 423:425–8, 06 2003.

[199] A. Donkov, M. M. Korshunov, I. Eremin, P. Lemmens, V. Gnezdilov, F. C. Chou, and C. T. Lin. Electron-phonon interaction in the lamellar cobaltate Na_xCoO_2. *Phys. Rev. B*, 77:100504, Mar 2008.

[200] S. H. Yao, B. B. Zhang, J. Zhou, Y. B. Chen, S. T. Zhang, Z. B. Gu, S. T. Dong, and Y. F. Chen. Structure and physical properties of $K_{0.63}RhO_2$ single crystals. *AIP Adv.*, 2(4):042140, 2012.

[201] M. Z. Hasan, Y.-D. Chuang, D. Qian, Y. W. Li, Y. Kong, A. Kuprin, A. V. Fedorov, R. Kimmerling, E. Rotenberg, K. Rossnagel, Z. Hussain, H. Koh, N. S. Rogado, M. L. Foo, and R. J. Cava. Fermi Surface and Quasiparticle Dynamics of $Na_{0.7}CoO_2$ Investigated by Angle-Resolved Photoemission Spectroscopy. *Phys. Rev. Lett.*, 92:246402, Jun 2004.

[202] H.-B. Yang, Z.-H. Pan, A. K. P. Sekharan, T. Sato, S. Souma, T. Takahashi, R. Jin, B. C. Sales, D. Mandrus, A. V. Fedorov, Z. Wang, and H. Ding. Fermi Surface Evolution and Luttinger Theorem in Na_xCoO_2: A Systematic Photoemission Study. *Phys. Rev. Lett.*, 95:146401, Sep 2005.

[203] T Arakane, T Sato, T Takahashi, T Fujii, and A Asamitsu. Angle-resolved photoemission study of the doping evolution of a three-dimensional Fermi surface in Na_xCoO_2. *New J. Phys.*, 13(4):043021, apr 2011.

[204] Y. Okamoto, R. Matsumoto, T. Yagihara, C. Iwai, K. Miyoshi, J. Takeuchi, K. Horiba, M. Kobayashi, K. Ono, H. Kumigashira, N. L. Saini, and T. Mizokawa. Electronic structure and polar catastrophe at the surface of Li_xCoO_2 studied by angle-resolved photoemission spectroscopy. *Phys. Rev. B*, 96:125147, Sep 2017.

[205] Su-Di Chen, Yu He, Alfred Zong, Yan Zhang, Makoto Hashimoto, Bin-Bin Zhang, Shu-Hua Yao, Yan-Bin Chen, Jian Zhou, Yan-Feng Chen, Sung-Kwan Mo, Zahid Hussain, Donghui Lu, and Zhi-Xun Shen. Large thermopower from dressed quasiparticles in the layered cobaltates and rhodates. *Phys. Rev. B*, 96:081109, Aug 2017.

[206] Paolo Giannozzi, Stefano Baroni, Nicola Bonini, Matteo Calandra, Roberto Car, Carlo Cavazzoni, Davide Ceresoli, Guido L Chiarotti, Matteo Cococcioni, Ismaila Dabo, Andrea Dal Corso, Stefano de Gironcoli, Stefano Fabris, Guido Fratesi, Ralph Gebauer, Uwe Gerstmann, Christos Gougoussis, Anton Kokalj, Michele Lazzeri, Layla Martin-Samos, Nicola Marzari, Francesco Mauri, Riccardo Mazzarello, Stefano Paolini, Alfredo Pasquarello, Lorenzo Paulatto, Carlo Sbraccia, Sandro Scandolo, Gabriele Sclauzero, Ari P Seitsonen, Alexander Smogunov, Paolo Umari, and Renata M Wentzcovitch. QUANTUM ESPRESSO: A Modular and Open-source Software Project for Quantum Simulations of Materials. *J. Phys.: Condens. Matter*, 21(39):395502 (19pp), 2009.

[207] D. J. Singh. Electronic structure of $NaCo_2O_4$. *Phys Rev B*, 61:13397–13402, May 2000.

[208] F. Reinert and S. Hüfner. Photoemission Spectroscopy with Very High Energy Resolution: Studying the Influence of Electronic Correlations on the Millielectronvolt Scale. In *Very High Resolution Photoelectron Spectroscopy*, pages 13–53. Springer Berlin Heidelberg.

[209] A. Nicolaou, V. Brouet, M. Zacchigna, I. Vobornik, A. Tejeda, A. Taleb-Ibrahimi, P. Le Fèvre, F. Bertran, S. Hébert, H. Muguerra, and D. Grebille. Experimental Study of the Incoherent Spectral Weight in the Photoemission Spectra of the Misfit Cobaltate $[Bi_2Ba_2\mathbf{O}_4][CoO_2]_2$. *Phys. Rev. Lett.*, 104:056403, Feb 2010.

[210] J. Fink, S. Borisenko, A. Kordyuk, A. Koitzsch, J. Geck, V. Zabolotnyy, M. Knupfer, B. Büchner, and H. Berger. Dressing of the Charge Carriers in High-T_c Superconductors. In Hüfner S. (eds), editor, *Very High Resolution Photoelectron Spectroscopy*, pages 295–325. Springer Berlin Heidelberg, 2007.

[211] J. Geck, S. V. Borisenko, H. Berger, H. Eschrig, J. Fink, M. Knupfer, K. Koepernik, A. Koitzsch, A. A. Kordyuk, V. B. Zabolotnyy, and B. Büchner. Anomalous Quasiparticle Renormalization in $Na_{0.73}CoO_2$: Role of Interorbital Interactions and Magnetic Correlations. *Phys. Rev. Lett.*, 99:046403, Jul 2007.

[212] J. M. Luttinger. Fermi surface and some simple equilibrium properties of a system of interacting fermions. *Phys. Rev.*, 119:1153–1163, Aug 1960.

[213] P. Zhang, T. Qian, P. Richard, X. P. Wang, H. Miao, B. Q. Lv, B. B. Fu, T. Wolf, C. Meingast, X. X. Wu, Z. Q. Wang, J. P. Hu, and H. Ding. Observation of two distinct d_{xz}/d_{yz} band splittings in fese. *Phys. Rev. B*, 91:214503, Jun 2015.

[214] J. Schäfer, D. Schrupp, Eli Rotenberg, K. Rossnagel, H. Koh, P. Blaha, and R. Claessen. Electronic Quasiparticle Renormalization on the Spin Wave Energy Scale. *Phys. Rev. Lett.*, 92:097205, Mar 2004.

[215] Federico Mazzola, Justin W. Wells, Rositza Yakimova, Søren Ulstrup, Jill A. Miwa, Richard Balog, Marco Bianchi, Mats Leandersson, Johan Adell, Philip Hofmann, and T. Balasubramanian. Kinks in the σ Band of Graphene Induced by Electron-Phonon Coupling. *Phys. Rev. Lett.*, 111:216806, Nov 2013.

[216] T. Valla, T. E. Kidd, W.-G. Yin, G. D. Gu, P. D. Johnson, Z.-H. Pan, and A. V. Fedorov. High-Energy Kink Observed in the Electron Dispersion of High-Temperature Cuprate Superconductors. *Phys. Rev. Lett.*, 98:167003, Apr 2007.

[217] D. S. Inosov, J. Fink, A. A. Kordyuk, S. V. Borisenko, V. B. Zabolotnyy, R. Schuster, M. Knupfer, B. Büchner, R. Follath, H. A. Dürr, W. Eberhardt, V. Hinkov, B. Keimer, and H. Berger. Momentum and energy dependence of the anomalous high-energy dispersion in the electronic structure of high temperature superconductors. *Phys. Rev. Lett.*, 99:237002, 2007.

[218] Susmita Basak, Tanmoy Das, Hsin Lin, J. Nieminen, M. Lindroos, R. S. Markiewicz, and A. Bansil. Origin of the high-energy kink in the photoemission spectrum of the

high-temperature superconductor $Bi_2Sr_2CaCu_2O_8$. *Phys. Rev. B*, 80:214520, Dec 2009.

[219] E. D. L. Rienks, M. Ärrälä, M. Lindroos, F. Roth, W. Tabis, G. Yu, M. Greven, and J. Fink. High-Energy Anomaly in the Angle-Resolved Photoemission Spectra of $Nd_{2-x}Ce_xCuO_4$: Evidence for a Matrix Element Effect. *Phys. Rev. Lett.*, 113:137001, Sep 2014.

[220] J. Graf, G.-H. Gweon, K. McElroy, S. Y. Zhou, C. Jozwiak, E. Rotenberg, A. Bill, T. Sasagawa, H. Eisaki, S. Uchida, H. Takagi, D.-H. Lee, and A. Lanzara. Universal High Energy Anomaly in the Angle-Resolved Photoemission Spectra of High Temperature Superconductors: Possible Evidence of Spinon and Holon Branches. *Phys. Rev. Lett.*, 98:067004, Feb 2007.

[221] H. W. Ou, J. F. Zhao, Y. Zhang, B. P. Xie, D. W. Shen, Y. Zhu, Z. Q. Yang, J. G. Che, X. G. Luo, X. H. Chen, M. Arita, K. Shimada, H. Namatame, M. Taniguchi, C. M. Cheng, K. D. Tsuei, and D. L. Feng. Novel Electronic Structure Induced by a Highly Strained Oxide Interface with Incommensurate Crystal Fields. *Phys. Rev. Lett.*, 102:026806, Jan 2009.

[222] Bin-Bin Zhang, Song-Tao Dong, Shu-Hua Yao, Y. B. Chen, Shan-Tao Zhang, Zheng-Bin Gu, Jian Zhou, Ming-Hui Lu, Yan-Feng Chen, and Y. G. Shi. Electrical, magnetic, and magneto-electrical properties in quasi-two-dimensional $K_{0.58}RhO_2$ single crystals doped with rare-earth elements. *Appl. Phys. Lett.*, 105(6):062408, 2014.

[223] Manoj Soundhira Pandiyan. *Phase Diagram andControl of Thermoelectric Propertiesof Sodium Cobaltate*. PhD thesis, Department of Physics, University of London, 2013.

[224] D. J. Singh and D. Kasinathan. Thermoelectric Properties of Na_xCoO_2 and Prospects for Other Oxide Thermoelectrics. *J. Electron. Mater.*, 36(7):736–739, jun 2007.

[225] Frank Wilczek. Two applications of axion electrodynamics. *Phys. Rev. Lett.*, 58:1799–1802, May 1987.

[226] Roger S. K. Mong, Andrew M. Essin, and Joel E. Moore. Antiferromagnetic topological insulators. *Phys. Rev. B*, 81:245209, Jun 2010.

[227] Rundong Li, Jing Wang, Xiao-Liang Qi, and Shou-Cheng Zhang. Dynamical axion field in topological magnetic insulators. *Nature Physics*, 6(4):284–288, 2010.

[228] Rui Yu, Wei Zhang, Hai-Jun Zhang, Shou-Cheng Zhang, Xi Dai, and Zhong Fang. Quantized Anomalous Hall Effect in Magnetic Topological Insulators. *Science*, 329(5987):61–64, 2010.

[229] Cui-Zu Chang, Jinsong Zhang, Xiao Feng, Jie Shen, Zuocheng Zhang, Minghua Guo, Kang Li, Yunbo Ou, Pang Wei, Li-Li Wang, Zhong-Qing Ji, Yang Feng, Shuaihua Ji, Xi Chen, Jinfeng Jia, Xi Dai, Zhong Fang, Shou-Cheng Zhang, Ke He, Yayu Wang, Li Lu, Xu-Cun Ma, and Qi-Kun Xue. Experimental Observation of the Quantum Anomalous Hall Effect in a Magnetic Topological Insulator. *Science*, 340(6129):167–170, 2013.

[230] Z. F. Wang, Zheng Liu, and Feng Liu. Quantum Anomalous Hall Effect in 2D Organic Topological Insulators. *Phys. Rev. Lett.*, 110:196801, May 2013.

[231] Xiao-Liang Qi and Shou-Cheng Zhang. Topological insulators and superconductors. *Rev. Mod. Phys.*, 83:1057–1110, Oct 2011.

[232] Haijun Zhang, Jing Wang, Gang Xu, Yong Xu, and Shou-Cheng Zhang. Topological States in Ferromagnetic CdO/EuO Superlattices and Quantum Wells. *Phys. Rev. Lett.*, 112:096804, Mar 2014.

[233] Cui-Zu Chang, Weiwei Zhao, Duk Y Kim, Haijun Zhang, Badih A Assaf, Don Heiman, Shou-Cheng Zhang, Chaoxing Liu, Moses HW Chan, and Jagadeesh S Moodera. High-precision realization of robust quantum anomalous Hall state in a hard ferromagnetic topological insulator. *Nature materials*, 14(5):473–477, 2015.

[234] Ken N Okada, Youtarou Takahashi, Masataka Mogi, Ryutaro Yoshimi, Atsushi Tsukazaki, Kei S Takahashi, Naoki Ogawa, Masashi Kawasaki, and Yoshinori Tokura. Terahertz spectroscopy on Faraday and Kerr rotations in a quantum anomalous Hall state. *Nature communications*, 7(1):12245, 2016.

[235] Yoshinori Tokura, Kenji Yasuda, and Atsushi Tsukazaki. Magnetic topological insulators. *Nature Reviews Physics*, 1(2):126–143, 2019.

[236] Mikhail M Otrokov, Ilya I Klimovskikh, Hendrik Bentmann, D Estyunin, Alexander Zeugner, Ziya S Aliev, S Gaß, AUB Wolter, AV Koroleva, Alexander M Shikin, et al.

Prediction and observation of an antiferromagnetic topological insulator. *Nature*, 576(7787):416–422, 2019.

[237] Yan Gong, Jingwen Guo, Jiaheng Li, Kejing Zhu, Menghan Liao, Xiaozhi Liu, Qinghua Zhang, Lin Gu, Lin Tang, Xiao Feng, Ding Zhang, Wei Li, Canli Song, Lili Wang, Pu Yu, Xi Chen, Yayu Wang, Hong Yao, Wenhui Duan, Yong Xu, Shou-Cheng Zhang, Xucun Ma, Qi-Kun Xue, and Ke He. Experimental Realization of an Intrinsic Magnetic Topological Insulator. *Chinese Physics Letters*, 36(7):076801, jun 2019.

[238] Alexander Zeugner, Frederik Nietschke, Anja UB Wolter, Sebastian Gaß, Raphael C Vidal, Thiago RF Peixoto, Darius Pohl, Christine Damm, Axel Lubk, Richard Hentrich, et al. Chemical aspects of the candidate antiferromagnetic topological insulator $MnBi_2Te_4$. *Chemistry of Materials*, 31(8):2795–2806, 2019.

[239] Seng Huat Lee, Yanglin Zhu, Yu Wang, Leixin Miao, Timothy Pillsbury, Hemian Yi, Susan Kempinger, Jin Hu, Colin A. Heikes, P. Quarterman, William Ratcliff, Julie A. Borchers, Heda Zhang, Xianglin Ke, David Graf, Nasim Alem, Cui-Zu Chang, Nitin Samarth, and Zhiqiang Mao. Spin scattering and noncollinear spin structure-induced intrinsic anomalous Hall effect in antiferromagnetic topological insulator $MnBi_2Te_4$. *Phys. Rev. Research*, 1:012011, Aug 2019.

[240] Dongqin Zhang, Minji Shi, Tongshuai Zhu, Dingyu Xing, Haijun Zhang, and Jing Wang. Topological Axion States in the Magnetic Insulator $MnBi_2Te_4$ with the Quantized Magnetoelectric Effect. *Phys. Rev. Lett.*, 122:206401, May 2019.

[241] J.-Q. Yan, Q. Zhang, T. Heitmann, Zengle Huang, K. Y. Chen, J.-G. Cheng, Weida Wu, D. Vaknin, B. C. Sales, and R. J. McQueeney. Crystal growth and magnetic structure of $MnBi_2Te_4$. *Phys. Rev. Materials*, 3:064202, Jun 2019.

[242] Yu-Jie Hao, Pengfei Liu, Yue Feng, Xiao-Ming Ma, Eike F. Schwier, Masashi Arita, Shiv Kumar, Chaowei Hu, Rui'e Lu, Meng Zeng, Yuan Wang, Zhanyang Hao, Hong-Yi Sun, Ke Zhang, Jiawei Mei, Ni Ni, Liusuo Wu, Kenya Shimada, Chaoyu Chen, Qihang Liu, and Chang Liu. Gapless Surface Dirac Cone in Antiferromagnetic Topological Insulator $MnBi_2Te_4$. *Phys. Rev. X*, 9:041038, Nov 2019.

[243] Y. J. Chen, L. X. Xu, J. H. Li, Y. W. Li, H. Y. Wang, C. F. Zhang, H. Li, Y. Wu, A. J. Liang, C. Chen, S. W. Jung, C. Cacho, Y. H. Mao, S. Liu, M. X. Wang,

Y. F. Guo, Y. Xu, Z. K. Liu, L. X. Yang, and Y. L. Chen. Topological Electronic Structure and Its Temperature Evolution in Antiferromagnetic Topological Insulator $MnBi_2Te_4$. *Phys. Rev. X*, 9:041040, Nov 2019.

[244] Jiazhen Wu and Fucai Liu and Masato Sasase and Koichiro Ienaga and Yukiko Obata and Ryu Yukawa and Koji Horiba and Hiroshi Kumigashira and Satoshi Okuma and Takeshi Inoshita and Hideo Hosono . Natural van der waals heterostructural single crystals with both magnetic and topological properties. *Science Advances*, 5(11):eaax9989, 2019.

[245] Jiaheng Li, Chong Wang, Zetao Zhang, Bing-Lin Gu, Wenhui Duan, and Yong Xu. Magnetically controllable topological quantum phase transitions in the antiferromagnetic topological insulator $MnBi_2Te_4$. *Phys. Rev. B*, 100:121103, Sep 2019.

[246] J.-Q. Yan, Zengle Huang, Weida Wu, and A.F. May. Vapor transport growth of $MnBi_2Te_4$ and related compounds. *Journal of Alloys and Compounds*, 906:164327, 2022.

[247] Hao Li, Shengsheng Liu, Chang Liu, Jinsong Zhang, Yong Xu, Rong Yu, Yang Wu, Yuegang Zhang, and Shoushan Fan. Antiferromagnetic topological insulator $MnBi_2Te_4$: synthesis and magnetic properties. *Phys. Chem. Chem. Phys.*, 22:556–563, 2020.

[248] Alexander Zeugner, Frederik Nietschke, Anja UB Wolter, Sebastian Gaß, Raphael C Vidal, Thiago RF Peixoto, Darius Pohl, Christine Damm, Axel Lubk, Richard Hentrich, et al. Chemical aspects of the candidate antiferromagnetic topological insulator $MnBi_2Te_4$. *Chem. Mater.*, 31(8):2795–2806, 2019.

[249] OrujluE. Phase equilibria in the SnBi2Te4-MnBi2Te4 system and characterization of the $Sn_{1-x}Mn_xBi_2Te_4$ solid solutions. *Physics and Chemistry of Solid State*, 21(1):113–116, Mar. 2020.

[250] Mujeeb Ahmad, Khushboo Agarwal, and B. R. Mehta. An anomalously high Seebeck coefficient and power factor in ultrathin Bi_2Te_3 film: Spin–orbit interaction. *Journal of Applied Physics*, 128(3):035108, 2020.

[251] Pei-Yu Chuang, Shu-Hsuan Su, Cheong-Wei Chong, Yi-Fan Chen, Yu-Heng Chou, Jung-Chun-Andrew Huang, Wei-Chuan Chen, Cheng-Maw Cheng, Ku-Ding Tsuei,

Chia-Hsin Wang, Yaw-Wen Yang, Yen-Fa Liao, Shih-Chang Weng, Jyh-Fu Lee, Yi-Kang Lan, Shen-Lin Chang, Chi-Hsuan Lee, Chih-Kai Yang, Hai-Lin Su, and Yu-Cheng Wu. Anti-site defect effect on the electronic structure of a Bi_2Te_3 topological insulator. *RSC Adv.*, 8:423–428, 2018.

[252] V.S. Neudachina, T.B. Shatalova, V.I. Shtanov, L.V. Yashina, T.S. Zyubina, M.E. Tamm, and S.P. Kobeleva. Xps study of snte(100) oxidation by molecular oxygen. *Surface Science*, 584(1):77–82, 2005. Selected papers of the Fifth Nordic Conference on Surface Science (NCSS-5).

[253] R.J Iwanowski, M.H Heinonen, and E Janik. X-ray photoelectron spectra of zinc-blende mnte. *Chemical Physics Letters*, 387(1):110–115, 2004.

[254] Fei Jiao, Jingfeng Wang, Xianyu Wang, Qingyin Tian, Meixia Chang, Lingbo Cai, Shu Zhu, Di Zhang, Qing Lu, Cao Wang, et al. The layer-inserting growth of antiferromagnetic topological insulator $MnBi_2Te_4$ based on symmetry and its x-ray photoelectron spectroscopy. *Journal of Superconductivity and Novel Magnetism*, 34(5):1485–1493, 2021.

[255] LC Wang, QY Dong, J Lu, XP Shao, ZJ Mo, ZY Xu, JR Sun, FX Hu, and BG Shen. Low-temperature large magnetocaloric effect in the antiferromagnetic CeSi compound. *Journal of alloys and compounds*, 587:10–13, 2014.

[256] G. Narsinga Rao, Viveka Nand Singh, R. Sankar, I. Panneer Muthuselvam, Guang-Yu Guo, and F. C. Chou. Antiferromagnetism of Ni_2NbBO_6 with $S = 1$ dimer quasi-one-dimensional armchair chains. *Phys. Rev. B*, 91:014423, Jan 2015.

[257] Bo Chen, Fucong Fei, Dongqin Zhang, Bo Zhang, Wanling Liu, Shuai Zhang, Pengdong Wang, Boyuan Wei, Yong Zhang, Zewen Zuo, et al. Intrinsic magnetic topological insulator phases in the Sb doped $MnBi_2Te_4$ bulks and thin flakes. *Nature communications*, 10(1):1–8, 2019.

[258] Jiejun Zhu, Muhammad Naveed, Bo Chen, Yu Du, Jingwen Guo, Hangkai Xie, and Fucong Fei. Magnetic and electrical transport study of the antiferromagnetic topological insulator Sn-doped $MnBi_2Te_4$. *Phys. Rev. B*, 103:144407, Apr 2021.

[259] J.-Q. Yan, S. Okamoto, M. A. McGuire, A. F. May, R. J. McQueeney, and B. C. Sales. Evolution of structural, magnetic, and transport properties in $MnBi_{2-x}Sb_xTe_4$. *Phys. Rev. B*, 100:104409, Sep 2019.

[260] Aoyu Tan, Valentin Labracherie, Narayan Kunchur, Anja U. B. Wolter, Joaquin Cornejo, Joseph Dufouleur, Bernd Büchner, Anna Isaeva, and Romain Giraud. Metamagnetism of Weakly Coupled Antiferromagnetic Topological Insulators. *Phys. Rev. Lett.*, 124:197201, May 2020.

[261] Tiema Qian, Yueh-Ting Yao, Chaowei Hu, Erxi Feng, Huibo Cao, Igor I. Mazin, Tay-Rong Chang, and Ni Ni. Magnetic dilution effect and topological phase transitions in $(Mn_{1-x}Pb_x)Bi_2Te_4$. *Phys. Rev. B*, 106:045121, Jul 2022.

[262] S. Chakraborty and A. K. Majumdar. Resistivity minima in concentrated γ-$Cu_{100-x}Mn_x$ alloys ($36 \leqslant x \leqslant 83$). *Phys. Rev. B*, 53:6235–6239, Mar 1996.

[263] E. Abrahams, P. W. Anderson, D. C. Licciardello, and T. V. Ramakrishnan. Scaling Theory of Localization: Absence of Quantum Diffusion in Two Dimensions. *Phys. Rev. Lett.*, 42:673–676, Mar 1979.

[264] J. Kondo. Resistance minimum in dilute magnetic alloys. *Prog. Theor. Phys.*, 32:37, 1964.

[265] Hongtao Liu, Lihong Bao, Zhang Zhou, Bingyu Che, Ruizi Zhang, Ce Bian, Ruisong Ma, Liangmei Wu, Haifang Yang, Junjie Li, Changzhi Gu, Cheng-Min Shen, Shixuan Du, and Hong-Jun Gao. Quasi-2D Transport and Weak Antilocalization Effect in Few-layered VSe2. *Nano Letters*, 19(7):4551–4559, 2019. PMID: 31241975.

[266] R. R. Jia, J. C. Zhang, R. K. Zheng, D. M. Deng, H.-U. Habermeier, H. L. W. Chan, H. S. Luo, and S. X. Cao. Effects of ferroelectric-poling-induced strain on the quantum correction to low-temperature resistivity of manganite thin films. *Phys. Rev. B*, 82:104418, Sep 2010.

[267] E. J. Guo, L. Wang, Z. P. Wu, L. Wang, H. B. Lu, K. J. Jin, and J. Gao. Magnetic field mediated low-temperature resistivity upturn in electron-doped $La_{1-x}Hf_xMnO_3$ manganite oxides. *Journal of Applied Physics*, 112(12):123710, 2012.

[268] Christoph Sürgers, Gerda Fischer, Patrick Winkel, and Hilbert V Löhneysen. Large topological hall effect in the non-collinear phase of an antiferromagnet. *Nature communications*, 5(1):3400, 2014.

[269] Jianhua Cui, Mengzhu Shi, Honghui Wang, Fanghang Yu, Tao Wu, Xigang Luo, Jianjun Ying, and Xianhui Chen. Transport properties of thin flakes of the antiferromagnetic topological insulator $MnBi_2Te_4$. *Phys. Rev. B*, 99:155125, Apr 2019.

[270] Bryan Kuropatwa and Holger Kleinke. Thermoelectric Properties of Stoichiometric Compounds in the $(SnTe)_x(Bi_2Te_3)_y$ System. *Zeitschrift für anorganische und allgemeine Chemie*, 638:2640–2647, 12 2012.

[271] Yi-Chao Zou, Zhi-Gang Chen, Enze Zhang, Fantai Kong, Yan Lu, Lihua Wang, John Drennan, Zhongchang Wang, Faxian Xiu, Kyeongjae Cho, et al. Atomic disorders in layer structured topological insulator $SnBi_2Te_4$ nanoplates. *Nano Research*, 11(2):696–706, 2018.

[272] Jang-Yeul Tak, Young Soo Lim, Jae Nyeong Kim, Changhoon Lee, Ji Hoon Shim, Hyung Koun Cho, Cheol-Hee Park, and Won-Seon Seo. Thermoelectric transport properties of tetradymite-type $Pb_{1-x}Sn_xBi_2Te_4$ compounds. *Journal of Alloys and Compounds*, 690:966–970, 2017.

[273] Yu-Jie Hao, Pengfei Liu, Yue Feng, Xiao-Ming Ma, Eike F. Schwier, Masashi Arita, Shiv Kumar, Chaowei Hu, Rui'e Lu, Meng Zeng, Yuan Wang, Zhanyang Hao, Hong-Yi Sun, Ke Zhang, Jiawei Mei, Ni Ni, Liusuo Wu, Kenya Shimada, Chaoyu Chen, Qihang Liu, and Chang Liu. Gapless Surface Dirac Cone in Antiferromagnetic Topological Insulator $MnBi_2Te_4$. *Phys. Rev. X*, 9(4):041038, 2019.

[274] Chenhui Yan, Sebastian Fernandez-Mulligan, Ruobing Mei, Seng Huat Lee, Nikola Protic, Rikuto Fukumori, Binghai Yan, Chaoxing Liu, Zhiqiang Mao, and Shuolong Yang. Origins of electronic bands in the antiferromagnetic topological insulator $MnBi_2Te_4$. *Phys. Rev. B*, 104:L041102, Jul 2021.

[275] D. A. Estyunin, I. I. Klimovskikh, A. M. Shikin, E. F. Schwier, M. M. Otrokov, A. Kimura, S. Kumar, S. O. Filnov, Z. S. Aliev, M. B. Babanly, and E. V. Chulkov. Signatures of temperature driven antiferromagnetic transition in the electronic structure of topological insulator $MnBi_2Te_4$. *APL Materials*, 8(2):021105, 2020.

[276] J. E. Moore and L. Balents. Topological invariants of time-reversal-invariant band structures. *Phys. Rev. B*, 75:121306, Mar 2007.

[277] A. R. Akhmerov, Johan Nilsson, and C. W. J. Beenakker. Electrically detected interferometry of majorana fermions in a topological insulator. *Phys. Rev. Lett.*, 102:216404, May 2009.

[278] Liang Fu and C. L. Kane. Probing neutral majorana fermion edge modes with charge transport. *Phys. Rev. Lett.*, 102:216403, May 2009.

[279] Fang Yang, Lin Miao, Z. F. Wang, Meng-Yu Yao, Fengfeng Zhu, Y. R. Song, Mei-Xiao Wang, Jin-Peng Xu, Alexei V. Fedorov, Z. Sun, G. B. Zhang, Canhua Liu, Feng Liu, Dong Qian, C. L. Gao, and Jin-Feng Jia. Spatial and Energy Distribution of Topological Edge States in Single Bi(111) Bilayer. *Phys. Rev. Lett.*, 109:016801, Jul 2012.

[280] Hsin Lin, L. Andrew Wray, Yuqi Xia, Suyang Xu, Shuang Jia, Robert J. Cava, Arun Bansil, and M. Zahid Hasan. Half-heusler ternary compounds as new multifunctional experimental platforms for topological quantum phenomena. *Nature Materials*, 9(7):546–549, may 2010.

[281] Di Xiao, Yugui Yao, Wanxiang Feng, Jun Wen, Wenguang Zhu, Xing-Qiu Chen, G. Malcolm Stocks, and Zhenyu Zhang. Half-heusler compounds as a new class of three-dimensional topological insulators. *Phys. Rev. Lett.*, 105:096404, Aug 2010.

[282] D. Hsieh, Y. Xia, D. Qian, L. Wray, F. Meier, J. H. Dil, J. Osterwalder, L. Patthey, A. V. Fedorov, H. Lin, A. Bansil, D. Grauer, Y. S. Hor, R. J. Cava, and M. Z. Hasan. Observation of Time-Reversal-Protected Single-Dirac-Cone Topological-Insulator States in Bi_2Te_3 and Sb_2Te_3. *Phys. Rev. Lett.*, 103:146401, Sep 2009.

[283] Xiao-Liang Qi, Taylor L. Hughes, and Shou-Cheng Zhang. Topological field theory of time-reversal invariant insulators. *Phys. Rev. B*, 78:195424, Nov 2008.

[284] Rabia Sultana, Geet Awana, Banabir Pal, PK Maheshwari, Monu Mishra, Govind Gupta, Anurag Gupta, S Thirupathaiah, and VP S. Awana. Electrical, thermal and spectroscopic characterization of Bulk Bi_2Se_3 topological insulator. *Journal of Superconductivity and Novel Magnetism*, 30:2031–2036, 2017.

[285] Rabia Sultana, Ganesh Gurjar, S Patnaik, and VPS Awana. Growth, Characterization and High-Field Magneto-Conductivity of $Co_{0.1}Bi_2Se_3$ Topological Insulator. *Journal of Superconductivity and Novel Magnetism*, 32:769–777, 2019.

[286] Rabia Sultana, Ganesh Gurjar, Bhasker Gahtori, Satyabrata Patnaik, and VPS Awana. Structural, surface morphology and magneto-transport properties of self flux grown Eu doped Bi_2Se_3 single crystal. *Materials Research Express*, 6(9):096107, 2019.

[287] Bao-Tian Wang and Ping Zhang. Phonon spectrum and bonding properties of Bi_2Se_3: Role of strong spin-orbit interaction. *Applied Physics Letters*, 100(8), 2012.

[288] Kushal Mazumder, Alfa Sharma, Yogendra Kumar, and Parasharam M Shirage. Effect of Cu intercalation on humidity sensing properties of Bi_2Se_3 topological insulator single crystals. *Physical Chemistry Chemical Physics*, 20(44):28257–28266, 2018.

[289] A. A. Burkov and Leon Balents. Weyl semimetal in a topological insulator multilayer. *Phys. Rev. Lett.*, 107:127205, Sep 2011.

[290] Xiangang Wan, Ari M. Turner, Ashvin Vishwanath, and Sergey Y. Savrasov. Topological semimetal and fermi-arc surface states in the electronic structure of pyrochlore iridates. *Phys. Rev. B*, 83:205101, May 2011.

[291] Binghai Yan and Claudia Felser. Topological Materials: Weyl Semimetals. *Annu. Rev. Condens. Matter Phys.*, 8(1):337–354, 2017.

[292] N. P. Armitage, E. J. Mele, and Ashvin Vishwanath. Weyl and Dirac semimetals in three-dimensional solids. *Rev. Mod. Phys.*, 90:015001, Jan 2018.

[293] Ajaya K. Nayak, Julia Erika Fischer, Yan Sun, Binghai Yan, Julie Karel, Alexander C. Komarek, Chandra Shekhar, Nitesh Kumar, Walter Schnelle, Jürgen Kübler, Claudia Felser, and Stuart S. P. Parkin. Large anomalous Hall effect driven by a nonvanishing Berry curvature in the noncolinear antiferromagnet Mn_3Ge. *Sci. Adv.*, 2(4):e1501870, 2016.

[294] Naoki Kiyohara, Takahiro Tomita, and Satoru Nakatsuji. Giant Anomalous Hall Effect in the Chiral Antiferromagnet Mn_3Ge. *Phys. Rev. Appl.*, 5:064009, Jun 2016.

[295] Satoru Nakatsuji, Naoki Kiyohara, and Tomoya Higo. Large anomalous Hall effect in a non-collinear antiferromagnet at room temperature. *Nature*, 527(7577):212–215, 2015.

[296] James M. Taylor, Anastasios Markou, Edouard Lesne, Pranava Keerthi Sivakumar, Chen Luo, Florin Radu, Peter Werner, Claudia Felser, and Stuart S. P. Parkin. Anomalous and topological Hall effects in epitaxial thin films of the noncollinear antiferromagnet Mn_3Sn. *Phys. Rev. B*, 101:094404, Mar 2020.

[297] Hideki Narita, Tomoya Higo, Muhammad Ikhlas, Satoru Nakatsuji, and YoshiChika Otani. Effect of sample size on anomalous Nernst effect in chiral antiferromagnetic Mn_3Sn devices. *Appl. Phys. Lett.*, 116(7):072404, 2020.

[298] Hideki Narita, Muhammad Ikhlas, Motoi Kimata, Agustinus Agung Nugroho, Satoru Nakatsuji, and YoshiChika Otani. Anomalous Nernst effect in a micro-fabricated thermoelectric element made of chiral antiferromagnet Mn_3Sn. *Appl. Phys. Lett.*, 111(20):202404, 2017.

[299] Christoph Wuttke, Federico Caglieris, Steffen Sykora, Francesco Scaravaggi, Anja U. B. Wolter, Kaustuv Manna, Vicky Süss, Chandra Shekhar, Claudia Felser, Bernd Büchner, and Christian Hess. Berry curvature unravelled by the anomalous Nernst effect in Mn_3Ge. *Phys. Rev. B*, 100:085111, Aug 2019.

[300] Guang-Yu Guo and Tzu-Cheng Wang. Large anomalous Nernst and spin Nernst effects in the noncollinear antiferromagnets Mn_3X ($X = \mathrm{Sn}, \mathrm{Ge}, \mathrm{Ga}$). *Phys. Rev. B*, 96:224415, Dec 2017.

[301] Xiaokang Li, Liangcai Xu, Linchao Ding, Jinhua Wang, Mingsong Shen, Xiufang Lu, Zengwei Zhu, and Kamran Behnia. Anomalous Nernst and Righi-Leduc Effects in Mn_3Sn: Berry Curvature and Entropy Flow. *Phys. Rev. Lett.*, 119:056601, Aug 2017.

[302] Mingxing Wu, Hironari Isshiki, Taishi Chen, Tomoya Higo, Satoru Nakatsuji, and YoshiChika Otani. Magneto-optical Kerr effect in a non-collinear antiferromagnet Mn_3Ge. *Applied Physics Letters*, 116(13):132408, 2020.

[303] Tomoya Higo, Huiyuan Man, Daniel B Gopman, Liang Wu, Takashi Koretsune, Olaf MJ van't Erve, Yury P Kabanov, Dylan Rees, Yufan Li, Michi-To Suzuki, et al. Large magneto-optical Kerr effect and imaging of magnetic octupole domains in an antiferromagnetic metal. *Nat. Photonics*, 12(2):73–78, 2018.

[304] H. Kurt, N. Baadji, K. Rode, M. Venkatesan, P. Stamenov, S. Sanvito, and J. M. D.

Coey. Magnetic and electronic properties of D022-Mn_3Ge (001) films. *Appl. Phys. Lett.*, 101(13):132410, 2012.

[305] Hao Yang, Yan Sun, Yang Zhang, Wu-Jun Shi, Stuart SP Parkin, and Binghai Yan. Topological Weyl semimetals in the chiral antiferromagnetic materials Mn_3Ge and Mn_3Sn. *New J. Phys.*, 19(1):015008, 2017.

[306] Taishi Chen, Takahiro Tomita, Susumu Minami, Mingxuan Fu, Takashi Koretsune, Motoharu Kitatani, Ikhlas Muhammad, Daisuke Nishio-Hamane, Rieko Ishii, Fumiyuki Ishii, et al. Anomalous transport due to Weyl fermions in the chiral antiferromagnets Mn_3X, X= Sn, Ge. *Nat. Commun.*, 12(1):572, 2021.

[307] R. S. Popović. In *Hall Effect Devices*. CRC Press, 2004.

[308] E. Ramsden. In *Hall-Effect Sensors: Theory and Application*. Elsevier, dec 2006.

[309] Yu Pan, Congcong Le, Bin He, Sarah J Watzman, Mengyu Yao, Johannes Gooth, Joseph P Heremans, Yan Sun, and Claudia Felser. Giant anomalous Nernst signal in the antiferromagnet $YbMnBi_2$. *Nat. Mater.*, 21(2):203–209, 2022.

[310] Daniel Destraz, Lakshmi Das, Stepan S Tsirkin, Yang Xu, Titus Neupert, J Chang, A Schilling, Adolfo G Grushin, Joachim Kohlbrecher, Lukas Keller, et al. Magnetism and anomalous transport in the Weyl semimetal PrAlGe: possible route to axial gauge fields. *npj Quantum Materials*, 5(1):5, 2020.

[311] M Ikhlas, S Dasgupta, F Theuss, T Higo, Shunichiro Kittaka, BJ Ramshaw, O Tchernyshyov, CW Hicks, and S Nakatsuji. Piezomagnetic switching of the anomalous Hall effect in an antiferromagnet at room temperature. *Nat. Phys.*, 18(9):1086–1093, 2022.

[312] ZH Liu, YJ Zhang, GD Liu, B Ding, EK Liu, Hasnain Mehdi Jafri, ZP Hou, WH Wang, XQ Ma, and GH Wu. Transition from anomalous Hall effect to topological Hall effect in hexagonal non-collinear magnet Mn_3Ga. *Sci. Rep.*, 7(1):515, 2017.

[313] V. Rai, S. Jana, M. Meven, R. Dutta, J. Perßon, and S. Nandi. Unconventional magnetoresistance and electronic transition in Mn_3Ge Weyl semimetal. *Phys. Rev. B*, 106:195114, Nov 2022.

[314] J. Kübler and C. Felser. Non-collinear antiferromagnets and the anomalous Hall effect. *Europhys. Lett.*, 108(6):67001, dec 2014.

[315] Xiaolei Wang, Dong Pan, Qingqi Zeng, Xue Chen, Hailong Wang, Duo Zhao, Zhiyang Xu, Qianqian Yang, Jinxiang Deng, Tianrui Zhai, et al. Robust anomalous Hall effect and temperature-driven Lifshitz transition in Weyl semimetal Mn_3Ge. *Nanoscale*, 13(4):2601–2608, 2021.

[316] J. Kübler and C. Felser. Weyl fermions in antiferromagnetic Mn_3Sn and Mn_3Ge. *Europhys. Lett.*, 120(4):47002, feb 2018.

[317] Cheng-Yi Huang, Hugo Aramberri, Hsin Lin, and Nicholas Kioussis. Noncollinear magnetic modulation of Weyl nodes in ferrimagnetic Mn_3Ga. *Phys. Rev. B*, 102:094403, Sep 2020.

[318] Tianye Yu, Rui Liu, Yiran Peng, Pengyu Zheng, Guangwei Wang, Xiaobo Ma, Zhihong Yuan, and Zhiping Yin. Correlated electronic structure of the kagome metal Mn_3Sn. *Phys. Rev. B*, 106:205103, Nov 2022.

[319] Man Li, Qi Wang, Guangwei Wang, Zhihong Yuan, Wenhua Song, Rui Lou, Zhengtai Liu, Yaobo Huang, Zhonghao Liu, Hechang Lei, et al. Dirac cone, flat band and saddle point in kagome magnet YMn_6Sn_6. *Nat. Commun.*, 12(1):3129, 2021.

[320] Mingu Kang, Shiang Fang, Linda Ye, Hoi Chun Po, Jonathan Denlinger, Chris Jozwiak, Aaron Bostwick, Eli Rotenberg, Efthimios Kaxiras, Joseph G Checkelsky, et al. Topological flat bands in frustrated kagome lattice CoSn. *Nat. Commun.*, 11(1):4004, 2020.

[321] Mingu Kang, Linda Ye, Shiang Fang, Jhih-Shih You, Abe Levitan, Minyong Han, Jorge I Facio, Chris Jozwiak, Aaron Bostwick, Eli Rotenberg, et al. Dirac fermions and flat bands in the ideal kagome metal FeSn. *Nat. Mater.*, 19(2):163–169, 2020.

[322] John P. Perdew, Kieron Burke, and Matthias Ernzerhof. Generalized Gradient Approximation Made Simple. *Phys. Rev. Lett.*, 77:3865–3868, Oct 1996.

[323] Paolo Giannozzi, Stefano Baroni, Nicola Bonini, Matteo Calandra, Roberto Car, Carlo Cavazzoni, Davide Ceresoli, Guido L Chiarotti, Matteo Cococcioni, Ismaila Dabo, et al. QUANTUM ESPRESSO: a modular and open-source software project for quantum simulations of materials. *J. Phys. Condens. Matter*, 21(39):395502, 2009.

[324] Paolo Giannozzi, Oliviero Andreussi, Thomas Brumme, Oana Bunau, M Buongiorno Nardelli, Matteo Calandra, Roberto Car, Carlo Cavazzoni, Davide Ceresoli, Matteo Cococcioni, et al. Advanced capabilities for materials modelling with Quantum ESPRESSO. *J. Phys. Condens. Matter*, 29(46):465901, 2017.

[325] Rodrigo A. Vicencio, Camilo Cantillano, Luis Morales-Inostroza, Bastián Real, Cristian Mejía-Cortés, Steffen Weimann, Alexander Szameit, and Mario I. Molina. Observation of Localized States in Lieb Photonic Lattices. *Phys. Rev. Lett.*, 114:245503, Jun 2015.